Longo

LBL

UNIVERSITY OF CALIFORNIA

Los Angeles

An Experimental Test of Time Reversal Invariance in the Reaction $n + p \rightarrow \gamma + d$

A dissertation submitted in partial satisfaction of the requirements for the degree Doctor of Philosophy in Physics

by

Bryce Leon Schrock

Committee in charge:

Professor Roy P. Haddock, Chairman

Professor B. M. K. Nefkens

Professor Donald H. Stork

Professor David T. Griggs

Professor George O. Abell

1971

FERMILAB
LIBRARY

AAD1177

The dissertation of Bryce Leon Schrock is approved, and it is acceptable in quality for publication on microfilm.

B. M. K. Nefkens

Donald H. Stork

David T. Griggs

George O. Abell

Roy P. Haddock, Committee Chairman

University of California, Los Angeles

1971

TABLE OF CONTENTS

LIST OF TABLES vii

LIST OF FIGURES viii

ACKNOWLEDGMENTS x

ABSTRACT xii

I. Theory 1

A. Introduction 1

B. General C, P and T Considerations 2

C. C- and T-symmetry in the Electromagnetic Interaction 5

D. Reciprocity Relations, Detailed Balance and T-invariance 11

E. Theoretical Model for the Effect of a T-violation in the Reaction $n+p \rightarrow \gamma+d$ ... 12

II. Experiment 20

A. General Design 20

1. Requirements 20

2. $n+p \rightarrow \gamma+d$ Detection 20

3. Discrimination Against Background Events 22

B. Apparatus 23

1. General Description 23

2. Neutron Beam 26

3. Liquid Hydrogen Target (LH_2 Target) 29

4. Wire-spark-chamber Spectrometer 33

a. General Description 33

b. Wire Spark Chambers 33

c. Analyzing Magnet 39

d. Counters 40

5. Gamma Chamber 40

6. γ-shower Anti-counters 45

7. Neutron Beam Monitors 45

8. Electronics 47

9. PDP-5 On-line Computer 49

C. Data Collection 52

III. Data Analysis 56

A. General Description 56

B. Gamma Chamber Data 58

1. Automatic Scanning System 58

2. Computer Data Reduction 59

3. Gamma Chamber Efficiency 62

C. Wire-chamber Spectrometer Data 70

1. Spark Location 70

2. Momentum Calculation 74

3. Mass Calculation 79

4. Energy Loss Correction 80

5. Spectrometer Efficiency 82

LBL

D. Least-squares Kinematic Fitting 87

E. Monte Carlo Computer Programs 95

1. General Description 95

2. Solid Angle Calculation 97

3. Kinematic Fitting Check 100

4. Background Subtraction Aid 103

F. Background Subtraction 104

G. Angular Distribution Calculation 106

H. Corrections to the Angular Distributions 112

1. Nuclear Scattering of the Deuteron 112

2. Accidentals in the LH_2 Anti-counters 115

3. Target Empty Corrections 115

4. Neutron Energy Adjustment 116

5. Additional Photon Detection Considerations .. 118

IV. Results and Conclusions 120

A. General Comments 120

B. Error Analysis 121

1. General Description 121

2. Background Subtraction Uncertainty 121

3. Solid Angle Calculation Uncertainty 122

4. Uncertainty in Deuteron Nuclear Scattering Losses 123

5. Uncertainty in the Neutron Energy Determination 123

6. Total Calculated Uncertainty 124

C. Angular Distribution Results 124

D. Conclusions 134

References 138

LBL

LIST OF TABLES

1. Scaled Singles and Coincidence Rates 50

2. Time of Flights 51

3. Rejected Events 82

4. Estimated Uncertainties (%) for Sample I 125

5. Estimated Uncertainties (%) for Sample II 126

6. $n+p \rightarrow \gamma+d$ Angular Distribution for Sample I 128

7. $n+p \rightarrow \gamma+d$ Angular Distribution for Sample II 129

8. Final $n+p \rightarrow \gamma+d$ Angular Distribution 131

9. Second Degree Legendre Coefficients 133

LIST OF FIGURES

1. Feynman Graphs for the Reaction $n+p \rightarrow \gamma+d$ 15

2. Plan View of the Experimental Arrangement 24

3. Scatter Plot of the Neutron Beam Intensity 28

4. Neutron Beam Energy Spectrum 30

5(a). Plan View of the Liquid Hydrogen Target 31

5(b). Side View of the Liquid Hydrogen Target 32

6. Photograph of Wire Chamber S_2 36

7. Photograph of Experimental Area 41

8. Gamma Chamber Photographs of Calibration and Real Events 44

9. Schematic of Neutral Beam Monitor 46

10. Simplified Schematic of Electronic Logic 48

11. Schematic of the Data Analysis Procedure 57

12. Photon Conversion Points in the γ-chamber 63

13. Calculated Efficiency of the Gamma Chamber 65

14. Distribution of the Number of γ-chamber Counters that Fired per Event 67

15. Scatter Plot of the Number of Sparks/Shower vs. the Shower Energy 68

16. Analyzing Magnet Coordinate System 76

17. Charged Particle Mass Calculated From the Particle's Momentum and Time of Flight 81

18. Energy Loss Correction for Charged Particles 83

19. Coordinate System Used by the Kinematic Fitting Program 88

20. χ^2-plots From the Kinematic Fitting Program 94

21. Missing Mass(m_x) Plot From the 1C Fit (m_d is the Deuteron Mass) 96

22. Distributions of Real and Monte Carlo $n+p \rightarrow \gamma+d$ Events on Wire Chambers S_2 and S_4 101

23. Comparison of χ^2-plots for Real and Monte Carlo $n+p \rightarrow \gamma+d$ Events 102

24. Comparison of χ^2-plots for Real Data and for Monte Carlo $n+p \rightarrow \pi^0+d$ Data 105

25(a). χ^2-plots for $\theta^*_{dn} \simeq 30^o$ 107

25(b). χ^2-plots for $\theta^*_{dn} \simeq 60^o$ 108

25(c). χ^2-plots for $\theta^*_{dn} \simeq 90^o$ 109

25(d). χ^2-plots for $\theta^*_{dn} \simeq 120^o$ 110

25(e). χ^2-plots for $\theta^*_{dn} \simeq 150^o$ 111

26. Percentage of Deuterons Lost Due to Nuclear Scattering 114

27. $n+p \rightarrow \gamma+d$ Angular Distributions for Samples I and II 130

28. Comparison of Angular Distributions for $n+p \rightarrow \gamma+d$ and $\gamma+d \rightarrow n+p$ 132

29. Plot of A_1/A_o and A_2/A_o as a Function of T_n and k_γ 136

LBL

ACKNOWLEDGMENTS

I would like to gratefully acknowledge the assistance of the many people who contributed to this experiment.

In particular, I would like to thank my advisor, Dr. Roy P. Haddock, for his support and encouragement throughout the entire experiment.

The many contributions of Steve Wilson both in running the experiment and in analyzing the data are very much appreciated.

I am indebted to Dr. Michael Longo for suggesting the experiment and for his help in implementing it.

Those involved in the design and execution of the experiment included: Michael J. Longo, Stephen S. Wilson and Kenneth K. Young from the U. of Michigan; David Cheng, Victor Perez-Mendez and John Sperinde from L.R.L.; and Jean-Francois Detoeuf, Roy P. Haddock and Jerome A. Helland from U.C.L.A.

The outstanding assistance of Leonard Proehl in the electronics instrumentation was greatly appreciated. I would also like to thank the staff of the 184-inch cyclotron, especially James Vale, Lloyd Hauser and Donald Rothfuss, for their help and cooperation.

The elegant computer programming of Les Wilson for the CDC 6600 analysis routines is most gratefully acknowledged. The PDP-5 programming for the VIDICON scanning system was

LBL

very skillfully handled by Jim Gillespie, and the PDP-5 programs for the on-line computer were largely due to Peter Berardo.

The smooth operation of the VIDICON measuring device was ensured by the capable efforts of Anne Carter and Charles Smith.

Most of all, for her patience, support and continuous encouragement, I thank my wife, Jane.

LBL

ABSTRACT OF THE DISSERTATION

An Experimental Test of Time Reversal Invariance in the Reaction $n + p \rightarrow \gamma + d$

by

Bryce Leon Schrock
Doctor of Philosophy in Physics
University of California, Los Angeles, 1971
Professor Roy P. Haddock, Chairman

A measurement of the angular distribution for the reaction $n + p \rightarrow \gamma + d$ has been made at the Lawrence Radiation Laboratory 184-inch cyclotron for neutron kinetic energies in the range 300 to 720 MeV. A total of 30,000 $n + p \rightarrow \gamma + d$ events were collected in 20 energy-angle bins. A comparison with the angular distribution for the inverse process indicates that the data are consistent with time-reversal invariance in this reaction. If the results are interpreted in the framework of a model by S. Barshay, the measured T-violating phase angle is $\phi = (4 \pm 10)^{\circ}$ where $\phi = 90^{\circ}$ for a maximal T-violation.

I. THEORY

A. INTRODUCTION

The discovery[1] of the decay mode

$$K_2^o \rightarrow \pi^+ + \pi^- , \qquad (1)$$

in apparent violation of CP-invariance, has caused an extensive re-examination, ~~for all the interactions,~~ of the discrete space-time symmetries consisting of charge conjugation(C), parity(P) and time reversal(T). Thus far the observed CP-violating effects are all of the order 2×10^{-3} in amplitude and are limited to K^o decay[2]. Much theoretical and experimental effort has been devoted to determining in which interaction, and with what strength, the CP-violation occurs.

If CPT is a good symmetry, for which there is strong evidence[2], then the observed CP-violation implies a T-violation. Bernstein, Feinberg and Lee[3] pointed out, in 1965, that there was a complete lack of evidence that the electromagnetic interaction of hadrons is invariant under C and T. Furthermore, Bernstein et al[3], and also Barshay[4], indicated that the rather small CP-violating effect demonstrated by the weak decay $K_2^o \rightarrow \pi^+ + \pi^-$ could be rather naturally explained if there were a large violation of C- and T-invariance in the electromagnetic interaction

LBL

of strongly-interacting particles(hadrons). Thus it appeared worthwhile to test, experimentally, T-invariance in the electromagnetic interaction of hadrons.

The reciprocity relations between a reaction and its inverse constitute one of the most direct tests of T-invariance. One aspect of these relations is that, at the same center of mass energy, the angular distributions for the direct reaction and the inverse reaction are identical. If a difference were to be observed in the angular distributions, this difference would be direct evidence for a T-violation in the reaction.

Barshay[5] suggested that a comparison of the angular distributions for the reactions $n+p \rightarrow \gamma+d$ and $\gamma+d \rightarrow n+p$ would be a sensitive test of T-invariance in the electromagnetic interaction of hadrons. Using a simple model due to Austern[6], he calculated that the angular distributions might differ by as much as 40% if a maximal T-violation were present. Thus, since the angular distribution for $\gamma+d \rightarrow n+p$ has been repeatedly measured, we designed an experiment to measure the corresponding distribution for the reaction $n+p \rightarrow \gamma+d$.

B. GENERAL C, P AND T CONSIDERATIONS

Many excellent review articles[2,7,8] have summarized, for all the interactions, the progress and current status of the attempts to understand the CP-violation. This

section will not be concerned with the many experimental tests of the symmetry principles in the weak interactions but rather will be restricted to those tests and results relevant to the strong and electromagnetic interactions.

The most sensitive tests of the CPT-symmetry result from the fact that this symmetry implies[9] mass and lifetime equalities between any particle and its antiparticle. The most accurate such equality exists between K^o and $\bar{K}^o$:

$$\langle K^o | H_{st} + H_\gamma + H_{wk} | K^o \rangle = \langle \bar{K}^o | H_{st} + H_\gamma + H_{wk} | \bar{K}^o \rangle, \quad (2)$$

where H_{st}, H_γ and H_{wk} are, respectively, the strong, electromagnetic and weak Hamiltonians. Although the mass difference between K^o and $\bar{K}^o$ cannot be measured directly, it should not be greater than the measurable difference Δm ($= m_{K_2^o} - m_{K_1^o}$) where K_2^o and K_1^o are the long- and short-lived kaons, respectively. From the experimental mass difference Δm[10], it can be concluded that equation (2) holds to $|\Delta m/m_K| \simeq 10^{-14}$. Therefore the upper limit on CPT-violating strong interactions is indeed very small. Since the electromagnetic contributions (H_γ) to the kaon mass are expected to be of the order αm_K, where α is the fine structure constant, the measurement of Δm also permits an upper limit on the CPT-violating electromagnetic interaction of the order of 10^{-11} to 10^{-12}. Thus CPT-invariance in strong and electromagnetic interactions is not violated

sufficiently to account for the observed CP-violating effects.

Although parity(P) is violated maximally in the weak interactions[11], it is generally considered to be a valid symmetry in the strong and electromagnetic interactions. Many experiments[12,13], searching for P-violating effects in nuclear reactions, have established that the magnitudes of P-nonconserving amplitudes are smaller than those of the corresponding P-conserving amplitudes by a factor of $\approx 10^{-5}$, which is the order of magnitude of the dimensionless weak coupling constant.

Consequently, since CPT and P are to be regarded as good symmetries in the strong and electromagnetic interactions, both interactions should be invariant under CT to the same level of accuracy that they are invariant under CPT and P. Thus if either interaction is responsible for the observed CP-violation, that interaction must violate both the C- and T-symmetries. However, existing data for strong interactions exclude any C- or T-violation at a level greater than ≈1%. In particular, comparisons[14,15] of the energy distributions of positive and negative pions and kaons in the reactions

$$\bar{p} + p \rightarrow n\pi^{+}(K^{+}) + n\pi^{-}(K^{-}) + \pi^{0}\text{'s} \qquad (3)$$

indicate that C-violating amplitudes for the strong interaction are smaller than ≈1%. Also, several experiments

have compared[16,17] the rates for direct and inverse reactions such as

$$^{24}Mg + d \rightleftarrows {}^{25}Mg + p \tag{4a}$$

and

$$^{24}Mg + \alpha \rightleftarrows {}^{27}Al + p \tag{4b}$$

and have found the rates to be equal to within a few parts per thousand. The maximum T-violating amplitudes for strong interactions should therefore be less than $\simeq 1/2\%$.

In conclusion, the strong interaction appears to be invariant both under the product CPT and also under C, P and T individually. There is also good evidence that the electromagnetic interaction is invariant under CPT and P. The situation for the electromagnetic interaction with respect to the C- and T-symmetries will be discussed in the next section.

C. C- AND T-SYMMETRY IN THE ELECTROMAGNETIC INTERACTION

Experimental results on the anomalous magnetic moment of the muon[18] and on the Lamb shift[19] indicate that the electromagnetic interaction of leptons is adequately described by the form $I_\mu \cdot A_\mu$ where

$$I_\mu = ie\Psi^+\gamma_4\gamma_\mu\Psi \tag{5}$$

is the lepton current and A_μ is the electromagnetic field. The lepton field operators are Ψ^+ and Ψ and the $\gamma_\mu, \mu=1\rightarrow4$,

are the usual Dirac matrices. The form $I_\mu \cdot A_\mu$, with I_μ given by equation (5), is explicitly invariant under C, P and T, and consequently no C- or T-violation is expected in the electromagnetic interaction of leptons.

However, as pointed out by Bernstein, Feinberg and Lee[3], and also by Barshay[4], no such statement can be made concerning the electromagnetic interaction of hadrons. In particular, Bernstein et al[3] pointed out, in 1965, that there was no experimental evidence indicating that C and T were valid symmetries for the electromagnetic interaction of hadrons. Consequently, if C- and T-invariance are not assumed, the electromagnetic current operator I_μ must be written in a more general form than equation (5). In particular, in order to emphasize the transformation properties under C, I_μ can be expressed as

$$I_\mu = J_\mu + K_\mu \tag{6}$$

where J_μ and K_μ are both vector currents and are assumed to have identical transformation properties under CPT. However, under C, J_μ is assumed to have the normal(odd) transformation properties:

$$CJ_\mu C^{-1} = -J_\mu \tag{7}$$

whereas K_μ is even under C:

$$CK_\mu C^{-1} = K_\mu \ . \tag{8}$$

Thus the condition of C- and T-invariance is that $K_\mu = 0$.

If it is assumed that $K_\mu \neq 0$ and that some of its matrix elements are comparable in magnitude to those of J_μ (large C- and T-violation), then C- and T-violating effects can be induced in all strong reactions, to the order of $\alpha(\simeq 1/137)$, by virtual electromagnetic processes. Similarly, the rather small magnitude ($\simeq 2 \times 10^{-3}$) of the amplitude for the CP-violating decay $K_2^o \to \pi^+\pi^-$ could be understood as resulting from the supplementary virtual emission and absorption of a photon with respect to the CP-conserving decay $K_1^o \to \pi^+\pi^-$. Thus one might naturally expect the decay $K_2^o \to \pi^+\pi^-$ to occur with an amplitude $\simeq(\alpha/\pi)$ times that of $K_1^o \to \pi^+\pi^-$.

Therefore it appears important to test experimentally the hypothesis that there exist large violations of C- and T-invariance in the electromagnetic interaction of hadrons. Five such tests which have been performed are described below.

(1) <u>Inelastic scattering of electrons from a polarized proton target</u>

Christ and Lee[20] proposed a test of T-invariance that involved the inelastic scattering of electrons from a polarized proton target in which only the scattered electron is detected. For the reaction

$$e + p \to e + \Gamma \,, \tag{9}$$

let $\sigma\uparrow(\sigma\downarrow)$ represent the cross section, summed over all outgoing hadronic states Γ, where the target spin is along (opposite to) the normal $\hat{n}$ to the electron scattering plane

$$\hat{n} = (\vec{p}_{in} \times \vec{p}_{out}) \; / \; |\vec{p}_{in} \times \vec{p}_{out}| \tag{10}$$

where $\vec{p}_{in}$ and $\vec{p}_{out}$ are the momentum vectors of the incident and scattered electron, respectively. Then the asymmetry

$$A = (\sigma\uparrow - \sigma\downarrow)/(\sigma\uparrow + \sigma\downarrow) \tag{11}$$

must vanish, in the single-photon-exchange approximation, unless T-invariance is violated. Two experiments[21,22] report values of A consistent with <u>no</u> T-invariance violation for electron energies corresponding to excitation of the 1236-, 1512- and 1688-MeV nucleon resonances.

(2) <u>$\eta^o \to \pi^+\pi^-\pi^o$ and $\eta^o \to \pi^+\pi^-\gamma$</u>

Asymmetries of the order of several per cent may be expected in the energy distributions of π^+ and π^- for both decays if C is violated in the electromagnetic interaction. The asymmetry is defined as

$$A = (N^+ - N^-)/(N^+ + N^-) \tag{12}$$

where N^+ is the number of decays with $T^{\pi^+} > T^{\pi^-}$ and N^- is the number with $T^{\pi^-} > T^{\pi^+}$ (T^π is the kinetic energy of the π). For the decay $\eta^o \to \pi^+\pi^-\pi^o$, Gormley et al[23] report $A = (1.5 \pm 0.5)\%$ whereas Cnops et al[24] report that

$A = (0.3 \pm 1.0)\%$. For the decay $\eta^o \to \pi^+\pi^-\gamma$, Bowen et al[25] obtain a value $A = (1.5 \pm 2.5)\%$ and Gormley et al[26] obtain $A = (2.4 \pm 1.4)\%$. These experimental results are inconclusive[27] with regard to the possibility of a C-violation in the electromagnetic interaction.

(3) $\underline{\eta^o \to e^+ + e^- + \pi^o}$

If C is violated, this decay is of the order α^2 ($\alpha \approx 1/137$) whereas if C is conserved the decay is of the order α^4, a factor of $\approx 10^4$ smaller. The decay has not been observed and the present upper limit[28] for the branching ratio is 2.3×10^{-3} (90% confidence level). The implication of this upper limit is unclear, however, since the decay is inhibited by angular momentum barriers.

(4) Neutron electric dipole moment

Parity violation in the weak interaction combined with a C-violation in the electromagnetic interaction would result in a nonzero electric dipole moment μ for the neutron. The predicted magnitude of such a dipole moment is very model dependent but on the basis of a dimensional argument might be expected to be

$$\mu/e \approx 10^{-19} \text{ cm.} \tag{13}$$

Baird et al[29] report a value $\mu/e = (1.8 \pm 1.1) \times 10^{-23}$cm which is three orders of magnitude smaller than expected

from a dimensional argument. However, due to the model dependence of the prediction, no firm conclusion can be drawn[30].

(5) $\pi^- p \rightleftarrows n\gamma$ differential cross sections

Christ and Lee[31] suggested that a comparison of the differential cross sections for $\pi^- p \to n\gamma$ and $n\gamma \to \pi^- p$ would be a sensitive test of T-invariance. The differential cross section for $\pi^- p \to n\gamma$ has been measured[32] at a c.m. energy near the $P^o_{33}(1236)$ resonance and compared to the corresponding distribution for $n\gamma \to \pi^- p$, deduced from $\gamma d \to pp\pi^-$ measurements. This comparison seems to exclude a strong violation in the isovector or isotensor amplitudes but a maximum violation in the isoscalar amplitude is possible.

In conclusion, no clear-cut evidence for C- or T-violation in the electromagnetic interaction has been found. There is some evidence against an electromagnetic C- or T-violation sufficiently large to account for the observed CP-violation in K decay but models can be constructed which circumvent this evidence.

D. RECIPROCITY RELATIONS, DETAILED BALANCE AND T-INVARIANCE

It is a well known fact[33] that T-invariance implies the reciprocity relations. These relations state that the S-matrix elements for a reaction $\alpha \rightarrow \beta$ are equal to those for the time-reversed reaction $-\beta \rightarrow -\alpha$:

$$S_{\alpha\beta} = S_{-\beta-\alpha} \tag{14}$$

where α and β represent the incoming and outgoing channels, respectively, for the forward reaction and $-\alpha$ and $-\beta$ are the channels α and β with all linear and angular momenta (and spins) reversed.

The more useful, but less general, principle of detailed balance follows from the reciprocity relations. This principle states that, at the same c.m. energy, the c.m. differential cross sections for the two-body reaction $a+b \rightleftarrows c+d$ are related by:

$$\frac{d\sigma}{d\Omega}(\rightarrow) = \frac{(2S_c+1)(2S_d+1)}{(2S_a+1)(2S_b+1)} \left(\frac{p_c}{p_a}\right)^2 \frac{d\sigma}{d\Omega}(\leftarrow) \tag{15}$$

where $d\sigma/d\Omega(\rightarrow)$ and $d\sigma/d\Omega(\leftarrow)$ are the differential cross sections for $a+b \rightarrow c+d$ and $c+d \rightarrow a+b$, respectively. The S_i and p_i in equation (15) are the spin and momentum, respectively, of the ith particle. Equation (15) results only after summing over all initial and final spin states and consequently any experiment which tests the principle

of detailed balance must avoid spin polarizations in both the initial and final states. In practice this means that the incident beam and target particles must be unpolarized and that final state spins must not be detected.

It follows from equation (15) that, at the same c.m. energy, the angular distributions for the forward reaction $a+b \rightarrow c+d$ and the inverse reaction $c+d \rightarrow a+b$ must be identical. Thus any statistically significant discrepancy between these angular distributions would be a direct indication of a failure of T-invariance in the reaction.

E. THEORETICAL MODEL FOR THE EFFECT OF A T-VIOLATION IN THE REACTION $n + p \rightarrow \gamma + d$

Although it is true that a breakdown of the reciprocity relations between a reaction and its inverse would imply a T-violation, the converse is not true. That is, a large T-violation in a particular reaction would <u>not necessarily</u> imply a correspondingly large discrepancy between the angular distributions for the reaction and its inverse. In particular, Christ and Lee[31] have pointed out that in photon-nucleon reactions without meson production(or absorption) the nucleons are, or almost are, on the mass shell. Any T-noninvariant terms in the matrix element for the reaction then vanish due to current conservation. Thus Christ and Lee[31] conclude that reciprocity relations for reactions such as $n+p \rightarrow \gamma+d$ are relatively insensitive

to a T-violation.

However, the total cross section[34,35] for the reaction $\gamma+d \rightarrow n+p$ has a large bump near an incident photon energy of ≈290 MeV. This bump is generally attributed to the influence of the Δ(1236) on the process and consequently there do exist intermediate states for the reaction $n+p \rightleftarrows \gamma+d$ which are off the mass shell. These considerations led Barshay[5] to suggest that a comparison of the angular distributions for the reactions:

$$n + p \rightarrow \gamma + d \tag{16a}$$

and

$$\gamma + d \rightarrow n + p \tag{16b}$$

would constitute a sensitive test of T-invariance in the electromagnetic interaction of hadrons.

Barshay, using a model due to Austern[6], calculated[5] the matrix element M for deuteron photodisintegration via an intermediate state in which one of the nucleons from the deuteron has been excited to the J=I=3/2 isobar Δ(1236) by absorption of a magnetic dipole photon. Calculation of the matrix element in the center of mass system involved the evaluation of the Feynman graph depicted in Fig. 1a and resulted in the following expression for M:

$$M = G\ \{(1/3)\sqrt{(2/3)}\}\ \sqrt{\{m^2/(m_d k E^2)\}}\ \frac{p^2 k\sqrt{2}\omega}{(k+m-m^*+i\gamma^*/2)(m+\omega-E)}$$

$$\times \int \frac{d\vec{Q}}{(2\pi)^3(mB+Q^2)}\ \{3\hat{p}\cdot\hat{t}\hat{p}\cdot\hat{k}\times\hat{\varepsilon} - \hat{t}\cdot\hat{k}\times\hat{\varepsilon}\}\ \chi_2^T\sigma_y\chi_1 \tag{17}$$

where m, m_d, m^* and m_π denote the masses of the nucleon, deuteron, isobar and pion, respectively. In equation (17), k is the photon momentum, p the nucleon momentum, $\gamma^* \approx 120$ MeV the isobar width, $\vec{Q}$ the deuteron internal momentum, B the deuteron binding energy, t the deuteron polarization pseudovector, ε the photon polarization vector, σ_y the Pauli spin operator, and χ_i the nucleon spinors (χ_i^T are the transposed spinors). The total energies of the nucleon and pion are $E = \sqrt{p^2+m^2}$ and $\omega = \sqrt{p^2+m_\pi^2}$, respectively. The last two factors in equation (17) constitute a projection operator for the $^1D_2$ state of the final two-nucleon system which is the dominant transition induced by absorption of a magnetic dipole photon (see Fig. 1a). The cutoff Q_{max} for the integral over the deuteron internal momentum in equation (17) is determined by equating the total cross section computed from the matrix element M to $\approx 27\mu b$ which is the approximate contribution of the resonant bump to the total $\gamma + d \rightarrow n + p$ cross section.

The quantity G appearing in equation (17) is a product

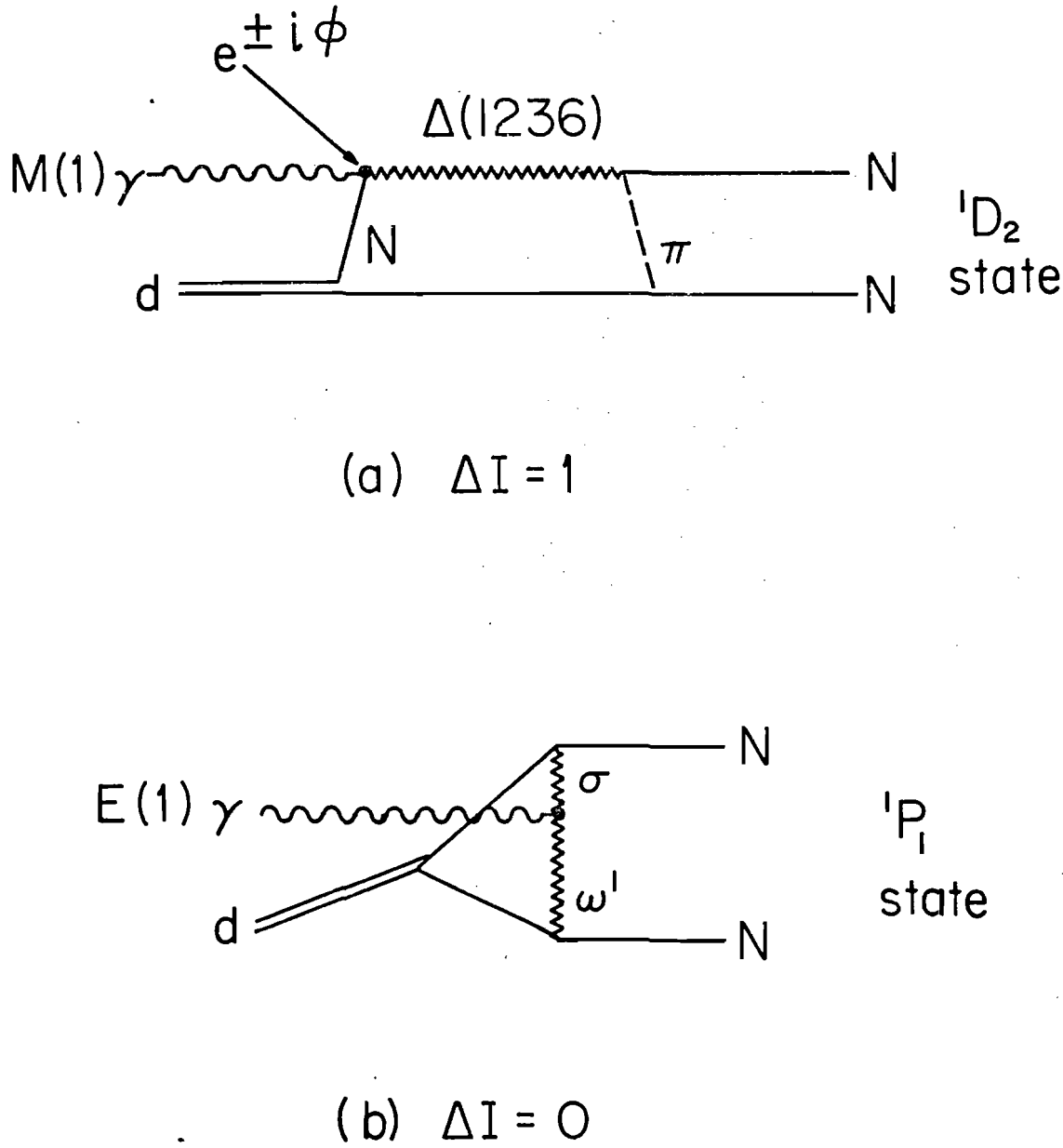

Figure 1. Feynman Graphs for the Reaction n+p → γ+d

of four known coupling parameters:

$$G = (a/\sqrt{2})\ g\ G_{\pi}^{*}\ G_{\gamma}^{*} \tag{18}$$

where g, G_{π}^{*} and G_{γ}^{*} are the pion-nucleon, the isobar-nucleon-pion and the photon-nucleon-isobar coupling constants, respectively. The quantity $a/\sqrt{2}$ represents the deuteron-two nucleon "coupling constant" and is estimated from the asymptotic form of the deuteron S-state wave function. The hypothetical failure of T-invariance is then introduced by giving a phase $\phi \neq 0,\pi$ to the vertex for $\gamma N \rightleftarrows \Delta$ represented by G_{γ}^{*}. The matrix element M in equation (17) is then proportional to $e^{i\phi}$ and the matrix element for the inverse reaction M_r is given by equation (17) with $e^{i\phi}$ changed to $e^{-i\phi}$. The essential effect that can cause a significant failure of reciprocity occurs at an energy such that the real part of the resonance denominator in equation (17) vanishes. For a maximal T-violation ($\phi=\pi/2$) both matrix elements, M and M_r, are then real and

$$M \simeq -M_r\ . \tag{19}$$

The isobar amplitude changes sign in going from the reaction to its inverse and, if there are other relatively real amplitudes present, reciprocity between the differential cross sections can be grossly violated.

Barshay includes in the matrix element amplitudes for transitions felt to be present at lower energies: $M(1) \rightarrow {}^1S_0$

denoted by a_o and $E(1)\to{}^3P_o$ denoted by b_o. The total matrix element is then given by

$$M_t = M + a_o\ \hat{t}\cdot\vec{k}\times\hat{\varepsilon}\chi_2^T\ \sigma_y\chi_1 + ib_o\ \hat{t}\cdot\hat{\varepsilon}\chi_2^T\ \vec{\sigma}\cdot\vec{p}\ \sigma_y\chi_1\ . \quad (20)$$

Of the total cross section of ≈75 μb at k = 290 MeV, it is estimated that $M(1)\to{}^1D_2$ contributes ≈27 μb, $E(1)\to{}^3P_o$ contributes ≈45 μb and $M(1)\to{}^1S_o$ contributes only ≈3 μb. Only the singlet states, ${}^1D_2$ and ${}^1S_o$, interfere in the differential cross sections and therefore the small amplitude a_o is essential to the failure of reciprocity.

Using reasonable approximations, Barshay calculated, for the total matrix element M_t, the following c.m. differential cross sections (in μb) for reactions (16a) and (16b):

$$\frac{4p}{k}\frac{d\sigma}{d\Omega}(16a) = 1.66\ \{10.66 + [1 \pm .94\cos(\delta_r-\phi)][3\sin^2\theta-2]\} \quad (21a)$$

and

$$\frac{6k}{p}\frac{d\sigma}{d\Omega}(16b) = 1.66\ \{10.66 + [1 \pm .94\cos(\delta_r+\phi)][3\sin^2\theta-2]\} \quad (21b)$$

where θ is the c.m. scattering angle. The phase of the resonance denominator δ_r is not taken as π/2 but rather is estimated as $\delta_r \approx \tan^{-1}3$ due to the nonzero deuteron

internal momentum. The differential cross sections as given by equations (21a) and (21b) are symmetric about $\theta = 90^{o}$ whereas experimental measurements indicate a fore-aft asymmetry. This asymmetry could be due to the interference of small amplitudes for $E(2) \rightarrow {}^{3}D$ transitions (not included in the model) with the $E(1) \rightarrow {}^{3}P$ amplitudes.

In summary, the main features of Barshay's model, reflected in equations (21a) and (21b) are: (i) the total cross sections for reactions (16a) and (16b) are equal, and (ii) the effect of a T-violation is expected to show up only in the ratio A_2/A_o where the differential cross sections are expressed in the form $d\sigma/d\Omega = A_o + A_2P_2(x)$ where P_2 is the second-order Legendre polynomial and $x = \cos\theta^*_{dn}$ where θ^*_{dn} is the c.m. angle between the deuteron and neutron. An estimate of the effect in the c.m. energy region of the $\Delta(1236)$ may be expressed as

$$\sin \phi \simeq 3 \; [A_2/A_o(16b) - A_2/A_o(16a)] \qquad (22)$$

where ϕ is the T-violating phase angle. Thus for a maximal T-violation ($\phi \simeq 90^{o}$), large differences ($\simeq 0.3$) might be expected between the ratios A_2/A_o for these reactions. Consequently we designed an experiment to measure the angular distribution for reaction (16a) with an accuracy such that the value of ϕ, appearing in equation (22) could be determined to within $\pm 10^{o}$.

It should be pointed out that the hypothetical

T-violation in Barshay's model occurs in the isovector component ($\Delta I=1$) of the electromagnetic interaction. A C-violating isoscalar component ($\Delta I=0$) could also be present[36] in transitions such as $E(1) \rightarrow {}^1P_1$ which could interfere with the isobar amplitude $M(1) \rightarrow {}^1D_2$ to produce a difference in the differential cross sections. However, the relevant Feynman graph (Fig. 1b) has not been evaluated and no estimate of the possible effect is available.

II. EXPERIMENT

A. GENERAL DESIGN

1. Requirements

The apparatus for the experiment was designed to measure the angular distribution for the reaction $n+p \rightarrow \gamma+d$ at five angles for neutron energies in the range 300 to 720 MeV. The desired precision for each measured point was three to five per cent. To achieve this precision the apparatus not only had to be highly efficient for detecting the reaction $n + p \rightarrow \gamma + d$ but also had to be highly discriminatory against background events from other reactions.

2. $n + p \rightarrow \gamma + d$ Detection

Basically the experimental configuration consisted of a neutron beam incident on a liquid hydrogen target, an optical lead plate shower chamber for detecting photons (γ's) and a magnetic spectrometer with wire spark chambers and counters for detecting deuterons(d's). Detection efficiencies for charged particles such as deuterons are typically high (>99%). However, detection of photons in the energy range of this experiment (100 to 500 MeV) is not as straightforward, particularly at the lower energies. Thus the results of a Monte Carlo study of shower

production[37] were utilized to aid in the design of the γ-shower chamber. The efficiency of the chamber will be discussed in detail in the chapter on data analysis.

Since the total cross section for the reaction $n + p \rightarrow \gamma + d$ is small (<20 μbarns for a neutron energy ≈ 590 MeV) it was necessary to have either a very intense neutron beam, a thick hydrogen target, or a large solid angle for detecting the reaction products. An intense neutron beam (≈ 4×10^6 neutrons/second at the hydrogen target over the entire energy range) was obtained by placing a beryllium target in the internal proton beam of the Berkeley 184-inch cyclotron. Although a thick hydrogen target would also have increased the yield of $n + p \rightarrow \gamma + d$ events, a thin target was used instead in order to decrease the Coulomb scattering and the energy loss of the final state deuteron as well as to improve the measurement of the photon scattering angle. Similarly, increasing the $n + p \rightarrow \gamma + d$ yield by arranging the apparatus so that it subtended a large solid angle was not practical due to the fact that part of the apparatus had to be placed at large distances from the hydrogen target in order to precisely measure the scattering angles of the deuteron and photon. A good measurement of these properties was essential in order to discriminate against reactions which simulated $n + p \rightarrow \gamma + d$.

3. Discrimination Against Background Events

Many reactions are possible for neutrons with kinetic energies $T_n < 720$ MeV impingent on a liquid hydrogen target. A list of these reactions follows with estimates of their approximate total cross sections at $T_n = 590$ MeV in parentheses.

$$
\begin{aligned}
n + p &\rightarrow n + p && (25.0\ \text{mb.}) \\
&\rightarrow n + n + \pi^+ && (\ 2.0\ \text{mb.}) \\
&\rightarrow p + p + \pi^- && (\ 2.0\ \text{mb.}) \\
&\rightarrow n + p + \pi^0 && (\ 3.4\ \text{mb.}) \\
&\rightarrow n + p + \gamma && (40.0\ \mu\text{b.}) \\
&\rightarrow d + \pi^0 \rightarrow d + \gamma + \gamma && (\ 1.5\ \text{mb.}) \\
&\rightarrow d + \gamma && (20.0\ \mu\text{b.})
\end{aligned}
$$

The last four reactions above have charged particles and photons in the final state, and of these reactions, those with a charged particle other than a deuteron were rejected by measuring the mass of that particle. The mass was determined by including in the spectrometer design a system for measuring the time of flight of the charged particle over a known distance, thereby determining its velocity. The velocity measurement, combined with the momentum measurement from the spectrometer, was sufficient to calculate the particle's mass.

The only other background reaction, $n + p \rightarrow \gamma + \gamma + d$,

provided the greatest difficulty. Not only is the cross section approximately 70 times larger than that for $n + p \rightarrow \gamma + d$, but also the kinematics of the two reactions are very similar. A Monte Carlo simulation of the experiment indicated that this background could be adequately subtracted if matter in the path of the deuteron was minimized thus reducing the multiple scattering and energy loss of the deuteron and thereby increasing the resolution of the apparatus. The hydrogen target, wire chambers and counters were designed and constructed accordingly.

B. APPARATUS

1. General Description

A floor plan of the experiment appears in Fig. 2. A neutral beam was taken off at an approximately zero degree production angle from a beryllium target positioned in the internal proton beam of the 184-inch cyclotron at Berkeley. The magnetic field of the cyclotron prevented charged particles produced in the beryllium from entering a steel collimator which served as the defining aperture for the beam. Photons in the beam were converted to electrons by two lead plates (γ-converters) placed upstream of the collimator. These electrons, along with charged particles produced in the collimator, were then removed from the

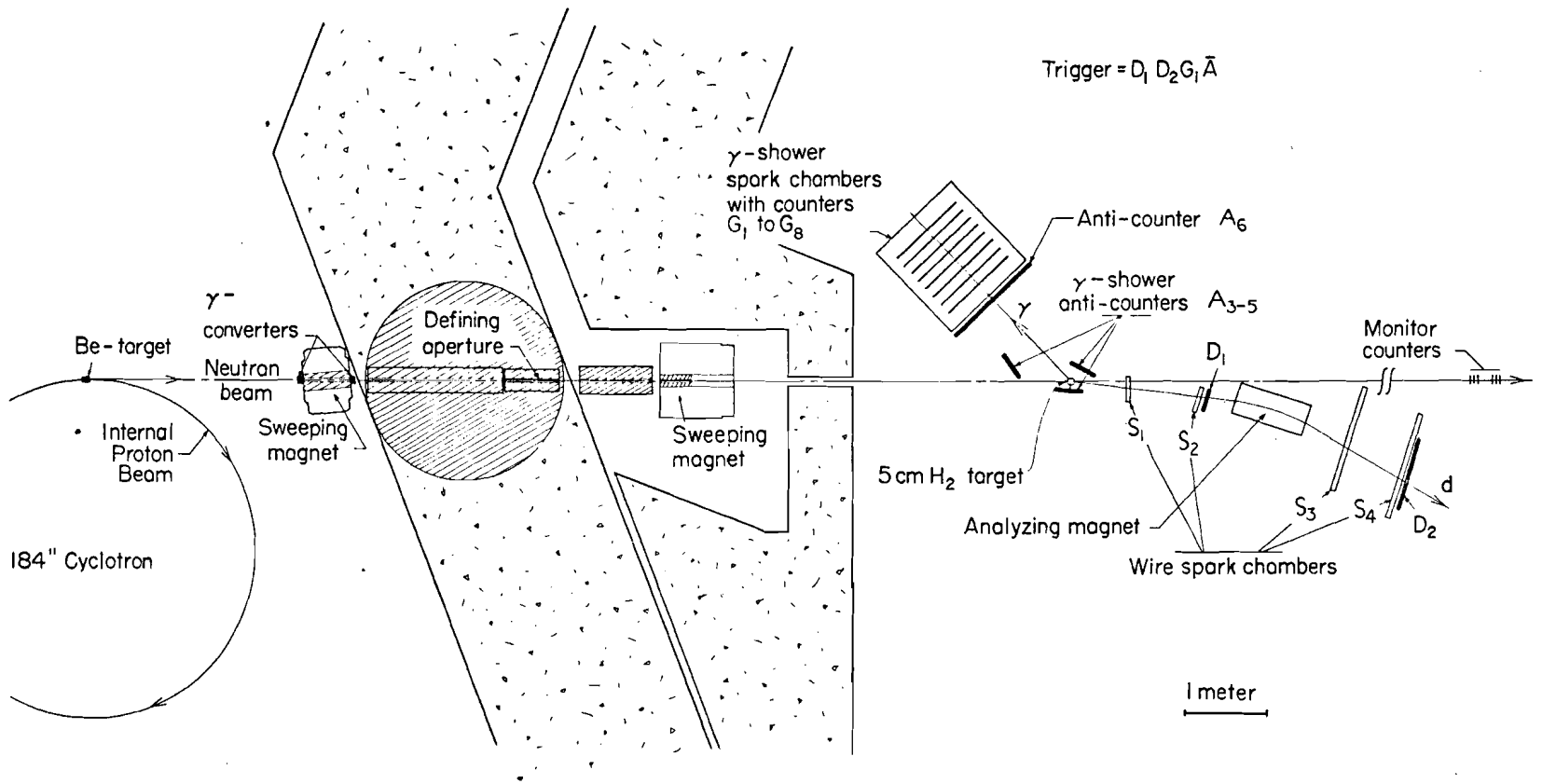

Figure 2. Plan View of the Experimental Arrangement

beam by a sweeping magnet. The neutron beam thus produced passed through a liquid hydrogen (LH_2) target, through a large aperture in a shielding wall (not shown in Fig. 2), and finally through a set of beam monitor counters.

Charged particles, produced primarily by neutron interactions in the LH_2, entered a spectrometer system consisting of two counters, D_1 and D_2, an analyzing magnet, and four wire spark chambers, two before and two after the analyzing magnet. The spectrometer system effectively measured the momentum and scattering angle of the charged particle.

Neutral particles, primarily photons of energies 100 to 500 MeV, were detected in a large lead-plate optical spark chamber with imbedded counters (G_1 to G_8). A counter in anticoincidence was placed between this γ-shower chamber and the LH_2 target in order to veto charged particles which entered the chamber. The γ-chamber and the deuteron spectrometer were both movable systems and were repositioned each time the angular distribution was to be measured at a new scattering angle.

In addition to the anti-counter in front of the γ-shower chamber, three lead-scintillator "sandwich" counters in anticoincidence partially surrounded the LH_2 target. Background events in which one of the gammas from the reaction $n + p \rightarrow \pi^o + d \rightarrow \gamma + \gamma + d$ entered the γ-shower chamber were vetoed if the second gamma was de-

tected by one of these counters.

Thus an event occurred when the electronics received, in proper coincidence, a signal from D_1, D_2, any one or more of the G_i (i=1,8), and no signal from any of the anti-counters. The spark chambers were then pulsed with high voltage. Coordinate information from the wire chambers and associated counter and scaler information for the event were recorded by a PDP-5 on-line computer, and a double-frame 35 mm photograph was taken of 90° stereo views of the photon conversion in the γ-shower chamber.

2. Neutron Beam

The neutron source was a beryllium target 3.0 inches long and 0.5 inches square in cross section positioned at a radius of 82.3 inches in the internal proton beam of the Berkeley 184-inch cyclotron. The neutron beam was taken off at (0.0±0.2) degrees with respect to the internal proton beam in order to ensure that the neutrons were not polarized. Two lead plates, each one inch thick, were placed in the beam to convert photons to charged particles. The beam was then collimated by a series of stepped collimators constructed of steel and totaling 14 feet in length with a defining aperture 2.0 inches in diameter. Charged particles produced in the beryllium target were swept away from the collimator by the magnetic field of the cyclotron. Another sweeping magnet downstream of the

collimator removed charged particles produced by neutrons interacting in the collimator as well as those from converted photons.

At the hydrogen target the beam was 2.25 inches in diameter and rather sharply defined for a neutral beam. A scatter plot of the beam intensity in a plane perpendicular to the beam and passing through the center of the LH_2 target appears in Fig. 3. The plot was obtained by tracing the deuteron trajectory from chambers S_1 and S_2 back to the midplane of the target and was corrected for the solid angle subtended by the apparatus.

If it is assumed that no T-violation occurs in the reaction $n + p \rightleftarrows \gamma + d$, then the energy spectrum of the neutron beam for this experiment can be calculated, for each configuration of the apparatus, from the yield of $n + p \rightarrow \gamma + d$ events, $Y_i(T_n)$, collected with that (i^{th}) configuration. Thus,

$$F_i(T_n) = Y_i(T_n) \;/\; \left((d\sigma/d\Omega(T_n))_i \Delta\Omega_i(T_n) \right)$$

where T_n is the neutron kinetic energy calculated for each event and the subscript i indicates the ith configuration of the apparatus at a nominal c.m. scattering angle θ_i. $Y_i(T_n)$ is the yield of $n + p \rightarrow \gamma + d$ events; $F_i(T_n)$ is the unknown neutron energy spectrum; $(d\sigma/d\Omega(T_n))_i$ is the average laboratory differential cross section for $n + p \rightarrow \gamma + d$ calculated by detailed balance from

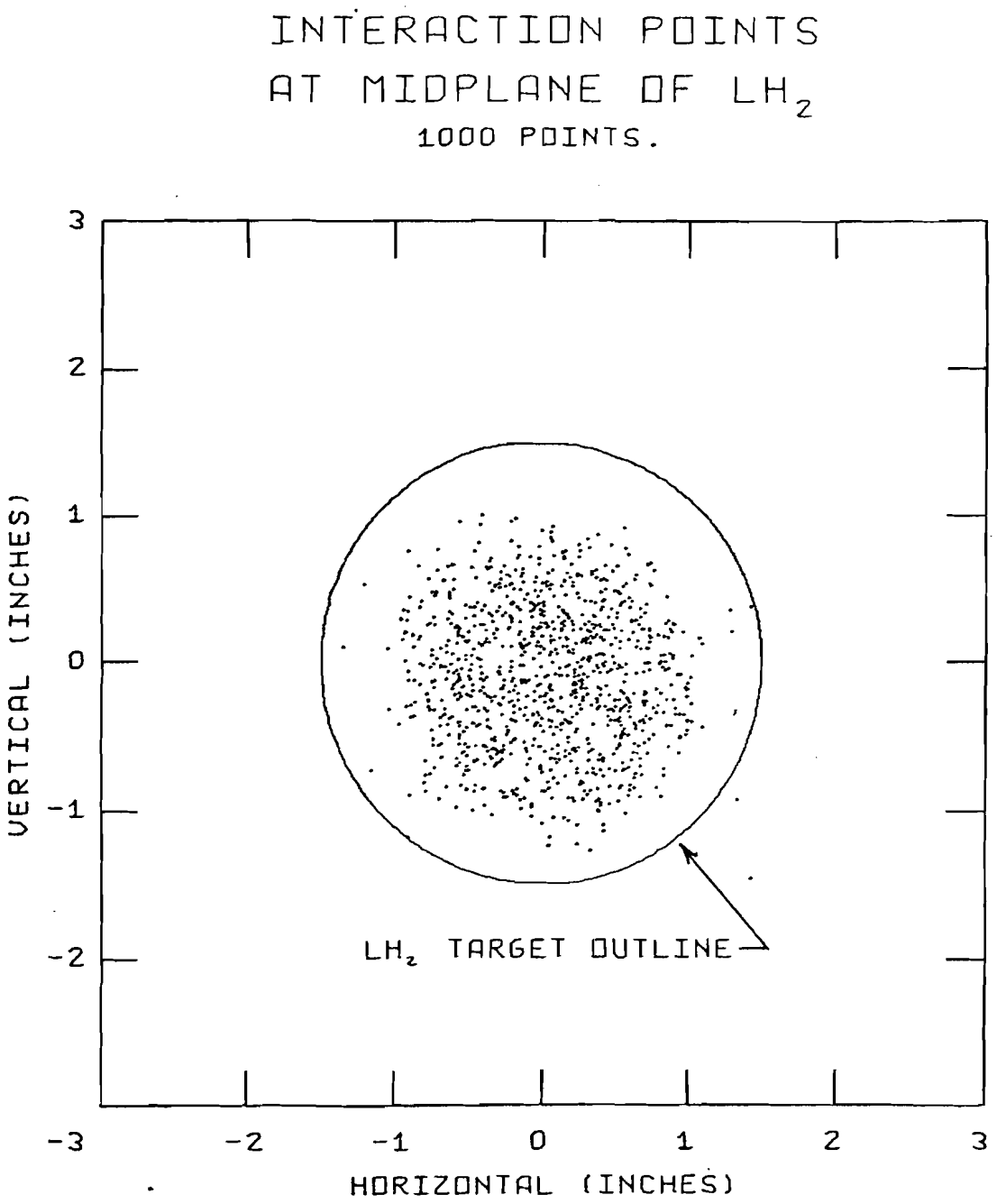

Figure 3. Scatter Plot of the Neutron Beam Intensity

earlier $\gamma+d \rightarrow n+p$ experiments; and $\Delta\Omega_i(T_n)$ is the solid angle averaged over all scattering angles collected with the ith configuration. If there are no systematic errors in the data, then the $F_i(T_n)$ should be identical for all configurations of the apparatus except for slight differences in resolution. In general, the $F_i(T_n)$, calculated as described above, are in good agreement and the best estimate of the spectrum is plotted as the solid curve in Fig. 4. The dashed curve is the estimated error in the spectrum, due primarily to the rather large uncertainties in the normalization of $d\sigma/d\Omega(T_n)$ in the $\gamma+d \rightarrow n+p$ experiments.

3. Liquid Hydrogen Target (LH2 Target)

A drawing of the LH_2 target assembly appears in Figs. 5a and 5b. The flask containing the hydrogen was an aluminum cylinder 7.5 cm in diameter and 1.5 cm long with 4 mil mylar end caps. The total length of the flask along the beam was 6.0 cm. The entire flask was wrapped in ten alternate layers each of 0.25 mil aluminized mylar and 0.25 mil aluminum foil. A reservoir above the flask supplied liquid hydrogen through a fill line entering the bottom of the flask. The target was vented through a line running from the top of the flask to a valve. This valve was open for normal data collection to allow boiling hydrogen to escape but for target empty runs it was closed,

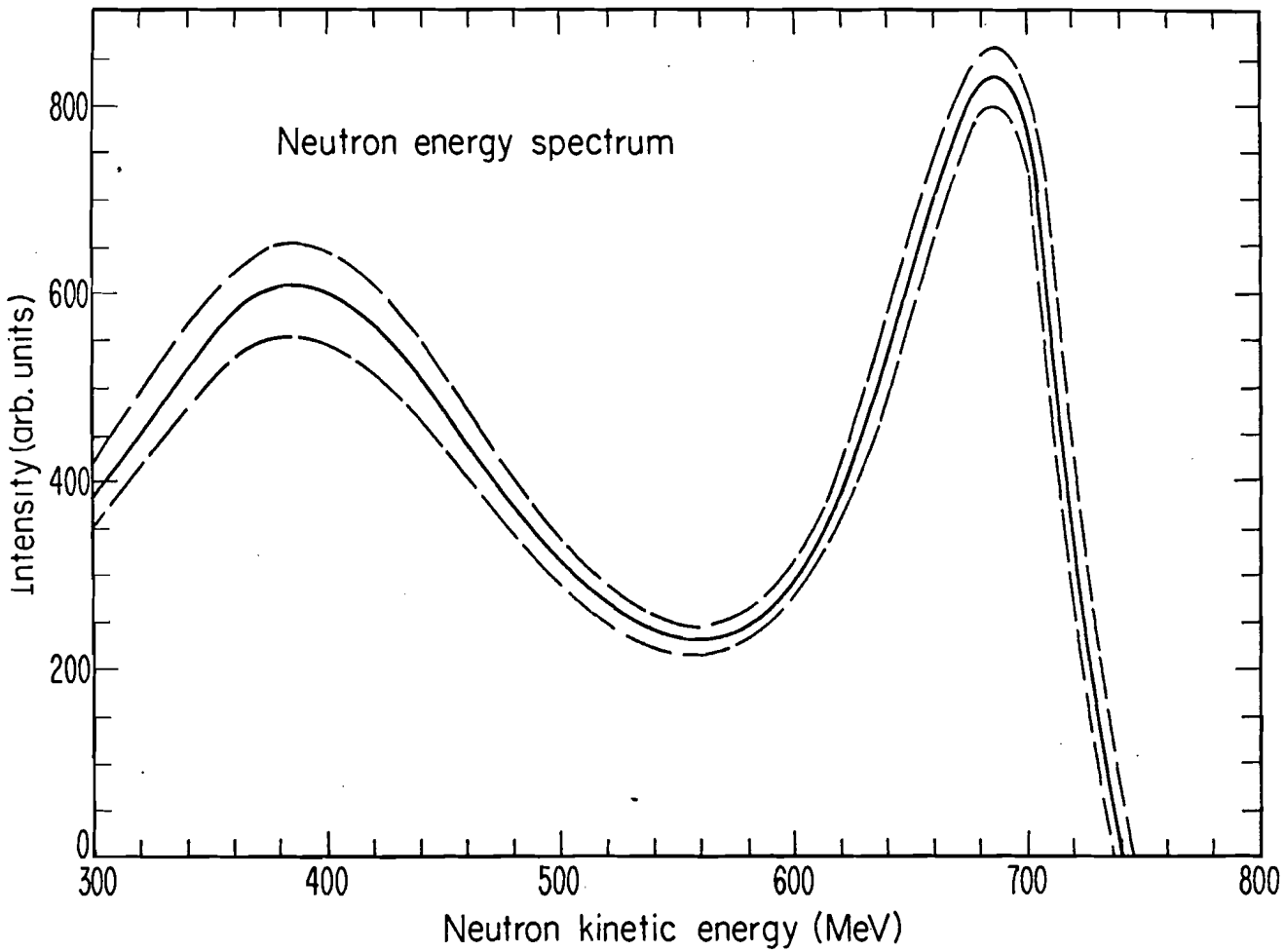

Figure 4. Neutron Beam Energy Spectrum

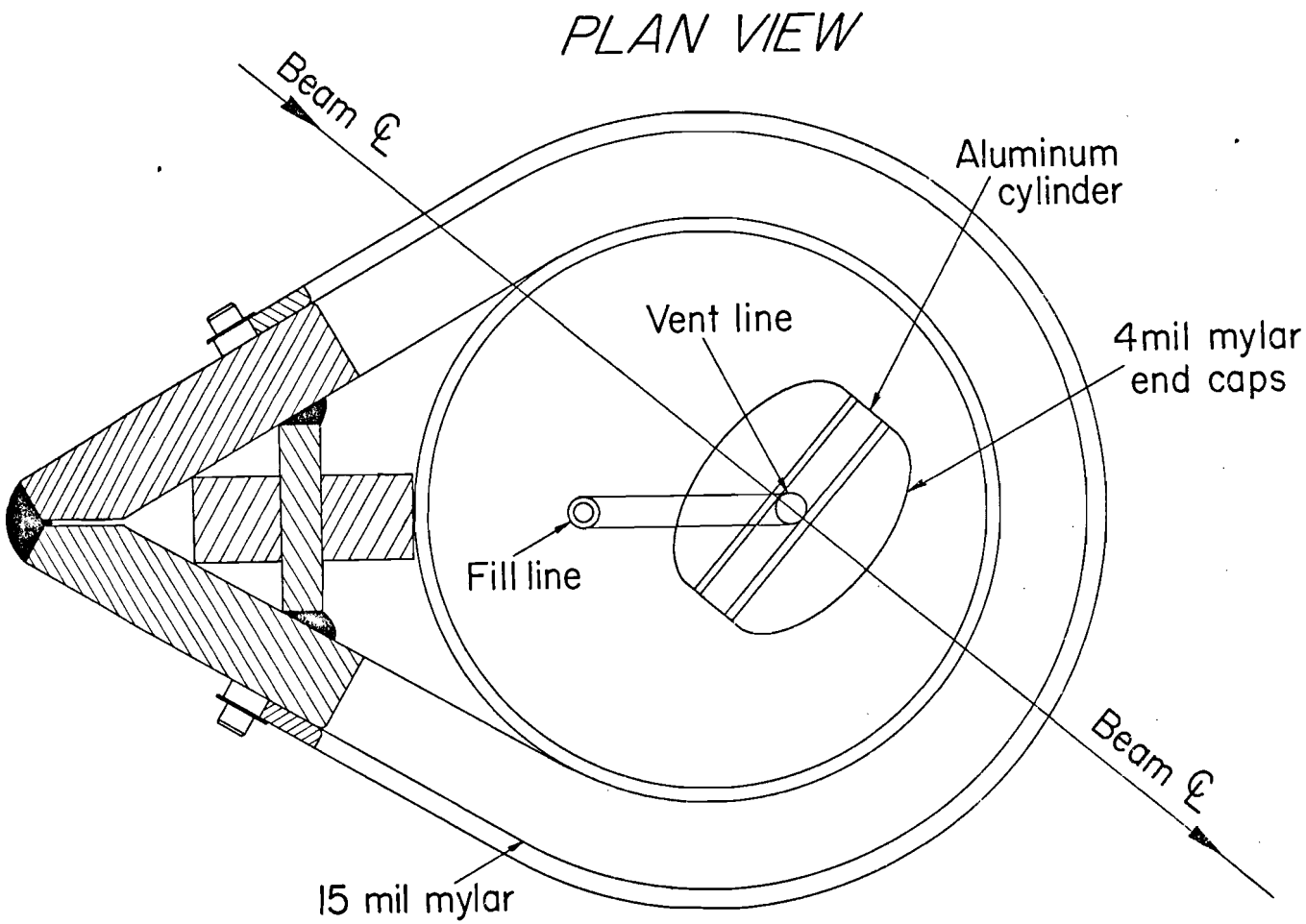

Figure 5(a). Plan View of the Liquid Hydrogen Target

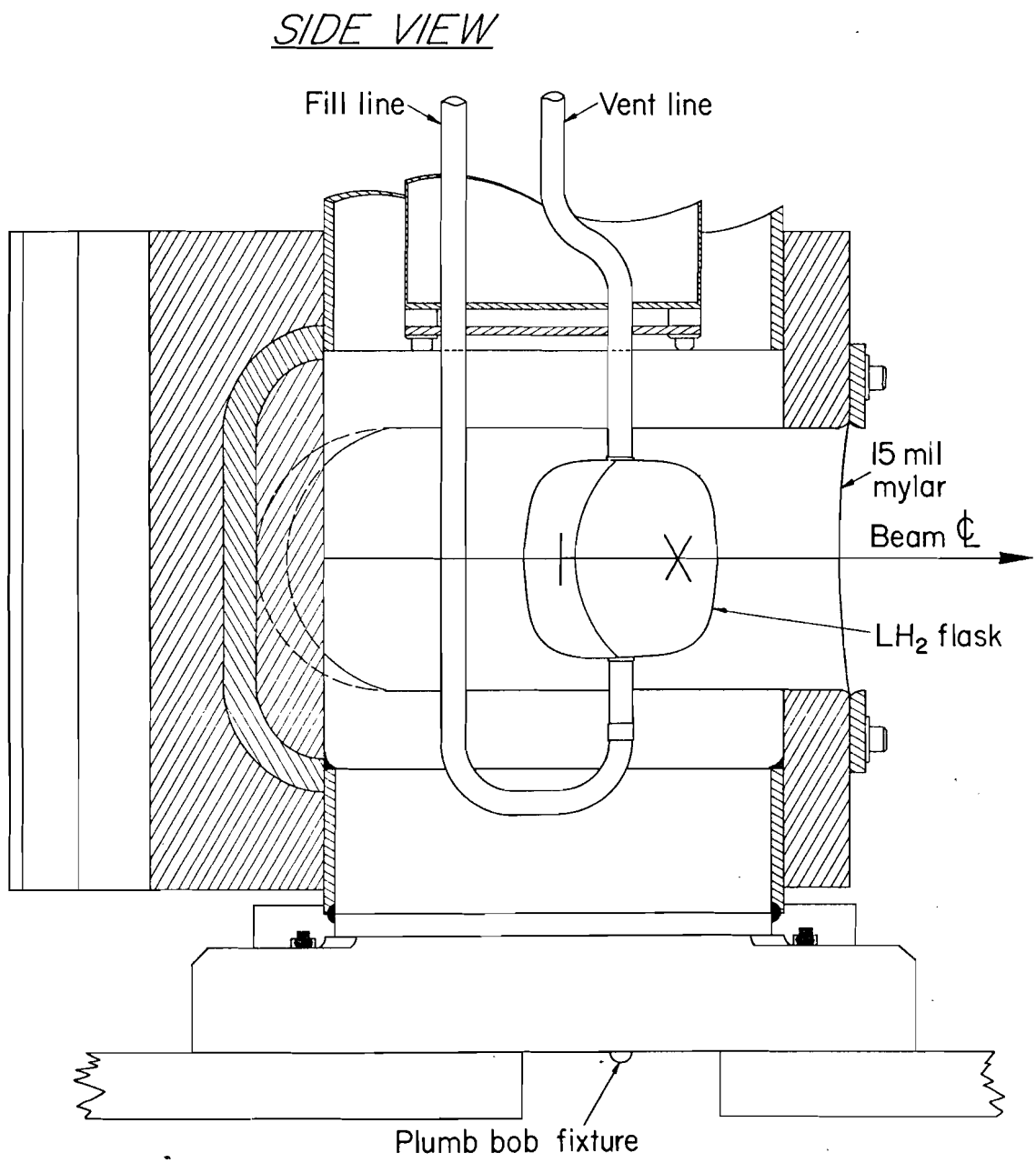

Figure 5(b). Side View of the Liquid Hydrogen Target

thus forcing hydrogen in the flask back into the reservoir. Data from target empty runs were used to correct the $n+p \rightarrow \gamma+d$ angular distribution for background from neutrons interacting in the target walls.

The flask was surrounded by a vacuum jacket consisting of two mylar walls, each 7.5 mils thick. The amount of material in the flask and vacuum jacket was minimized in order to reduce background neutron interactions as well as to reduce Coulomb scattering of the exiting deuteron for $n+p \rightarrow \gamma+d$ interactions.

4. Wire-spark-chamber Spectrometer

a. General Description

The scattering angle and momentum of the deuteron were measured by a spectrometer consisting of four wire spark chambers with magnetostrictive readout, S_1 through S_4, a magnet, and counters D_1 and D_2 as shown in Fig. 2. Two counters, A_1 and A_2, not shown in Fig. 2 were used in anticoincidence and were placed near the phototubes of D_1 and D_2, respectively, in order to clearly define the effective aperture for the deuteron.

b. Wire Spark Chambers

The operation of spark chambers in general, and wire

spark chambers in particular, is reviewed in reference 38. Basically the concept of a spark chamber is simple: two conducting planes are separated by a small distance (≈3/8 inch) and one of the planes is pulsed with high voltage when it is determined, usually with counters, that a charged particle has passed through the chamber. Ions, resulting from the passage of the particle through the chamber, cause a spark between the plane at high voltage and the other plane, held at ground potential. In optical chambers, a stereo photograph is taken of the spark, thus determining a point through which the charged particle had passed. For wire chambers, the conducting planes are wire grids, the wires in each grid perpendicular to those in the other grid. The spark, instead of being photographed, causes current to flow in one wire of each grid and the location of these wires is recorded. The intersection of the two recorded wires, with the assumption that they lie in the same plane, thus determines the point through which the particle passed. Various techniques are available for sensing the wires which carried current, among which is the magnetostrictive readout system utilized in this experiment. In practice, more than two wire planes are generally used and several chambers are employed to determine the trajectory of the particle.

The two wire chambers before the magnet, S_1 and S_2, were constructed at the University of Michigan and were

identical. A photograph of S_2 appears in Fig. 6. Each chamber had two pairs of 3/8-inch spark gaps for a total of four gaps per chamber. Each pair of gaps consisted of two wire planes at ground potential separated by an aluminum plane which was pulsed at 11 kilovolts. Each wire plane consisted of a grid of 20 mil wide by 1 mil thick aluminum strips (wires) etched on a 2 mil thick aluminized mylar sheet. For each chamber, one grid of wires was vertical, one horizontal, and the remaining two were perpendicular to each other and at 45° with respect to the vertical and horizontal grids. Two fiducial wires for each wire plane were accurately located 0.5 inches outside the active area of the plane and were pulsed along with the high voltage. All planes were glued in a conventional fashion to lucite frames to form a completed chamber with an active area 9.75 inches square.

The two chambers after the magnet, S_3 and S_4, were constructed at LRL and are discussed in detail in reference 39. Each chamber had two 3/8-inch gaps formed by four wire planes, each plane consisting of 6 mil aluminum wires spaced 1 mm apart. The orientation of the wire grids was identical to that for chambers S_1 and S_2. The outer two planes were grounded and the inner two were pulsed at 11 kilovolts. The first and last wires of each plane drew current each time the chambers were pulsed and thus served as start and stop fiducials for the readout electronics.

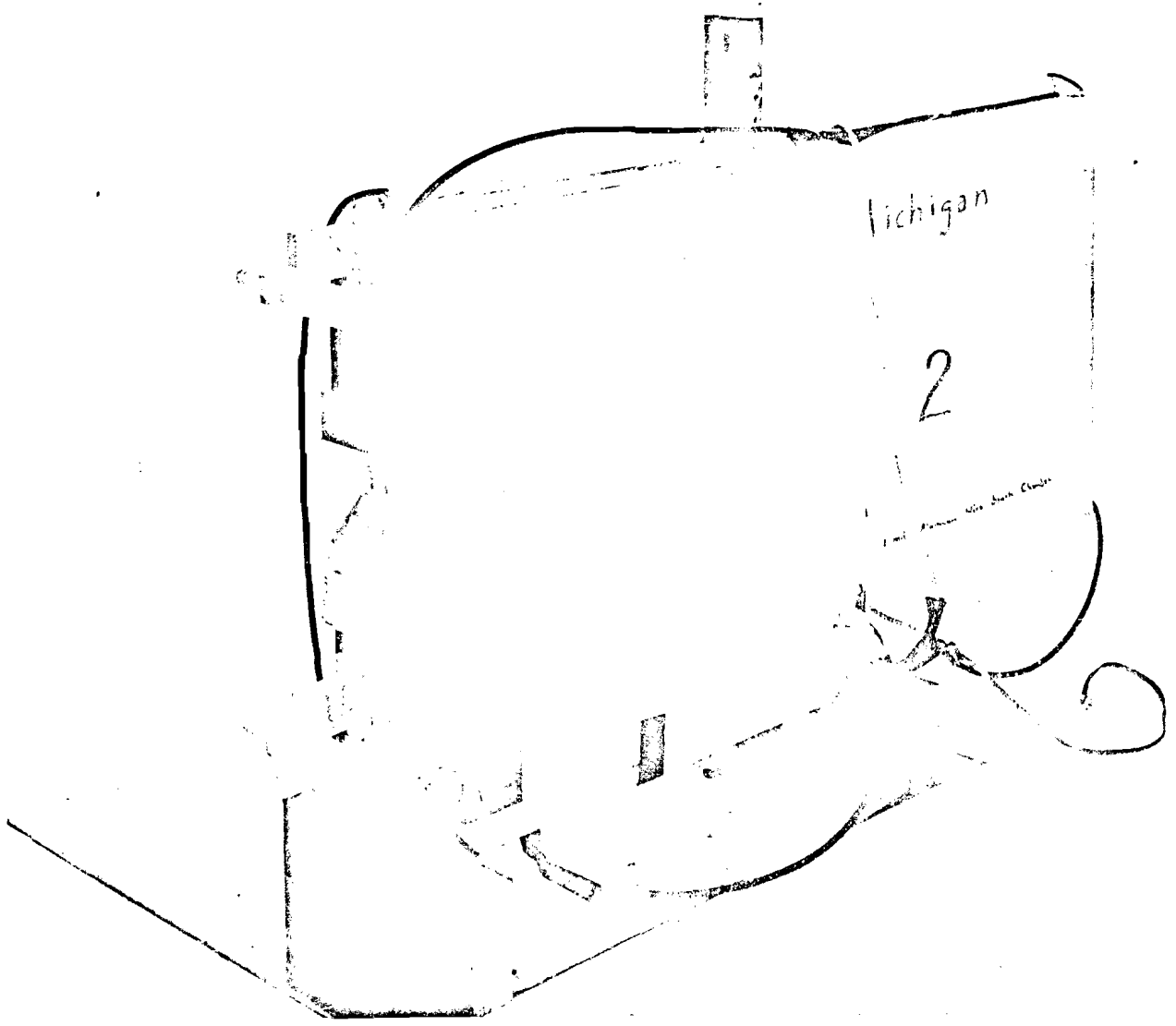

Figure 6. Photograph of Wire Chamber S_2

All the wire planes were glued to an epoxy-fiberglass frame and each chamber had an active area 18 inches by 22 inches.

In operation, all four wire chambers in the experiment were pulsed with high voltage by a triggered spark gap designed at LRL[40]. Mylar windows and gas manifolds on each chamber formed an airtight unit through which a gas mixture of 90% neon and 10% helium was circulated. Ten per cent of the gas mixture was saturated with ethanol which served as a quenching agent to reduce spurious sparking. The recovery time of the chambers was improved by applying a 50 volt clearing field to each gap to remove ions from unrelated events.

The techniques involved in the magnetostrictive readout of wire spark chamber information have been described in detail by many authors[41, 42]. For this experiment, the magnetostrictive sensing unit consisted of a 7 mil magnetostrictive wire mounted on an aluminum bar with a mechanical damping pad at one end and a pick-up coil and a preamplifier at the other. Slots were milled in the chamber frames so the aluminum bar could be inserted with the magnetostrictive wire in close proximity and perpendicular to the wires of the chamber. The output signal of the pick-up coil was approximately 30 Mv which was amplified to 1.5 volts. The first signal from the coil, resulting from current flowing in the "start" fiducial, gated on two 12-bit scalers which counted a 20-MHz pulser.

The second signal, caused by a spark in the active area of the chamber, gated off the first scaler. The second scaler was gated off by the third signal to arrive which was due to either the second fiducial or to a second spark in the active area of the chamber.

For the usual case of only one spark, the first scaler measured the distance, in scaler units, to the wire which sparked and the second scaler measured the distance between fiducials, again in scaler units. Thus if the measured distance in inches between the fiducials was k, the distance, d, from the first fiducial to the wire that sparked is given by

$$d(\text{inches}) = k \frac{C1}{C2}$$

where C_1 and C_2 are the first and second scaler values, respectively.

Four chambers with four wire planes each and two scalers per plane would have required a total of 32 scalers if the scalers had been read in parallel. Instead, a delay-line multiplexing system described in reference 43 was used to reduce the number of scalers to 12. The reduction in the number of scalers was made possible by storing some of the signals from the chambers on a 22-foot long magnetostrictive delay line before digitization. An additional feature of this system was an oscilloscope

display comparing the relative positions of the signals on the delay line to their relative positions after digitization and storage in the computer's memory. This feature provided an excellent on-line monitor not only of the digitizing system but also of the operation of the chambers themselves. Wire planes which were multiple sparking or not sparking at all were easily detectable.

c. Analyzing Magnet

The bending magnet, located between chambers S_2 and S_3, was a 19-ton C-magnet with rectangular pole faces 36 x 16 inches separated by an 8 inch gap. Chambers S_2, S_3, and S_4 were suspended from a large aluminum I-beam bolted to the top of the magnet and iron shields were clamped to the magnet in order to reduce the magnetic field in the region of the chambers. This entire unit was then mounted on a war-surplus gun mount which rested on multi-ton rollers on steel tracks. Thus the solid angle could be easily altered for various kinematic regions of the $n+p \rightarrow \gamma+d$ reaction.

The vertical component of the magnetic field was measured by the LRL magnet group for six currents in the range 980 to 2000 amps. A grid of measurements one inch apart was taken in each of five planes spaced 1.4 inches apart and parallel to the pole faces. Central field values ranged from 10400 to 17500 Gauss.

Figure 7. Photograph of Experimental Area

frame and separated by 3/8 inch to form a four gap chamber. The first plate in each module was stainless steel and had dimensions 33.75 x 33.75 x .025 inches. Each of the remaining four plates consisted of a 45 mil lead sheet laminated between two stainless steel plates with dimensions 33.75 x 33.75 x .018 inches. Mylar strips 15 mils thick and 0.5 inches wide were glued to the perimeter of the metal sheets in order to prevent "edge-sparking" when the chambers were pulsed with high voltage. Small lucite spacers, 1/4-inch square, were placed at the center of the chamber between each pair of plates in order to maintain a uniform 3/8-inch gap. Each module had an active area approximately 30 inches square and a total thickness of about 1.8 inches. The amount of material encountered in each module by an incident photon was equivalent to about one radiation length.

In operation, the center and outer plates of each module were held at ground potential and the other two plates were pulsed with 11KV by the triggered spark gap described in reference 40. A gas mixture of 90% neon and 10% helium was circulated through the modules and a 50 volt clearing field was applied to each gap. Ten per cent of the circulating gas mixture was saturated with ethanol to reduce spurious sparking.

The ten modules were spaced 1-3/8 inches apart and eight pairs of plastic scintillator counters were placed

between the first nine modules in order to detect the charged particles from the converted photon. Each counter of a pair had dimensions 27 x 12 x 1/2 inches and thus the active area of the chamber for photon detection was 27 x 24 inches. The counters were coupled with lucite light pipes to RCA 6810A photomultiplier tubes and the two signal cables of each pair were passively OR-ed at the gamma chamber.

Stereo views of the chamber (top and side) were transmitted to a Mitchell double frame 35 mm camera by an optical system consisting of two lucite field lenses and four mirrors. The two views were recorded on Kodak 2498, a film with a reversal type emulsion on an estar base and with high speed perforations. The aperture setting on the camera was midway between f/5.6 and f/8. Fig. 8a is an actual photograph from a calibration event. The long lines were neon lights used as control fiducials by the automatic scanning system which measured the film. The regularly-spaced lights were calibration fiducials and were flashed only at the start of each run to provide coordinate information to the analysis programs. Six of these calibration fiducials were also flashed for every event collected during the course of the experiment in order to ensure accurate reconstruction of each event. The left-hand view in Fig. 8a is the top view of the chamber and includes the data box which provides, via nixie lights,

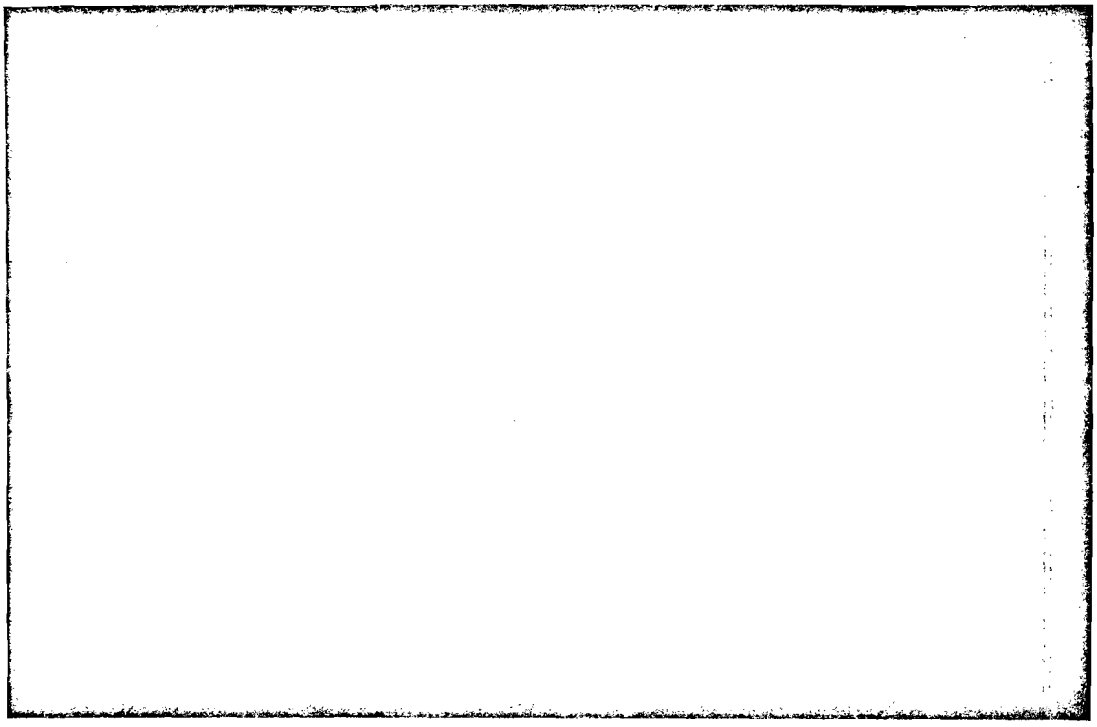

Figure 8a. Gamma Chamber Photograph of Calibration Event

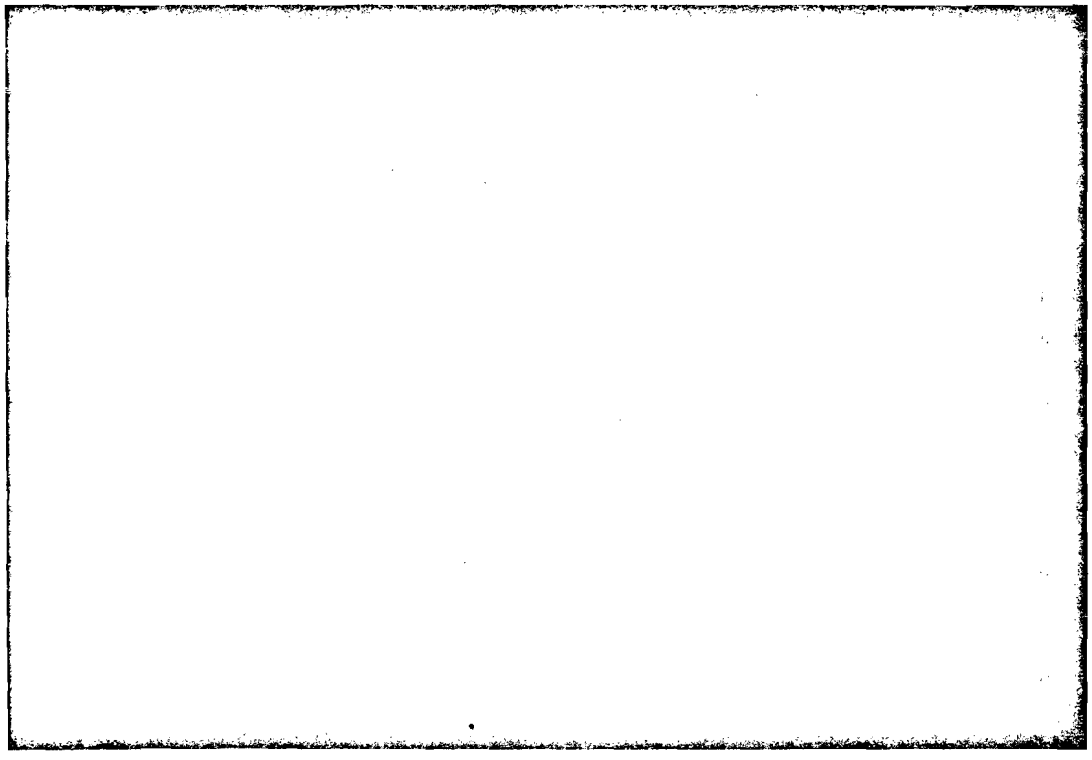

Figure 8b. Gamma Chamber Photograph of Real Event

run and event number identification for the frame. The frame in Fig. 8a is event number 15 of run number 1086. The digits of the event number were also coded as BCD bits to facilitate event identification by the analysis programs.

6. γ-shower Anti-counters

Three lead-scintillator anti-counters (A_3, A_4, and A_5) partially surrounded the LH_2 target in order to veto events from the reaction $n+p \rightarrow \gamma+\gamma+d$ when one of the two gammas entered the gamma chamber and the other entered one of the three anti-counters. The counters were identical and each was constructed of eight rectangular blades of plastic scintillator, each blade having dimensions 15.5 x 15.5 x .025 inches. Seven lead sheets, each 0.11 inches thick, were interleaved between the plastic blades for a total of 3.4 radiation lengths of lead in each counter. Alternate scintillator blades were channeled via lucite to one of two lucite light pipes, each viewed by an RCA photomultiplier tube.

7. Neutron Beam Monitors

The neutron beam was continuously monitored by the counter arrangement depicted schematically in Fig. 9. Three sets of counters (K, L, and M) were used to provide a

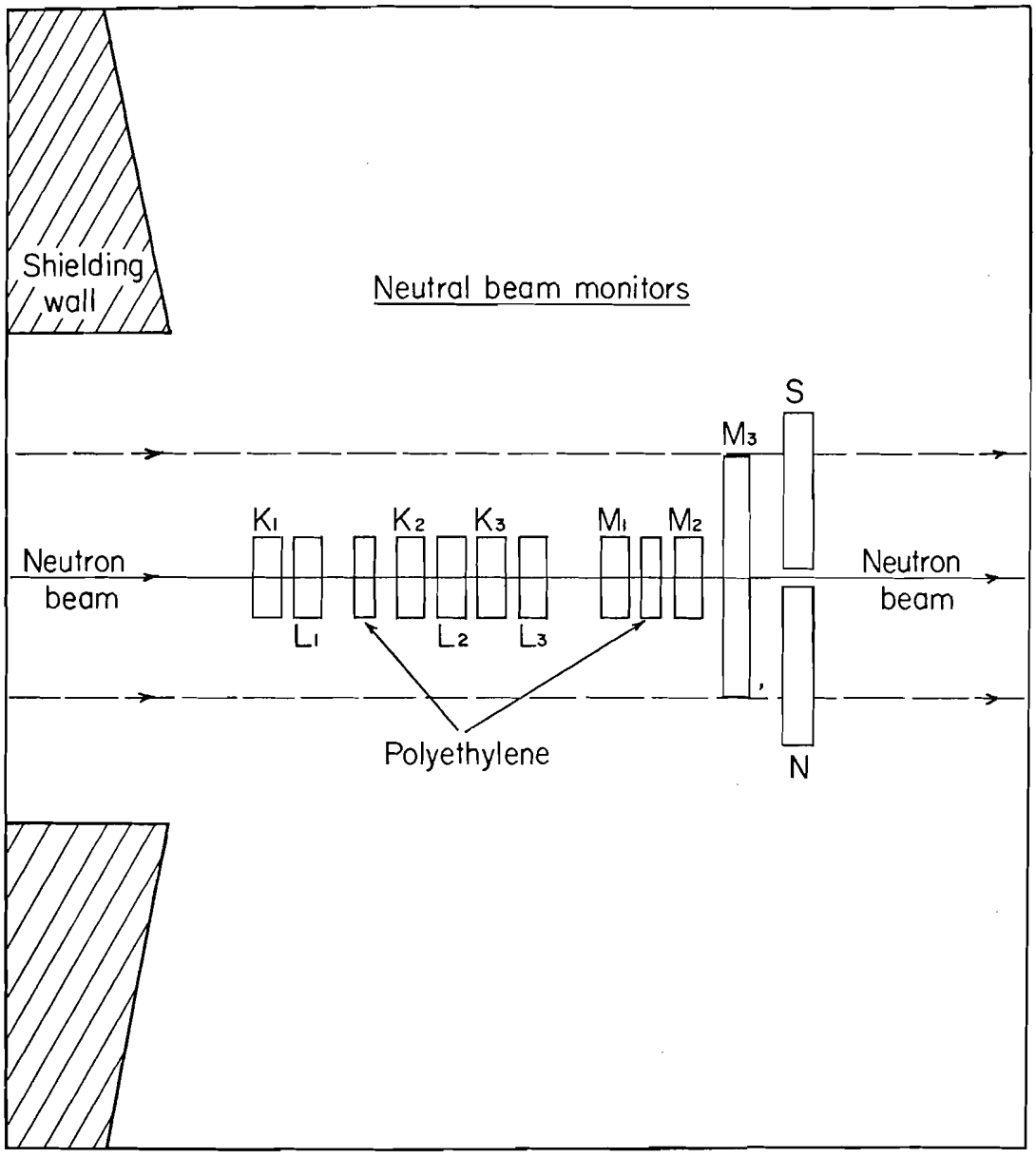

Figure 9. Schematic of Neutral Beam Monitor

redundant measurement of the beam's relative intensity. The K and L counters and counters M_1 and M_2 were one inch square and 3/8 inch thick. Counter M_3 was 3/8 inch thick and 3 inches square. The beam, at counter M_3, was approximately circular with a diameter of 3 inches. Polyethylene blocks, placed after the first counter in each set, created charged particles which the second and third counters detected in coincidence. The first counter was placed in anticoincidence to ensure that the second and third counters were not counting primary charged particles in the beam.

Counters N and S, both 2 inches square and 3/8 inches thick, were used to align the beam horizontally. Polaroid film was also used to check the alignment of the beam.

8. Electronics

A simplified schematic of the counters and the associated electronics appears in Fig. 10. In general, the counters were connected to Chronetics 101 discriminator modules[44] and coincidences were formed using Chronetics 103 modules. The event trigger consisted of a coincidence between D_1, D_2, any of the counters in the gamma chamber, and none of the anti-counters. The output signal of the event trigger flashed fiducials, triggered the spark gap for the chambers, initiated data input to the PDP-5 computer, gated off the electronics for 200 msec and advanced

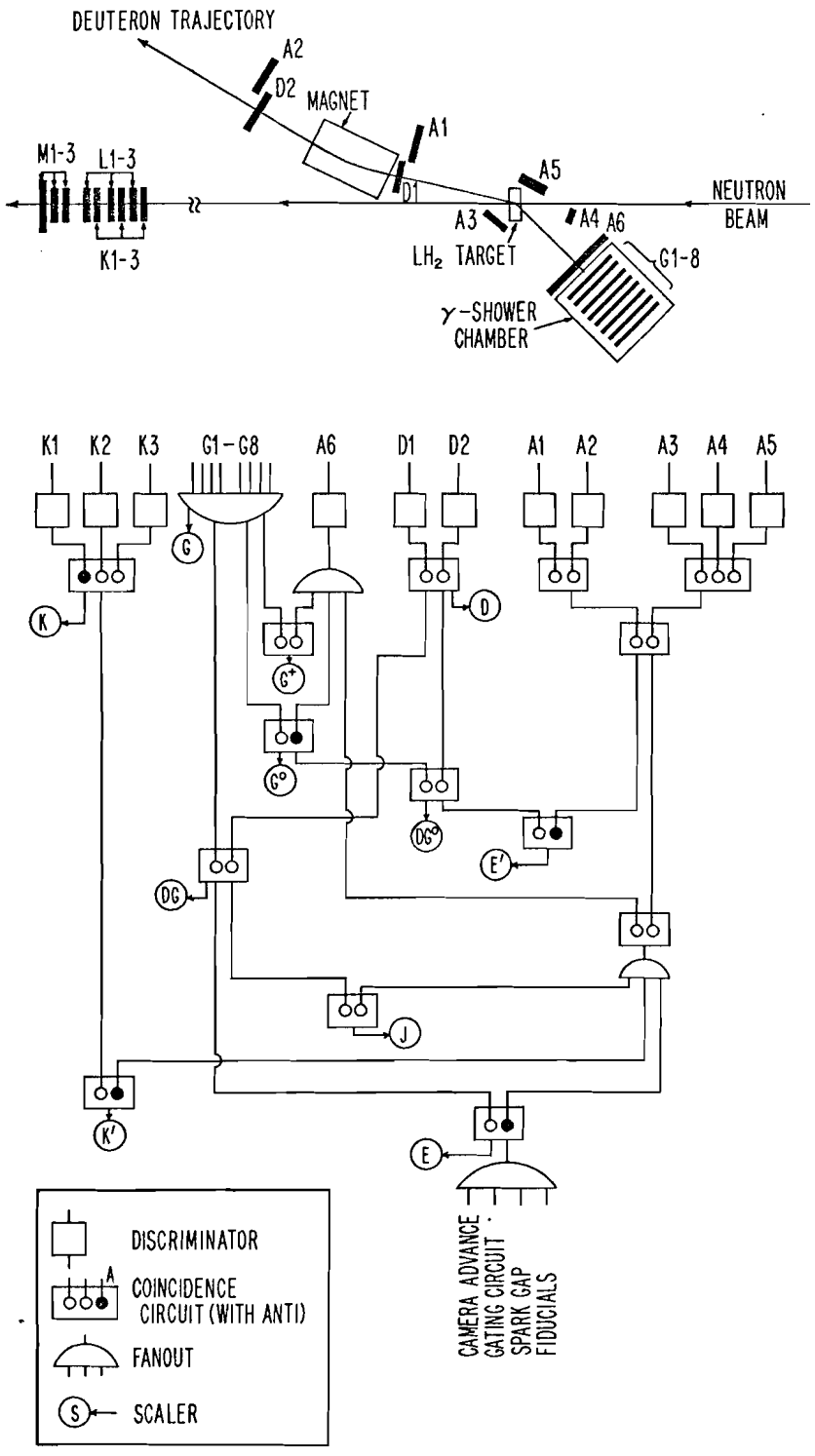

Figure 10. Simplified Schematic of Electronic Logic

the camera. For each event, four time of flights were recorded and 16 bi-stable flip-flops or latches identified the counters that fired. In addition, various singles and coincidence rates were continuously recorded by 12 1-megacycle and 12 10-megacycle scalers.

Figure 10 is incomplete in that it does not include all the coincidences that were formed nor all the rates that were scaled. In particular, "accidentals" in many of the more important coincidences were continuously monitored by delaying one of the inputs to the coincidence by 51 nanoseconds, the time between rf bursts from the cyclotron. A complete list of the singles and coincidence rates that were scaled appears in Table 1.

The four time of flights (TOF's) that were recorded are listed in Table 2. Each TOF was measured, with an accuracy of ±1/2 nanosecond, by a system that consisted of a time to height converter (THC) and an analog to digital converter (ADC). Of the four TOF's listed, only the D_1-D_2 TOF was valuable in the analysis in that it provided the best measure of the mass of the charged particle in the spectrometer.

9. PDP-5 On-line Computer

A Digital Equipment Corporation[45] PDP-5 computer with a 4096 word memory was used on-line to record data from the experiment and to continuously monitor the

TABLE 1

SCALED SINGLES AND COINCIDENCE RATES

K	$= \bar{K}_1 K_2 K_3$	K'	$= K\bar{A}_s$
L	$= \bar{L}_1 L_2 L_3$	L'	$= L\bar{A}_s$
M	$= \bar{M}_1 M_2 M_3$	M'	$= M\bar{A}_s$
D	$= D_1 D_2$	G	$= G_i$ (any $i=1,8$)
DG	$= DG$	E	$= (DG)\bar{A}_s$
G^o	$= G\bar{A}_6$	E'	$= (DG^o)\bar{A}_7$
DG	$= DG^{(d)}$	DG^o	$= D^{(d)}G^o$
J	$= (DG)A_s$	J	$= (DG)A_s^{(d)}$
G^+	$= GA_6$	G^+	$= A_6 G^{(d)}$
T	= Live Time	D	$= D_1 D_2^{(d)}$

Legend

$S = XX_1$: X and X_1 in coincidence

$S = X\bar{X}_1$: X_1 in anticoincidence

$S = XX_1^{(d)}$: Accidentals for coincidence; X_1 delayed by 51 nsec.

$A_7 = A_1 A_2 A_3 A_4 A_5$

$A_s = A_6 A_7$

TABLE 2

TIME OF FLIGHTS

LABEL	START PULSE	STOP PULSE
D_1-D_2	D_1	D_2
D_1-G	D_1	G (any G_i, i=1,8)
Beam	Pulse from second Dee of cyclotron	Event trigger(E)
Cycle	Event trigger(E)	Next cyclotron rf pulse

operation of the apparatus. Data from each event, consisting of 45 12-bit words, were stored sequentially in a 540 word buffer until the buffer was full. Ten of the more important scaler values were then strobed and, along with the entire data buffer, were written on magnetic tape at 556 bytes per inch. The remainder of the computer's memory, 3511 words, was used for the storage of control and monitor programs. The monitor programs consisted primarily of routines to organize and display, on an oscilloscope, information about the operation of the wire spark chambers. A data break facility suspended the operation of the monitor programs whenever an event occurred and resumed their operation after the data from the event had been recorded.

C. DATA COLLECTION

Data were collected simultaneously for all neutron kinetic energies in the range 300 to 720 MeV for each scattering angle at which the angular distribution was measured. The five scattering angles had nominal values $\theta^*_{dn} = 30^\circ$, 60°, 90°, 120°, and 150° where θ^*_{dn} is the c.m. angle of the deuteron relative to the neutron. For each angle, the gamma chamber and deuteron spectrometer were positioned appropriately and data were collected over a period of 2-3 weeks. After completing the first measurement at all five angles, a second measurement of the angular distribution was made, identical with the first

except for a lower statistical precision. The second measurement was completed in a total of 10 days and was intended to serve as a check of long-term drifts in the neutron beam monitors as well as a check of the surveying for the first measurement. A total of 1.2×10^6 events were collected for the two measurements with the second measurement comprising 15% of the total sample.

Two different media, film and magnetic tape, were necessary for recording the data describing each event. The conversion point of the photon in the gamma chamber was recorded on film whereas the wire spark chamber and counter information was stored on magnetic tape. Run and event numbers were also recorded on both film and tape in order that the information from the two media could be correlated by subsequent analysis programs.

A stereo photograph of a photon-initiated shower from a typical event appears in Fig. 8b. The spatial coordinates of a point on the photon's trajectory could be determined by measuring the vertex of the shower in each view. Approximately 4000 such photographs were collected on each 500 foot roll of film used in the experiment. The developed film was usually available two hours after exposure and was checked immediately to ensure that the chamber and camera were operating properly. Measurement of most of the film was generally not undertaken immediately although selected runs were measured and analyzed while the

experiment was in progress.

The information from each event that was recorded on magnetic tape by the computer required 45 12-bit words. Thirty-two words were required for the scaler information from the magnetostrictive readout of the wire spark chambers (2 scalers per wire plane x 4 wire planes per chamber x 4 chambers = 32 scaler values). Five words were required for the four time of flights that were measured and two words were needed for the event number. The information specifying which counters fired for the event was coded in two words or 24 binary bits. A value of one for a bit corresponding to a particular counter indicated that the counter had fired, a zero that it had not. The remaining four words in the block of 45 were blanks resulting from a peculiarity of the delay-line multiplexing system used for the magnetostrictive readout.

Before being written on magnetic tape, the information from each event was monitored by the computer. The most useful monitoring task that the computer performed was a count of the number of times that each wire plane had multiple sparks or no sparks at all. This count was displayed on the oscilloscope in a convenient fashion and was an immediate indication of chamber malfunction. Other monitoring information resulting from the PDP-5 included counter frequency curves and displays of the time of flight and wire chamber distributions.

In addition to the monitoring performed by the computer, the values of the scalers listed in Table 1 were compared, after each run, to their values in previous runs. In general, the monitoring activity during the experiment resulted in minimal losses of data due to equipment malfunctions.

III. DATA ANALYSIS

A. GENERAL DESCRIPTION

The data from this experiment were conveniently divided into two groups: (1) magnetic tape from the PDP-5 computer, comprised mostly of wire-chamber spectrometer data, and (2) film from the gamma chamber. The overall scheme for analyzing and combining the two groups of data is depicted in Fig. 11. For the spectrometer data, the scaler values from the wire chambers were converted to coordinates of sparks in a coordinate system centered on the magnet. These spark coordinates were used to calculate the momentum of the charged particle and the momentum was then combined with the time of flight measurement to determine the mass of the particle. For the gamma chamber data, the film was first measured by an automatic scanning system consisting of a Vidicon television tube, associated electronics and a PDP-5 computer which wrote the data on magnetic tape. Subsequent computer programs condensed the data and located the vertex of the photon shower. The two groups of data were then merged by a kinematic fitting routine which calculated a "goodness" number (χ^2-value) for the event. Distributions of these "goodness" numbers were then plotted and background events were subtracted with the aid of similar distributions from a Monte Carlo program.

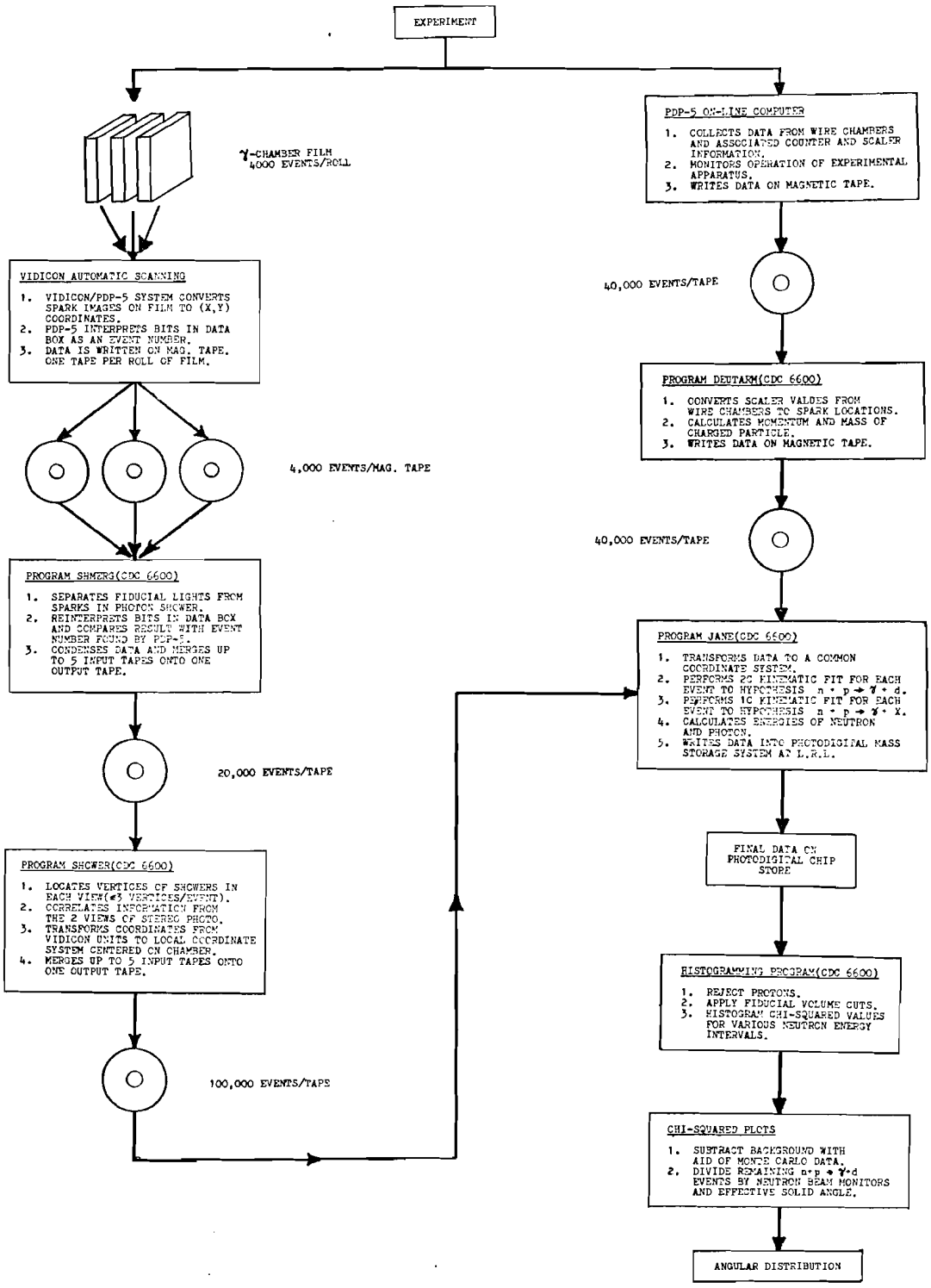

Figure 11. Schematic of the Data Analysis Procedure

The events remaining after the subtraction, the $n+p \rightarrow \gamma+d$ yield, were then normalized by the neutron beam monitors. The angular distribution finally resulted by correcting the yield for the effective solid angle subtended by the apparatus, determined by another Monte Carlo program. Each step in the analysis process is described in detail below.

B. GAMMA CHAMBER DATA

1. Automatic Scanning System

The stereo photograph displayed in Fig. 8b is typical of the 1.25 million gamma chamber photographs. The automatic scanning system used to measure the photographs is described in detail in reference 46. Basically the system consisted of a Vidicon television tube positioned to scan the film with an electron beam sweeping parallel to the image of the spark chamber's plates. Each sweep was digitized by eight 10-bit, 20 Mc scalers which were reset at the beginning of each sweep by the "start" fiducial, the long neon light visible in Fig. 8b. The first scaler was gated on by this start fiducial and each time the electron beam encountered a bright image on the film one of the seven remaining scalers was gated on. All scalers were gated off by the "stop" fiducial, another neon light, and the sweep number and scaler values were then recorded by the PDP-5 before the next sweep began. Every bright image

on the film (sparks, fiducial lights, and the data box) was thus converted to rectangular coordinates by the 256 digitized sweeps. The PDP-5 computer interpreted the coordinates corresponding to the bits in the data box and translated the information into an event number. All of the coordinate data and the event number were then written on magnetic tape.

The scanning system was capable of measuring 3000 frames (2 frames/event) per hour. The image resolution parallel to the chamber plates was .07 mm and perpendicular to the plates it was 0.15 mm. The demagnification from chamber to film was 32/1 so the corresponding resolutions for locating the spark in the chamber were 0.1 inches and 0.2 inches, respectively. Since the gap width in the chamber was 3/8 inch, each spark was recorded an average of 1.9 times. Lens distortions and electronic drifts in the Vidicon system were removed by subsequent analysis programs as described below.

2. Computer Data Reduction

SHMERG, a program written for a Control Data Corporation[47] 6600 computer (CDC 6600), accepted as input the magnetic tapes from the Vidicon/PDP-5 scanning system. In general, the two views from each event were processed separately and no attempt at correlation was made at this stage. The first ten events on each tape were calibration

events, digitized representations of the photograph in Fig. 8a. Since each calibration light was 0.5 inches long, it had been digitized several times by the scanning system and thus was represented on magnetic tape by several coordinate pairs. SHMERG calculated, from all ten events, the average value of these coordinate pairs for each light and wrote the average values on magnetic tape as a single calibration event. For actual data events, SHMERG isolated the coordinates corresponding to the six fiducial lights which were flashed for each event (see section II-B-5) and maintained a weighted average of their values from event to event in order to correct for electronic drifts in the automatic scanning system. For the top view (left-hand view in Fig. 8b), SHMERG interpreted the data box coordinates as an event number and checked this number with that found previously by the PDP-5. The remaining data in both views, consisting of the coordinates of sparks in the chamber's active area, were then written on magnetic tape along with the event number and the averaged fiducial information. It was usually possible to merge five input tapes with 4000 events per tape onto one output tape containing 20,000 events.

The output tapes from SHMERG served as the input tapes to the next program in the analysis chain, SHOWER. The first event encountered on tape by SHOWER was a calibration event consisting of the average values, in Vidicon units,

of the coordinate pairs (X_i, Y_i) describing the calibration lights in each view. The coordinates of these lights in inches in a system centered on the gamma chamber (x_i, y_i) had been previously input to the program and thus the program was able to calculate, by a least-squares fit, the transformation from Vidicon units to a local coordinate system attached to the chamber. This transformation corrected for distortions in the film image caused by non-uniformities in the Vidicon tube and the lucite field lenses. For actual data events, SHOWER used a simple algorithm to locate the vertices of up to three photon showers in each view. The common coordinate for the two views, the depth into the chamber, was then used to correlate the vertices if more than one shower occurred in the event. The fiducial values were then checked to detect any drift in their values compared to the calibration event. If the drift was more than an acceptable minimum, a correction was calculated that would translate the fiducials back to their original locations. This same correction was applied to the vertices of the showers and the transformation from Vidicon units to the chamber coordinate system was then made. For each event, the program recorded the event number, the number of showers detected, the three spatial coordinates specifying the vertex of each shower and the number of sparks in each shower. Five input tapes with 20,000 events per tape were usually merged onto one

output tape containing 100,000 events. This tape contained the final gamma chamber data required as input for the kinematic fitting program.

3. Gamma Chamber Efficiency

The overall efficiency of the γ-chamber system for detecting and recording photons from $n+p \rightarrow \gamma+d$ involved three factors: (1) the probability that a photon which entered the chamber would be converted to an electron-positron pair, (2) the probability that the pair from the converted photon would be detected in at least one of the eight pairs of counters in the chamber and (3) the efficiency of the scanning system and computer programs for correctly digitizing, identifying and recording the vertex of the photon shower.

The thickness of lead, stainless steel and plastic scintillator in the chamber was equivalent to more than ten radiation lengths of material. Thus it was expected that the probability for photon conversion in the chamber would be essentially 100%. Figure 12 is a plot of the distribution of photon conversion points (vertices of the photon showers) as a function of the depth of the vertex in the chamber for a sample of $n+p \rightarrow \gamma+d$ events with photon energies from 120 MeV to 475 MeV. The sample was collected at $\theta^*_{dn} = 120^o$, a kinematic region which is favorable to the reaction $n+p \rightarrow \gamma+d$ with the background

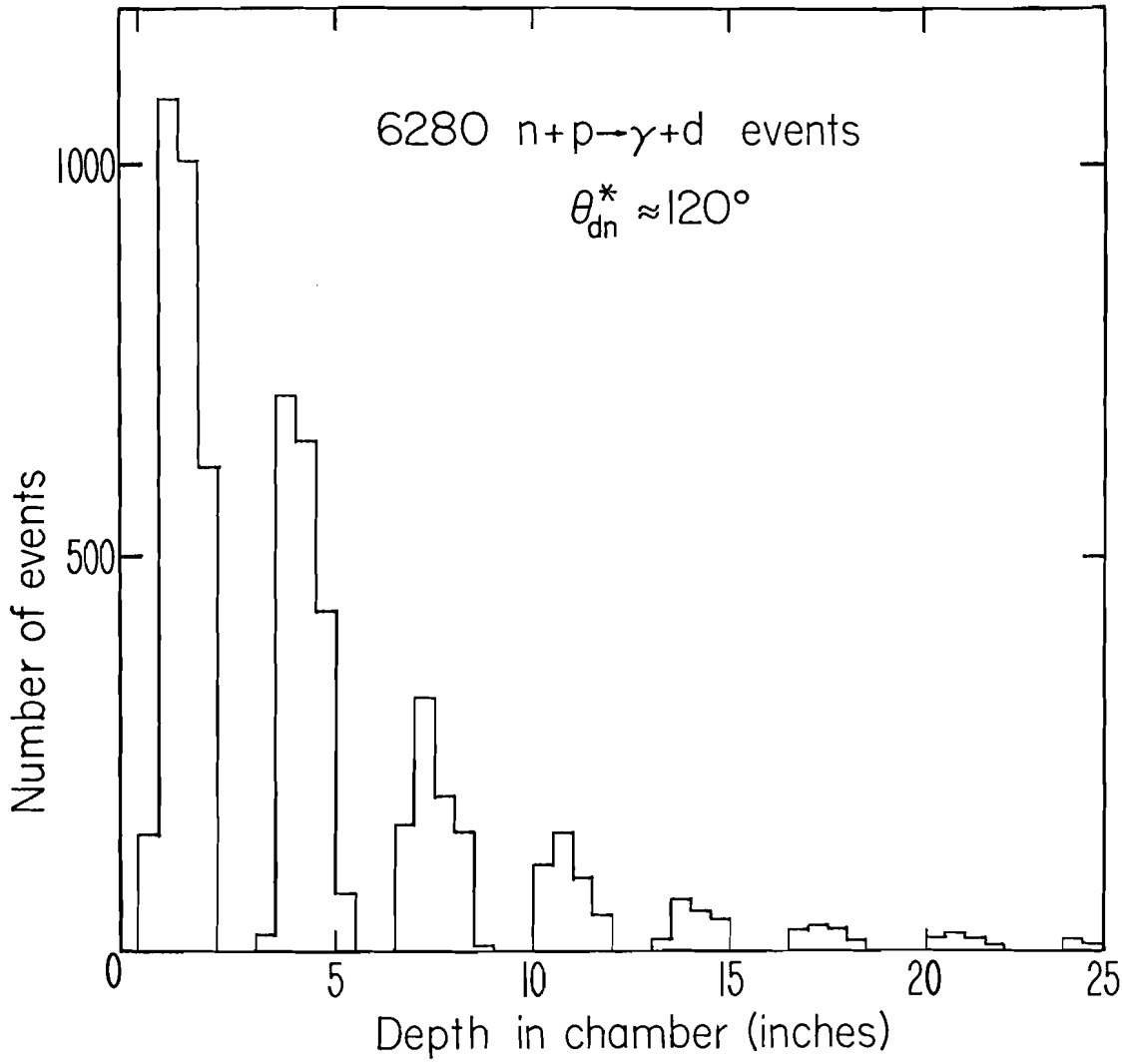

Figure 12. Photon Conversion Points in the γ-chamber

contamination comprising less than 2% of the total sample. Eight of the ten individual spark chamber modules are visible in the plot, and it is clear that the distribution extrapolates to approximately zero events by the tenth module. Thus the expectation of 100% photon conversion probability was empirically confirmed.

Calculation of the second factor, the probability that the pair, once formed, would be detected in one of the eight pairs of counters, was somewhat more complicated. Two theoretical estimates of this probability were made. The first estimate utilized the results of a Monte Carlo study of shower production[37], and the conclusion was that the triggering efficiency of the chamber was essentially 100% for photon energies greater than 80 MeV. The second estimate resulted from an independent Monte Carlo program written explicitly for another experiment[48] which used the same γ-chamber over approximately the same range of photon energies. For that experiment, two or more pairs of γ-chamber counters were required in the event trigger and the efficiency was calculated for that mode of operation. The calculated efficiency is plotted as a function of the photon energy in Fig. 13, and it can be seen from this plot that the chamber is >97.5% efficient for all photon energies greater than 100 MeV. The chamber is certainly more efficient if only one pair of counters is required in the event trigger, as is the case for this experiment, and

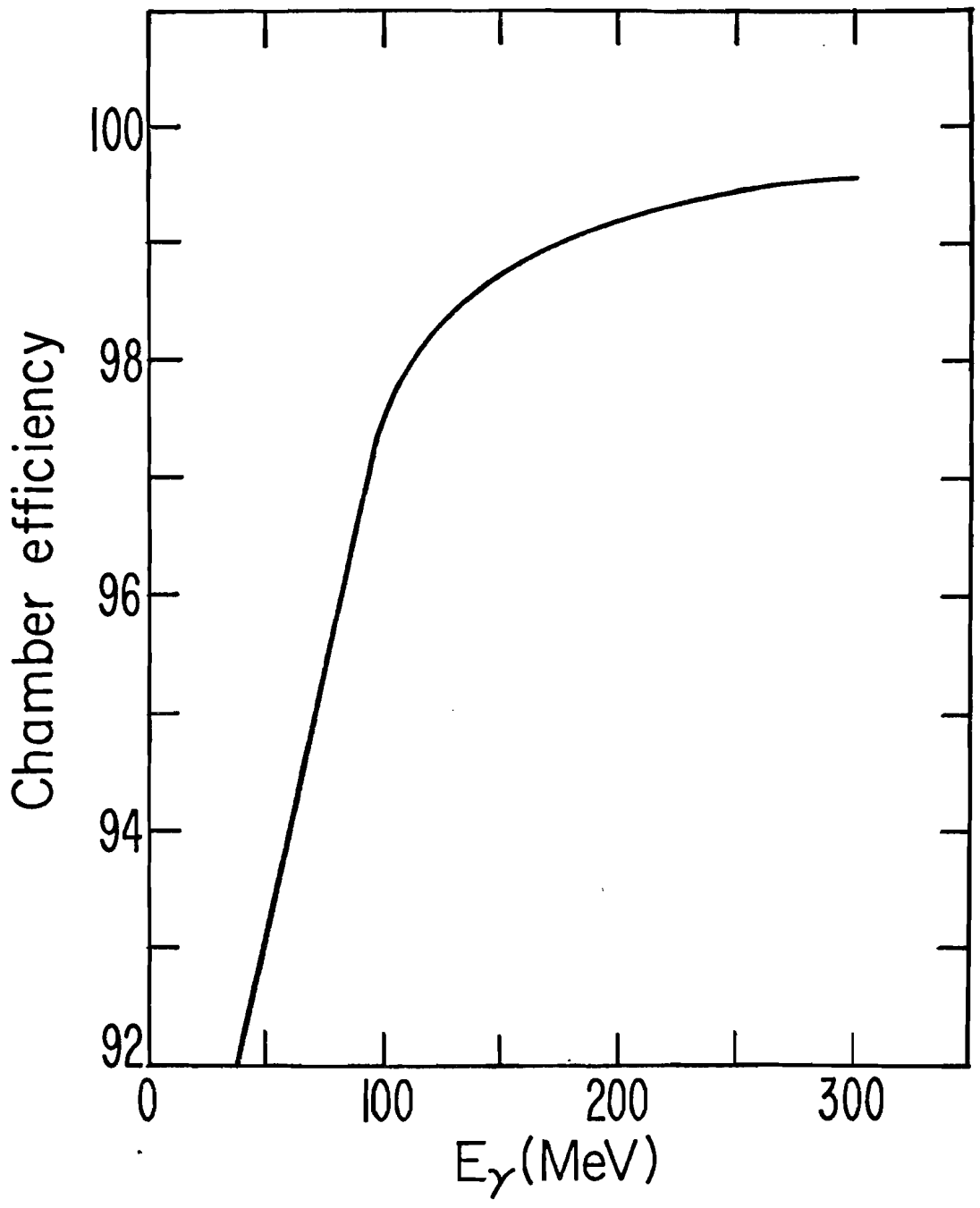

Figure 13. Calculated Efficiency of the Gamma Chamber

consequently the second estimate of the efficiency is consistent with the 100% efficiency from the first estimate.

In addition to the two theoretical estimates of the chamber efficiency, some empirical considerations indicated that the chamber was ≈100% efficient for all photon energies >100 MeV. Figure 14 is a histogram of the number of events in which n trigger counters fired for each event (n ranges from one to eight). The sample of events comes from the previously discussed kinematic region favorable to $n+p \rightarrow \gamma+d$. The smooth curves were hand drawn through the center of each bin, and the important point is that these curves extrapolate to zero events for n = 0 for all the photon energy, E_γ, intervals thus indicating an efficiency consistent with the theoretical efficiency of 100%.

Figure 15 is a scatter plot with the number of sparks in each photon shower and the photon energy for the event as the two coordinates. It should be pointed out that the few events in Fig. 15 with a small number of sparks and a large photon energy are almost certainly background events for which the photon energy was incorrectly assigned. The photon energy assignment is discussed in Section III-D. The sample of events for the plot was again taken from the kinematically favorable region and consists of 98% $n+p \rightarrow \gamma+d$ reactions. The average number of sparks in each shower is approximately a linear function of the photon energy, and a linear extrapolation to E_γ = 100 MeV

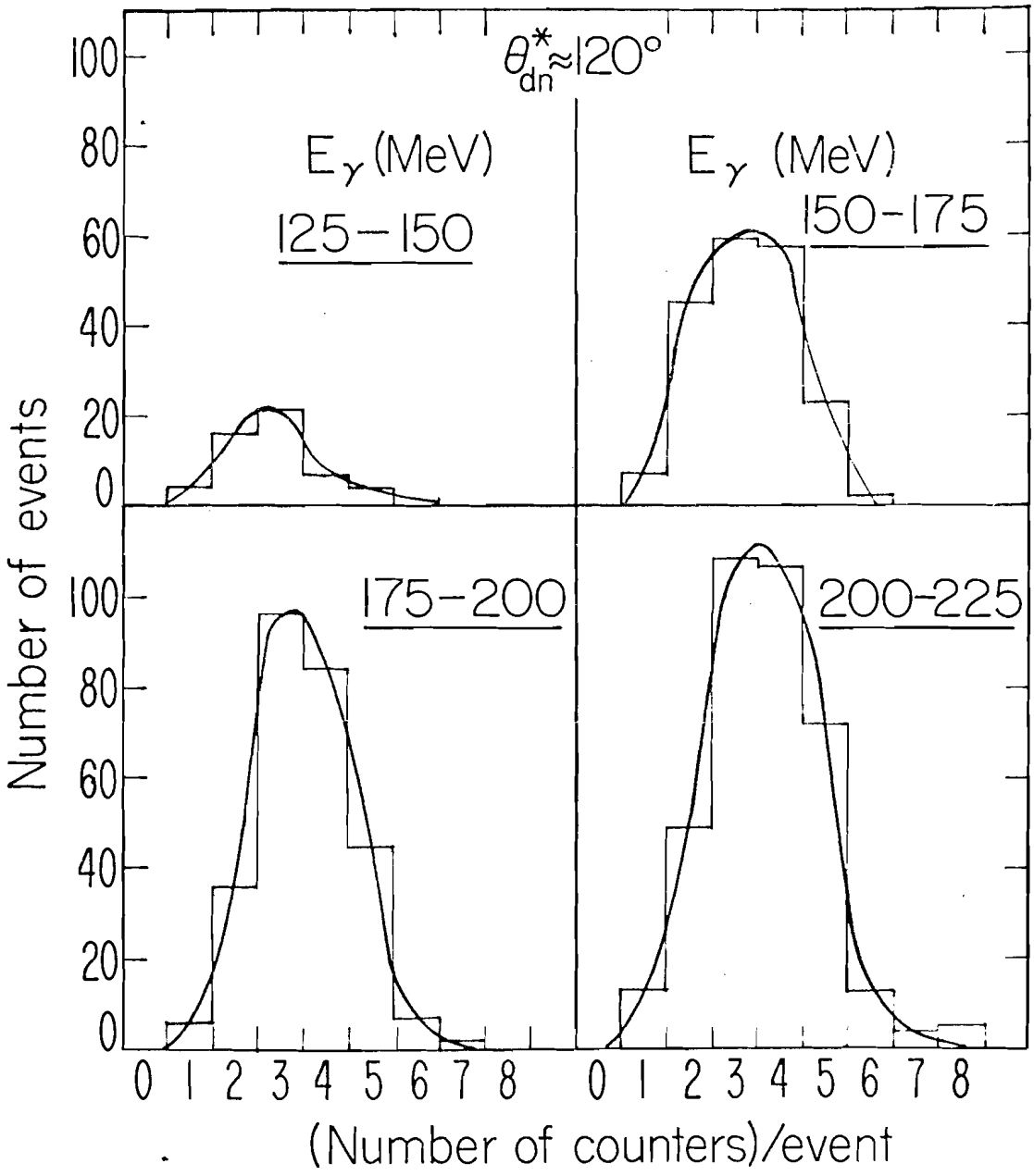

Figure 14. Distribution of the Number of γ-chamber Counters that Fired per Event

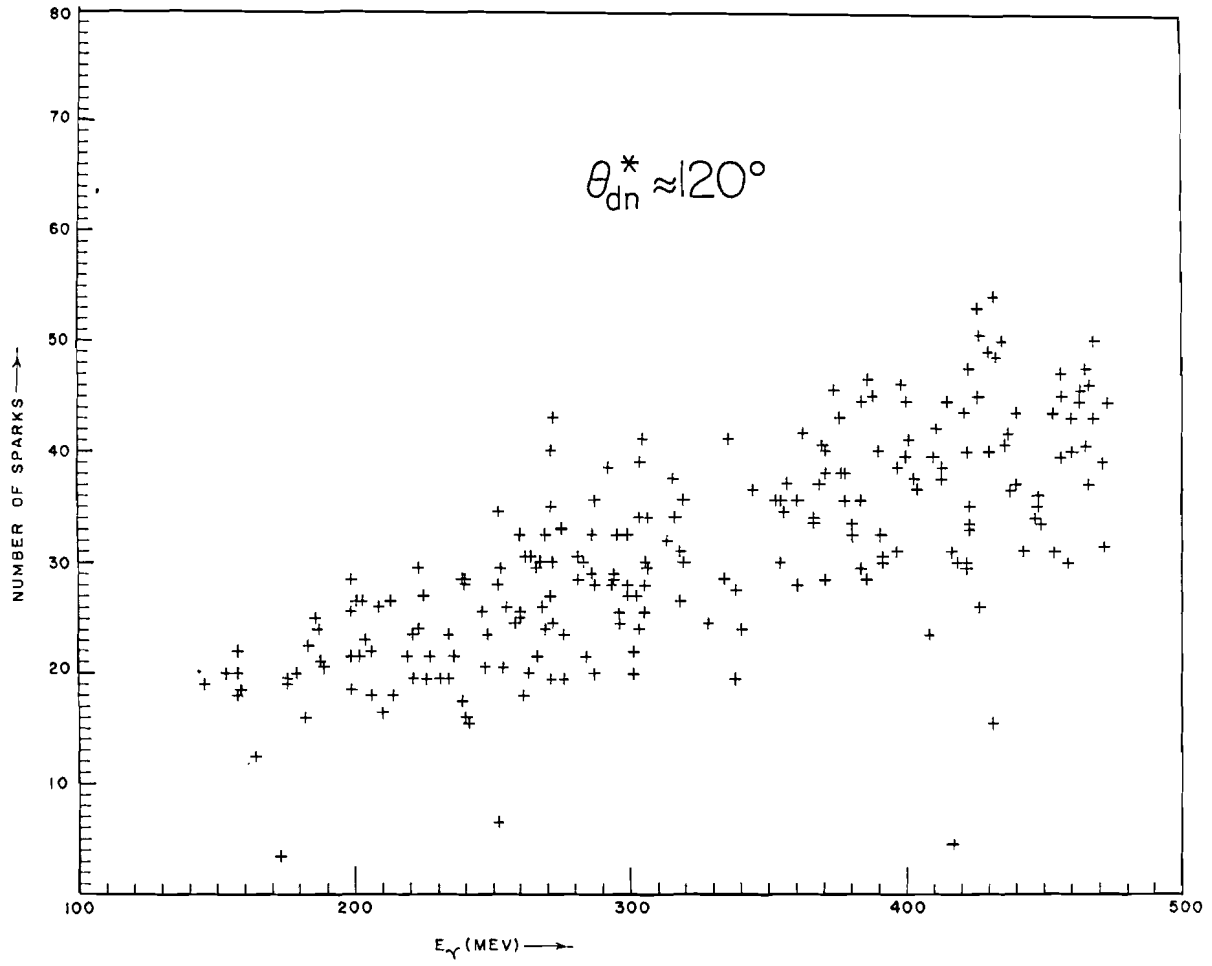

Figure 15. Scatter Plot of the Number of Sparks/Shower vs. the Shower Energy

indicates an average of 12 sparks per shower for photons with this energy. For showers with 12 sparks, a study was made of the spark distribution relative to the counter planes. In particular, it was determined whether or not, for each shower, there was at least one counter plane with sparks in each of the adjacent gaps which bracketed the counter. For a sample of 400 events, (97±5)% of the events had a counter bracketed by sparks and thus this study was consistent with an efficiency of 100%.

The third factor in the overall efficiency of the γ-chamber system, the operational efficiency of the automatic measuring system (Section III-B-1) and the computer programs (Section III-B-2), was checked by measuring, with a completely independent system, the film for 1000 randomly selected events from each of the five experimental configurations. Human scanners located the vertex for each event and then used an automatic measuring device to record the coordinates of the vertex. The coordinates were then compared to the corresponding coordinates found by the system described in Sections III-B-1 and III-B-2. The coordinates agreed, within the desired precision, for (98±3)% of the events. The events for which the coordinates disagreed were usually events with a poorly-defined vertex, e.g., events (accidentals) with photons entering the side of the γ-chamber. However, it could not be definitely determined that all such events originated from

reactions other than $n+p \rightarrow \gamma+d$, and the 98% figure was accepted as the general operational efficiency of the vertex-location procedure. The important point is that the efficiency did not appear to be a function of the photon energy and was reasonably constant for the five configurations of the apparatus.

In summary, the overall efficiency of the γ-chamber was assumed to be $\simeq$ 98% for photons from the reaction $n+p \rightarrow \gamma+d$ in the energy range 100 to 500 MeV. The 2% inefficiency did not appear to be a function of the photon energy but rather was a result of operational inefficiencies in the scanning system and computer programs. Consequently, no correction for the γ-chamber efficiency was made to the angular distributions.

C. WIRE-CHAMBER SPECTROMETER DATA

1. Spark Location

The first step in processing the spectrometer data was the conversion of the scaler values from the wire chambers into points in the chambers through which the charged particle had passed. This conversion was accomplished in an efficient manner by a CDC 6600 computer program, DEUTARM, developed with the aid of LRL programmers[49]. Each chamber had four wire planes and a possibility of zero, one, or two scaler values representing actual sparks from

each plane. For each plane, the scaler value could be interpreted as specifying which wire in the plane had carried current and this wire could be representated by the equation for a straight line

$$Ax + By = C \tag{1}$$

where A and B are direction cosines determined from the orientation of the fiducial wires on the plane and C is calculated from the scaler value and interfiducial distance. If it is now assumed that all the wire grids in the chamber lie in a common plane and that one wire fired in each grid, there result the four equations

$$A_i x + B_i y = C_i \quad , \; i=1,4 \tag{2}$$

representing the event in each chamber. These equations can be written in matrix notation as

$$\tilde{M}\tilde{W} = \tilde{C} \tag{3}$$

$$\text{where } \tilde{M} = \begin{pmatrix} A_1 & B_1 \\ A_2 & B_2 \\ A_3 & B_3 \\ A_4 & B_4 \end{pmatrix} , \quad \tilde{W} = \begin{pmatrix} x \\ y \end{pmatrix} , \text{ and } \tilde{C} = \begin{pmatrix} C_1 \\ C_2 \\ C_3 \\ C_4 \end{pmatrix} .$$

In general, equation 3 is overdetermined and does not have a unique solution for $\tilde{W}$ (the four lines do not intersect in a common point). However, equation 3 can be rewritten

$$\tilde{M}\tilde{W} - \tilde{C} = \tilde{R} \quad , \text{ where } \quad \tilde{R} = \begin{pmatrix} R_1 \\ R_2 \\ R_3 \\ R_4 \end{pmatrix} \tag{4}$$

and there does exist a unique solution of equation 4 which minimizes $|R|^2$, the sum of the squares of the residuals, R_i. The solution is given by

$$\tilde{W} = \tilde{M}^I \tilde{C} \tag{5}$$

where $\tilde{M}^I$ is the generalized inverse of $\tilde{M}$ and can be calculated with an algorithm developed and discussed in reference 50. The residuals, R_i, turn out to be the perpendicular distances from the point $\tilde{W}$ to each of the wires used in the calculation and thus serve as a criteria for determining whether or not a particular wire is to be associated with the point.

For each chamber the program DEUTARM calculated $\tilde{W}$ for all possible four-wire combinations and chose the combination with the smallest value of $|R|^2$, provided that each R_i for the combination was less than 0.5 inches. The four wires chosen were flagged as used and the program proceeded to search for any further points in the chamber. If no acceptable four-wire combination could be found, the program searched for three-wire combinations in a manner analogous to the four-wire search. If no four-wire or

three-wire points could be located, the program would also accept two-wire points. However, the number of events with two-wire points was small and these events were usually rejected for other reasons, e.g., no other chambers had points.

If all particles had been perpendicularly incident on the chambers, the points calculated in the manner described above would have been as accurate as possible. In order to improve accuracy for particles passing obliquely through the chambers a correction was made to the calculated points as follows. The two chambers on each side of the magnet were considered as a pair and a straight line was drawn connecting the calculated points in each chamber. This line was then adjusted by minimizing the sum of the squares of the perpendicular distances from the line to each wire used in determining the two points. The intersections of the adjusted line with the midplanes of the two chambers were then considered to be the best determination of the points on the particle's trajectory, provided that the fiducial wires on each plane had been positioned accurately and that the location of each chamber was well known. To ensure that such was the case, two additional checks were made.

The positional accuracy of the fiducial wires was checked by calculating the average values of the residuals, R_i, for each wire plane for particles which were

perpendicularly incident (within 0.5 degrees) on the chambers. The average values, for a large number of events, would have been zero if all fiducials had been accurately located. Small corrections (<0.75 mm) were made to several fiducials as a result of this check.

The surveyed positions of the chambers themselves were checked by turning off the current to the analyzing magnet and allowing particles to pass in a straight line through all four chambers. The resulting points (spark locations in the chambers) were fit to a straight line and corrections (<1.0 mm) were made on this basis for each configuration of the apparatus. The small magnitude of these corrections not only indicated that the chambers were properly surveyed but also that adverse effects from the fringing field of the cyclotron and from the clearing field in the chambers (see Section II-B-4-b) were negligible.

2. Momentum Calculation

After determining the spark locations in each chamber, the program DEUTARM next calculated the momentum of the charged particle. Since three points on the particle's trajectory (and knowledge of the magnetic field) are required for the calculation, the program determined the momentum only if at least three of the four chambers had one or more points each. For most events, all four chambers had at least one point and for these cases the

points in chambers S_2, S_3, and S_4 (see Fig. 2) were used in the momentum calculation. By not using the point in chamber S_1, the detrimental effect of the particle's Coulomb scattering in counter D_1 was eliminated. The calculation was also carried out for events with only three points but a larger uncertainty was assigned to the resultant momentum if chamber S_1 had to be used in the calculation.

The first step in calculating the momentum, P, consisted of approximating its value by the formula

$$P_1 = \frac{2k}{\sin \phi_o - \sin \phi_1} \quad . \tag{6}$$

The spherical angles, ϕ_o and ϕ_1, were defined by the entrance and exit rays to the magnet (see Fig. 16). For a particle of charge q traversing a rectangular magnetic field of length L and uniform strength B, the parameter k appearing in equation 6 would be

$$k = qBL \tag{7}$$

and P_1 as determined from equation 6 would be exact. In order to correct for the non-uniform field resulting from the C-magnet used in this experiment, k was calculated as a polynomial with 81 coefficients and four parameters as follows:

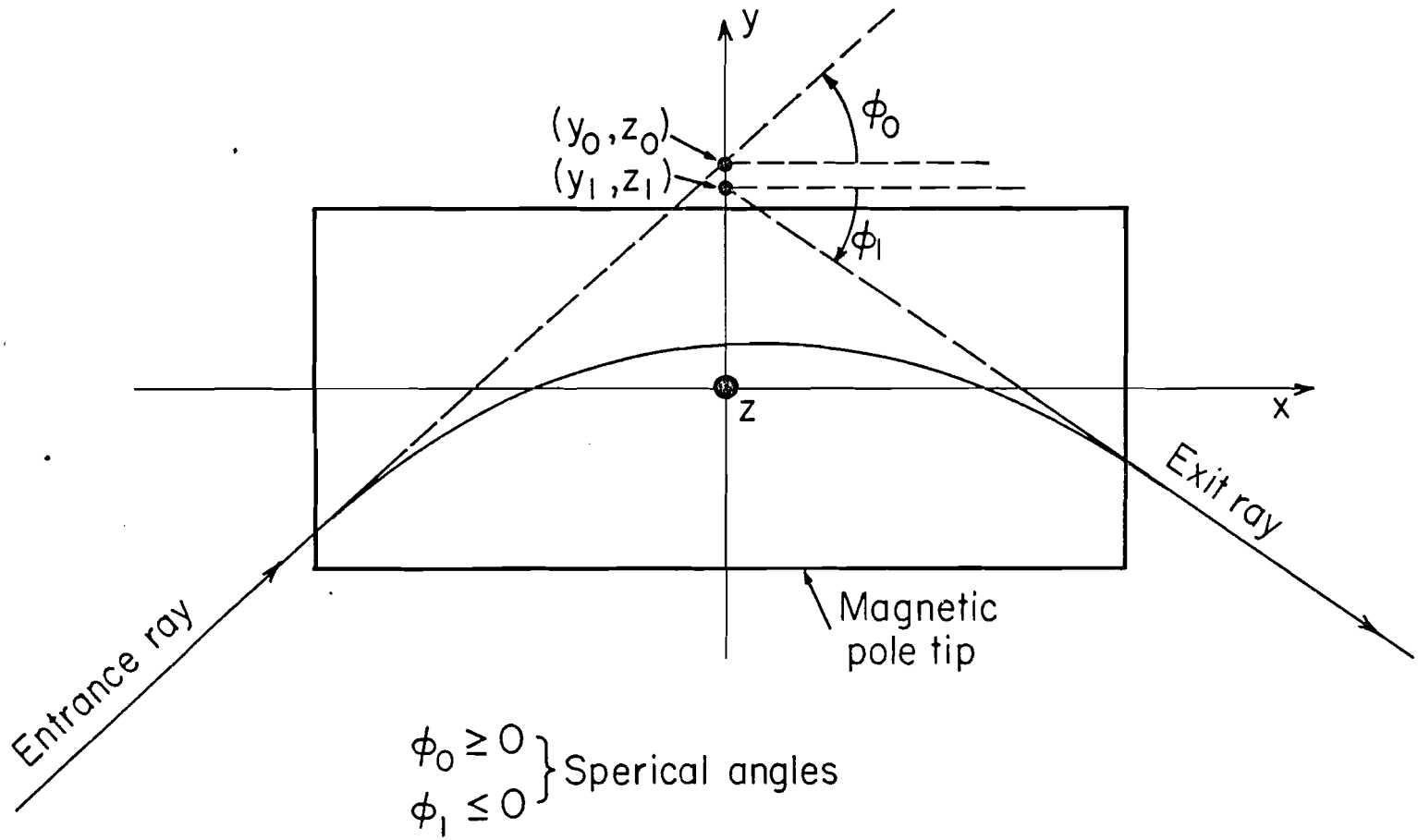

Figure 16. Analyzing Magnet Coordinate System

$$k = \sum_{i=0}^{2} \sum_{j=0}^{2} \sum_{k=0}^{2} \sum_{m=0}^{2} a_{ijkm}(\phi_o+\phi_1)^i y_1^j |z_1|^k (\phi_o-\phi_1)^m \qquad (8)$$

All parameters in equation 8 except the coefficients a_{ijkm} are defined in Fig. 16. The coefficients a_{ijkm} were calculated for each configuration of the apparatus by a simple Monte Carlo program which generated several hundred orbits of known momentum P and utilized equations 6 and 8 to find the coefficients a_{ijkm} which minimized the total RMS error.

With the momentum P_1 calculated from equation 6, an orbit was now integrated through the magnetic field starting from the ray defined by chambers S_3 and S_4. At each step in the integration process, the vertical component of the magnetic field, B_z, was calculated from the measured lattice of 5151 field values by a 16-point Lagrangian interpolation in three planes. The interpolation also yielded the derivatives dB_z/dx and dB_z/dy which, along with Maxwell's equations, were used to compute the remaining components of the field, B_x and B_y. The orbit was then adjusted accordingly and this process was repeated until the particle had left the field region. The orbit was then extrapolated, in a straight line, to chamber S_2 and the intersection of the orbit with the midplane of this chamber was calculated. If the intersection point was within 0.5 mm of the spark location in the chamber, P_1 was

within 0.2% of the correct momentum and was accepted as the momentum of the charged particle. If not, a further calculation was necessary.

To further correct the momentum, the intersection point of the integrated orbit with chamber S_2 was used to calculate new values of the parameters ϕ_0 and ϕ_1. A new value of k then resulted from equation 6 using P_1 and the new values of ϕ_0 and ϕ_1. The second approximation to the momentum, P_2, was then calculated from equation 6 with the new value of k and the original values of ϕ_0 and ϕ_1. The value P_2 was now used in another integration through the field and the intersection with chamber S_2 checked as before. For almost all events, no more than two integrations were necessary to obtain the desired accuracy. For those few events in which more integrations were necessary, an interpolation procedure was employed utilizing all previous intersection points and momentum guesses.

Although the momentum calculation procedure has been described using only chambers S_2, S_3, and S_4, the same procedure was easily modified to handle any three chambers if either S_2, S_3, or S_4 was missing from the event. However, if all four chambers did have sparks, a further check was possible. The last integrated orbit for each event was extrapolated to chamber S_1 and its intersection with this chamber was compared to the actual spark location for the chamber. A large difference in location indicated that the

charged particle had experienced large angle nuclear scattering in the spectrometer and the event was rejected. Furthermore, the distribution of the coordinate differences in chamber S_1 for a large number of events provided further information on the positional accuracy of the chambers.

In summary, the program DEUTARM calculated the momentum corresponding to all possible combinations of points for each event and recorded the momentum as well as the points used in the calculation. The uncertainty in the value of the momentum was approximately 1% for all momenta in the range 600 to 1500 MeV/c and was due primarily to the Coulomb scattering of the deuteron.

3. Mass Calculation

As mentioned previously, all background reactions except $n+p \rightarrow \pi^0+d$ could be eliminated if the mass of the charged particle in the spectrometer were known. To determine the mass, the time of flight of the particle from counter D_1 to counter D_2 was measured. The wire chamber information was used to determine where the particle had passed through the counters and thus the total flight path was known. Also, small corrections ($\approx$2 nanoseconds) were made to the time of flight depending on where the particle had hit the counter. Thus the velocity of the particle, v, was determined and its mass m, in MeV, could be calculated

from the formula

$$m = p \sqrt{(1/\beta^2) - 1} \tag{9}$$

where p is the momentum of the particle in MeV/c and β is the velocity of the particle, v, divided by the speed of light. The uncertainty in m is due primarily to the uncertainty in the time of flight measurement and consequently is a function of the momentum of the particle. Thus a momentum dependent mass cut was made in order to reject particles which were not deuterons. Figure 17 is a mass plot for high and low momentum particles and illustrates how strongly the uncertainty in the mass determination depends on the momentum. No deuterons were lost due to the mass cut and less than 0.2% of the particles accepted as deuterons were actually other particles.

4. Energy Loss Correction

The calculation described in Section III-C-2 resulted in the momentum of the deuteron at the effective center of the spectrometer whereas the momentum required by the kinematic fitting program was the momentum of the deuteron at the interaction point in the LH_2 target. Energy loss tables[51] were used to find an expression with which the energy loss of the deuteron in all the material through which it passed could be calculated. The energy loss, a function of the deuteron's momentum, is plotted as the

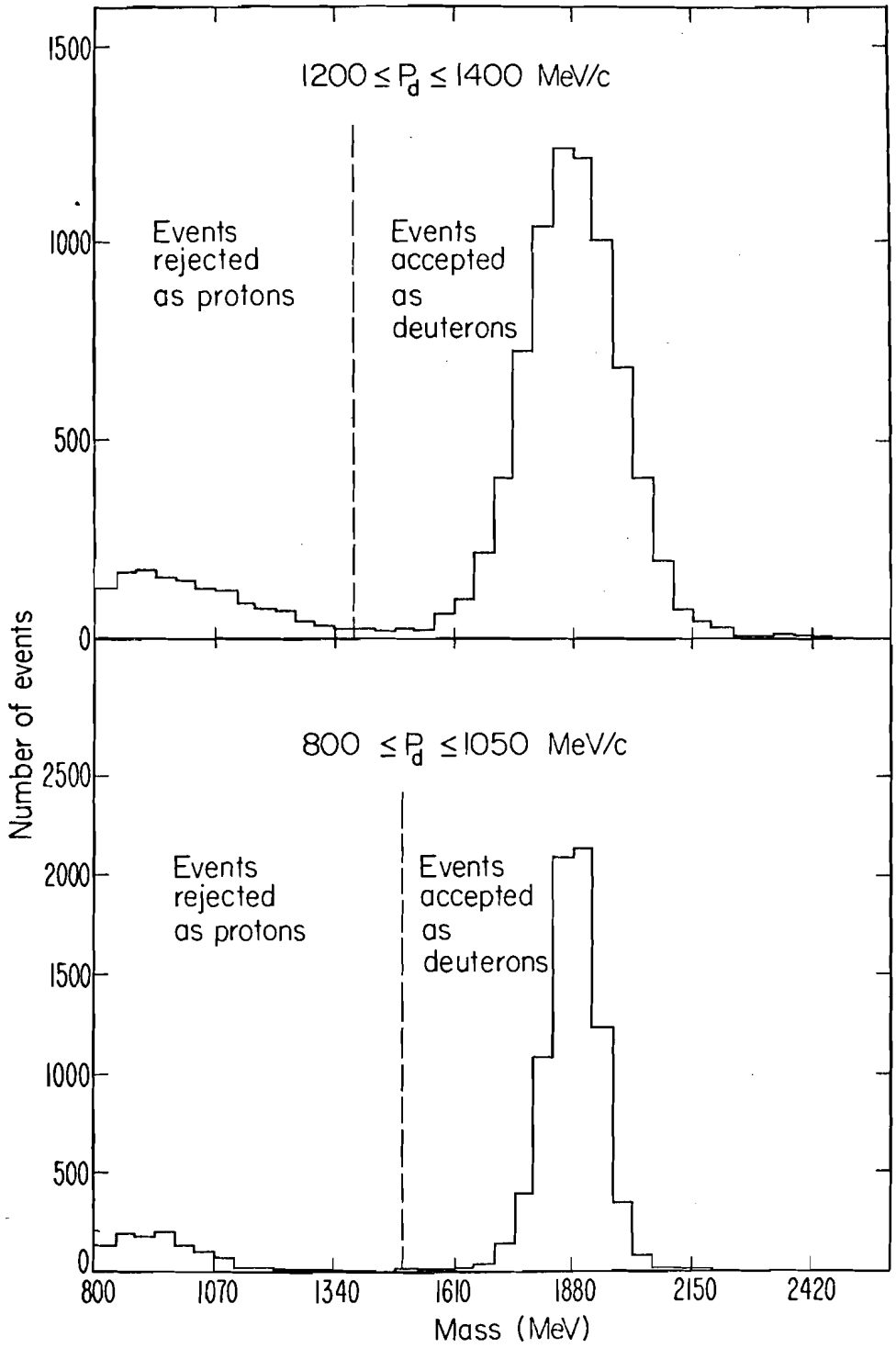

Figure 17. Charged Particle Mass Calculated From the Particle's Momentum and Time of Flight

solid line in Fig. 18. The uncertainty in the energy loss, the dashed curve in Fig. 18, is due to the uncertainty in determining the interaction point in the LH_2 target.

5. Spectrometer Efficiency

Although the percentage of events rejected on the basis (or lack) of spectrometer data varied from 15% to 30% for the various configurations of the apparatus, the results relating to the overall efficiency of the spectrometer were the same in each case. Table 3 is a summary of the events rejected for a typical configuration of the apparatus.

TABLE 3

REJECTED EVENTS

	Number of Events	% of Total
Total number of events	83,403	100.0
Rejected as protons	9,156	11.0
Lacking wire chambers	154	0.2
No momentum calculated	4,494	5.4
Inconsistent orbit	1,153	1.4
Outside LH_2 target	1,583	1.9
No deuteron angle	70	0.1
Total number rejected	16,610	20.0

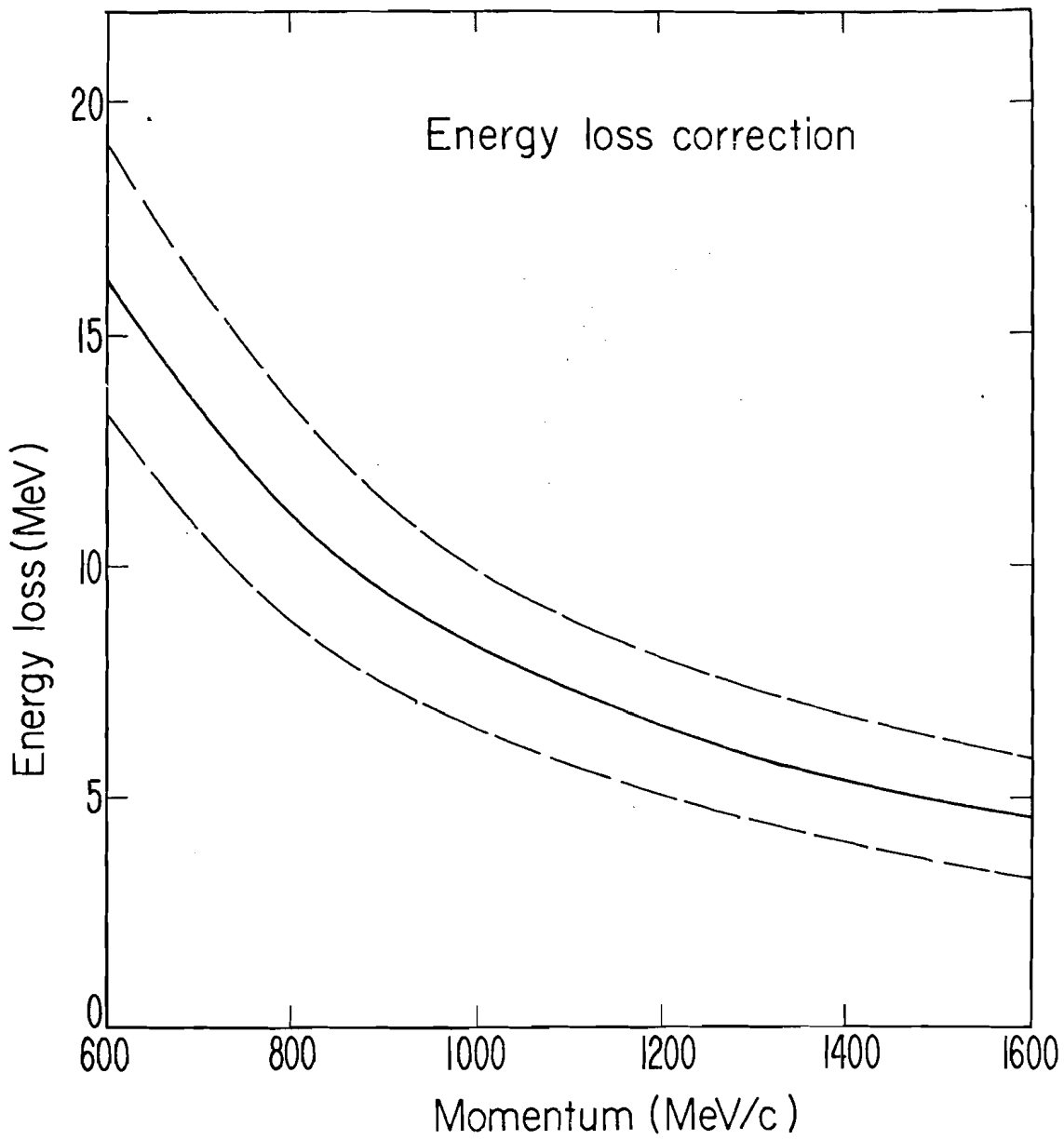

Figure 18. Energy Loss Correction for Charged Particles

The percentage of events rejected as protons ranged from 10% to 25% for the various configurations of the apparatus and constituted the largest category of rejects in all cases. However, as noted in section III-C-3, no deuterons were lost in the mass cut and only a small percentage (<0.2%) of the lower mass particles were misclassified as deuterons. Furthermore, at least 90% of the misclassified particles failed to satisfy the constraints applied by the kinematic fitting program (to be discussed in Section III-D) and thus this category of rejects had a completely negligible effect on the angular distribution.

The category "lacking wire chambers" consisted of those events in which two or more chambers had no sparks. Although 0.2% of the events were rejected for this reason, the effect on the angular distribution was at most 0.1% since the percentage rejected was practically constant from angle to angle.

A rather large number of events (≈5.4%) were rejected because no momentum could be calculated even though sufficient wire chamber information (sparks in three or more chambers) was available. The momentum could not be calculated whenever an orbit being integrated through the magnetic field by the analysis routine "collided" with the pole tips or the yoke of the magnet. Elaborate programming precautions were taken to ensure that the collisions were "real" rather than being caused by a bad first approxi-

mation to the momentum. In addition, 100 of these orbits were plotted by hand and 95% were definitely scatters off the pole tips or yoke and the remaining 5% were of doubtful quality. Thus the uncertainty introduced into the angular distribution by this type of event was at most 0.25%.

Events in the category "inconsistent orbit" were those events which had experienced large angle nuclear scattering in the spectrometer as indicated in chamber S_1 by a large difference between the location of the actual spark and that predicted by the integration routine (see Section III-C-2). The problem of losing events due to nuclear scattering was actually more serious than indicated by the 1.4% figure listed in Table 3, and the resulting correction to the angular distribution is discussed in detail in Section III-H-1. The problem was more serious than indicated because the 1.4% figure includes only those events which had scattering angles in the approximate range two to five degrees. Particles scattering less than two degrees were not rejected by the computer program and those scattering through an angle larger than five degrees missed the chamber completely.

Events in the next category, "outside LH_2 target", resulted from a fiducial volume cut made by extrapolating the deuteron ray from chambers S_1 and S_2 to the midplane of the LH_2 target and determining whether or not the ray had originated outside the hydrogen flask. Particles in this

category resulted either from neutrons interacting in the mylar walls of the vacuum vessel surrounding the flask or from events which had experienced a nuclear scatter before reaching chamber S_2. Except for the correction to be discussed in Section III-H-1, this cut did not affect the spectrometer efficiency or the shape of the angular distribution.

The last category, "no deuteron angle" consisted of those events in which chamber S_1 or S_2 had no spark. The deuteron scattering angle could not then be calculated with sufficient accuracy and the event was lost. Although this effect ranged from 0.1% to 0.3% for the various configurations, the actual chamber inefficiency was estimated to vary by only 0.1% since it was discovered that at least 50% of these events were caused by neutrons interacting in the lucite frame of chamber S_1.

In summary, although the number of events rejected on the basis of the spectrometer data was as high as 30%, the efficiency of the spectrometer for detecting deuterons from the reaction $n+p \rightarrow \gamma+d$ which entered the spectrometer system was greater than 99%. Furthermore, since most of the inefficiencies were not angle dependent, the uncertainty introduced into the angular distribution was less than 0.5%. This estimate of the uncertainty due to the spectrometer system does not include the nuclear scattering of the deuteron which is calculated in Section III-H-1.

D. LEAST-SQUARES KINEMATIC FITTING

The processed data from the spectrometer and the gamma chamber were merged by a CDC 6600 program, JANE, which transformed the data from each event to a common coordinate system and then fit the data to the hypothesis that the event was an $n+p \rightarrow \gamma+d$ reaction. In addition to calculating a "goodness" number (χ^2-value) for the event, the program calculated two unmeasured kinematic parameters, the energy of the incident neutron and that of the final state photon. The final data resulting from the program were written into the photodigital storage system at LRL and were readily available for various binning and histogramming routines.

The data from each event were transformed to a coordinate system whose origin was determined by the intersection of the deuteron ray with the midplane of the LH_2 target. The coordinate system was oriented as pictured in Fig. 19, and the spherical angles describing the photon and deuteron trajectories were calculated in this system. Spherical angles describing the direction of the incident neutron were found by drawing a line from the center of the beryllium target in the cyclotron to the origin of the coordinate system. Thus the measured quantities for each event, parameterized in the coordinate system of Fig. 19, consisted of:

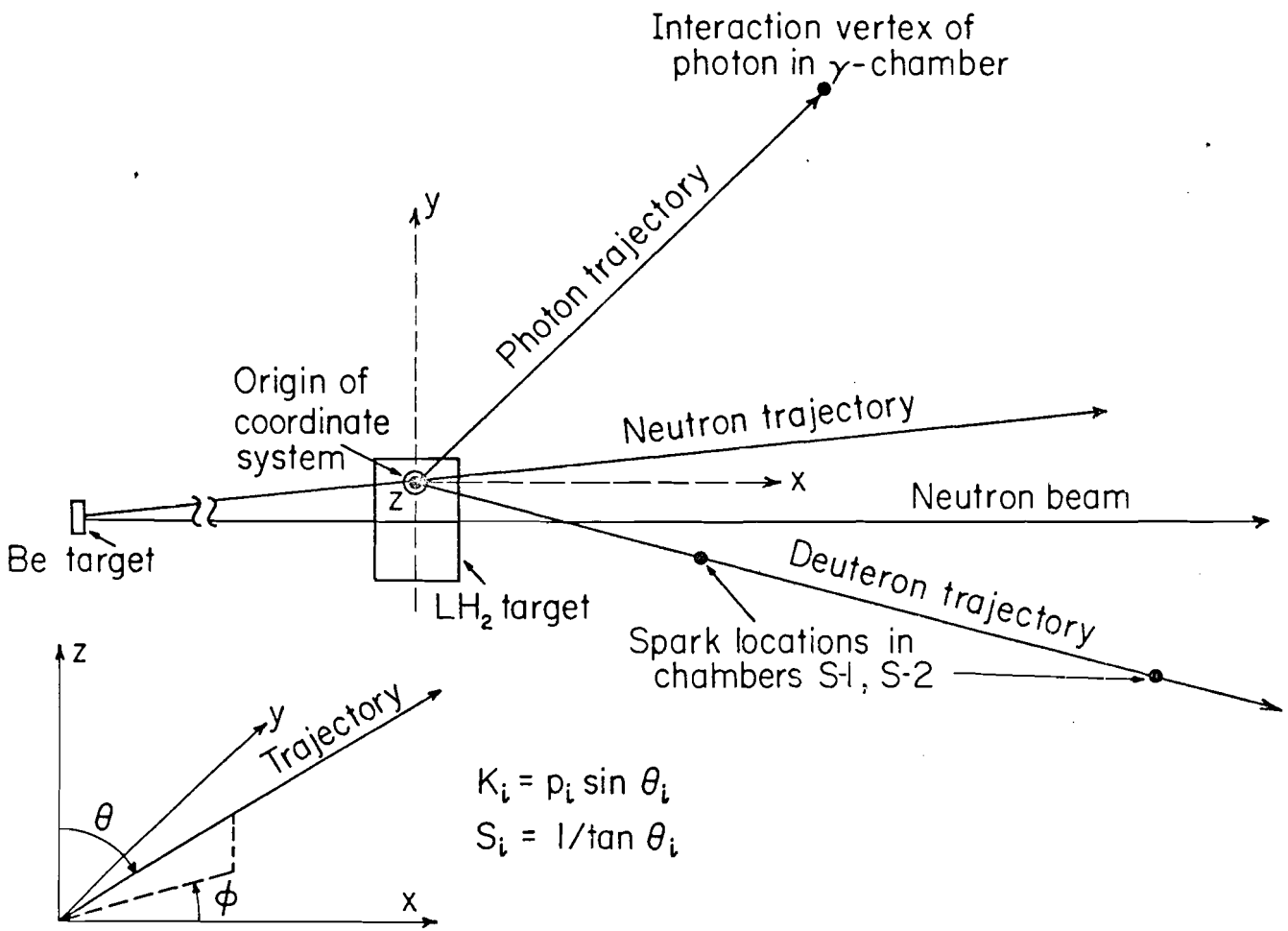

Figure 19. Coordinate System Used by the Kinematic Fitting Program

θ_n, ϕ_n = spherical angles of incident neutron

$\theta_\gamma, \phi_\gamma$ = spherical angles of photon

θ_d, ϕ_d = spherical angles of deuteron

P_d = calculated momentum of deuteron at interaction vertex

For an $n+p \rightarrow \gamma+d$ event, the measured quantities as expressed above are subject to the constraints of energy-momentum conservation. In order to express these constraints in a simple form, the following definitions are used:

$$k_i = p_i \sin \theta_i$$

$$s_i = 1/\tan \theta_i$$

where p_i is the momentum of the ith particle. The conservation of energy and momentum can then be expressed by the four equations

$$k_1 \cos\phi_1 - k_2 \cos\phi_2 - k_3 \cos\phi_3 = 0 \qquad (10a)$$

$$k_1 \sin\phi_1 - k_2 \sin\phi_2 - k_3 \sin\phi_3 = 0 \qquad (10b)$$

$$s_1 k_1 - s_2 k_2 - s_3 k_3 = 0 \qquad (10c)$$

$$E_1 + m_p - E_2 - E_3 = 0 \qquad (10d)$$

where m_p is the mass of the proton. The subscripts 1,2,3 refer to the incident neutron, the photon, and the deuteron,

respectively, and E_i is the total energy of the ith particle. The only two independent variables in equations 10(a-d) which are not measured are k_1 and k_2. Thus the four equations are overdetermined and a fitting procedure must be utilized to obtain the optimal solution.

Minimizing a chi-squared value subject to the non-linear constraints of momentum and energy conservation is a standard procedure for bubble chamber physicists[52]. The procedure is discussed in detail in reference 52 and only the general technique will be sketched below.

In general, the problem consists of having a set of n measured variables (x_i^m, i=1,...,n), estimates of the measurement errors (Δx_i^m), and a set of constraining equations

$$F_k(x_i) = 0 \qquad k=1,\ldots,c \quad . \tag{11}$$

The error matrix, taken to be diagonal for this experiment, is defined as

$$G_{ij}^{-1} = \overline{\Delta x_i^m \Delta x_j^m}\ \delta_{ij} \quad . \tag{12}$$

The quantity, χ^2, is then defined as

$$\chi^2 = \sum_{i,j=1}^{n} (x_i - x_i^m) G_{ij} (x_j - x_j^m) \tag{13}$$

and this quantity is to be minimized subject to the constraining equations 11. In order to minimize the χ^2-value

and simultaneously satisfy the equations of constraint, Lagrange multipliers, α_k, are introduced and we then want to minimize

$$M = \chi^2 + 2 \sum_{k=1}^{c} \alpha_k F_k(x_i) \tag{14}$$

with respect to x_i and α_k. The conditions for minimization are then

$$\frac{\partial M}{\partial x_i} = 2\{ \sum_{j=1}^{n} G_{ij}(x_j - x_j^m) + 2 \sum_{k=1}^{c} \alpha_k \frac{\partial F_k}{\partial x_i}\} = 0 \tag{15a}$$

and $$\frac{\partial M}{\partial \alpha_k} = 2F_k(x_i) = 0 \quad . \tag{15b}$$

The equations 15(a-b) must now be solved for x_i and α_k. If the constraining equations 11 were linear in the variables x_i, the solution would be trivial. However, since the F_k are non-linear in general, the following iterative process must be used.

Let the values of the variables on the μth iteration be x_i^μ and α_k^μ. One can then write:

$$B_{ik}^\mu = \left(\frac{\partial F_k}{\partial x_i}\right)\Bigg|_{x_i = x_i^\mu} \tag{16a}$$

$$H^{\mu}_{kw} = \sum_{s=1}^{n} \sum_{t=1}^{n} (\tilde{B})^{\mu}_{ks} \; G^{-1}_{st} \; B^{\mu}_{tw} \tag{16b}$$

where $\tilde{B} = B^{\text{transpose}}$

$$\alpha_k^{\mu+1} = \sum_{w=1}^{c} (H^{\mu})^{-1}_{kw} \; \{F^{\mu}_k + \sum_{j=1}^{n} (x^m_j - x^{\mu}_j) \; B^{\mu}_{jk}\} \tag{16c}$$

$$x_i^{\mu+1} = x_i^m - \sum_{k=1}^{c} \sum_{j=1}^{n} G^{-1}_{ij} \; B^{\mu}_{jk} \; \alpha_k^{\mu+1} \quad . \tag{16d}$$

The iteration begins with

$$x_i^o = x_i^m$$

and

$$\alpha_k^o = 0 \quad .$$

After every iteration the χ^2-value is calculated and the iterative process is halted when a minimum χ^2 is found. This minimum χ^2 is thus a measure, in a least-squares sense, of how well the measured variables x_i^m satisfy the hypothesis expressed by equations 11.

In order to apply the general procedure to the particular case of this experiment, equations 10a and 10b are solved for the unmeasured variables k_1 and k_2. The two equations, 10c and 10d, then remain as the constraining

equations analogous to the $F_k(x_i)$ in equations 11. For this reason, the fit for this particular case is classified as a 2-constraint (2C) fit.

Distributions of the χ^2-values for two of the angles measured in the experiment appear in Fig. 20. Figure 20a is an example of a case in which the background (primarily events from the reaction $n+p \rightarrow \pi^0+d$) does not simulate the $n+p \rightarrow \gamma+d$ reaction and thus is easily and accurately subtractable. In contrast, Fig. 20b indicates a case in which many background events simulate $n+p \rightarrow \gamma+d$ events. In this case the background must be subtracted with the aid of the Monte Carlo programs to be discussed in Section III-E.

In addition to calculating a χ^2-value for each event, the fitting program JANE calculated the energy of the incident neutron and that of the final state photon for each event from the values of k_1 and k_2 on the last iteration. Also, the fitted errors Δx_i for all the variables x_i were calculated after the last iteration and were recorded by the program.

In order to check the fitting programs, each event was also fit to the hypothesis that it was an event of the type $n+p \rightarrow \gamma+X$ where X represents a particle of unknown mass. One further constraining equation is lost in solving for the mass of the X particle and a 1-constraint fit results. If the fitting programs were operating properly,

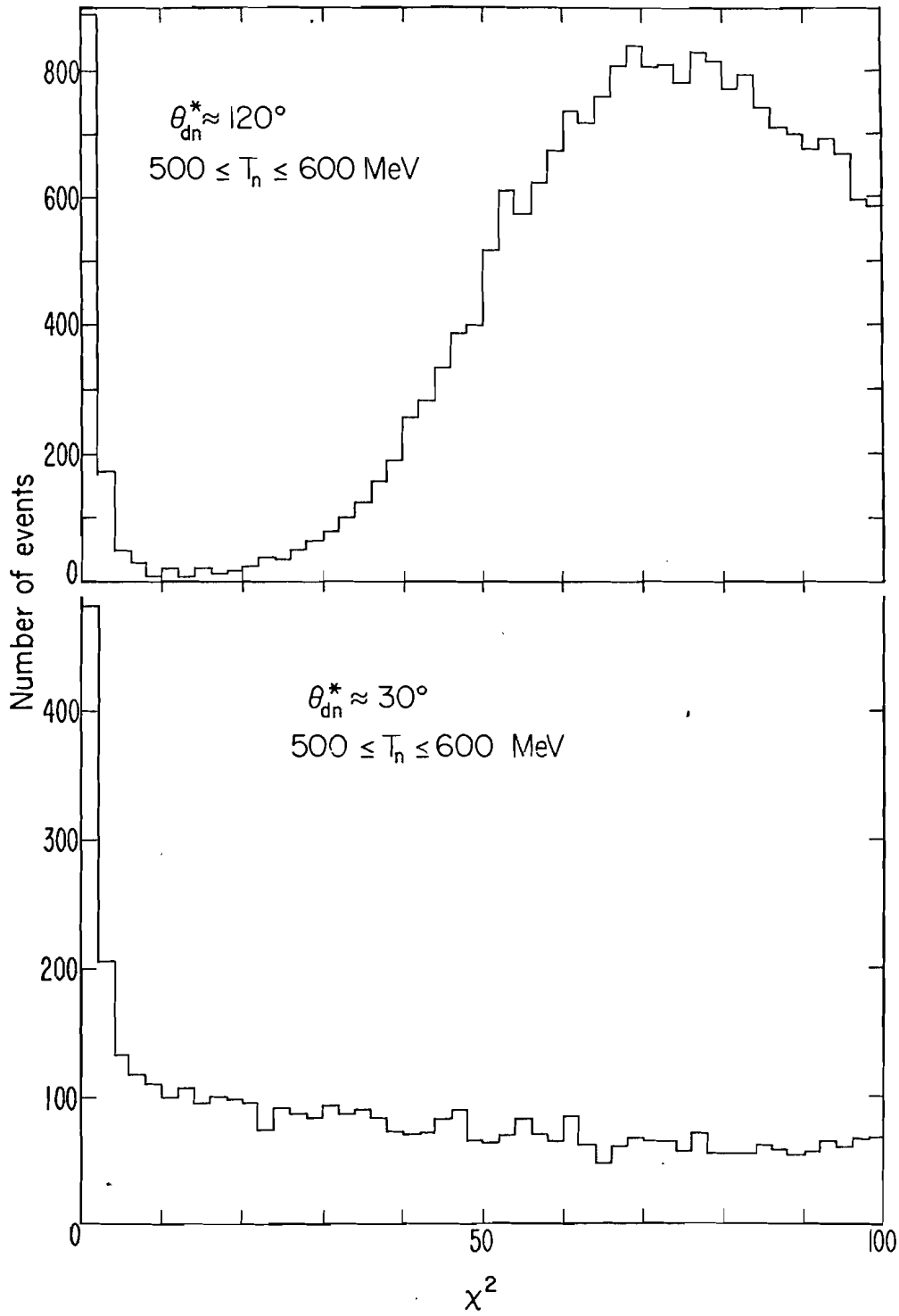

Figure 20. χ^2-plots from the Kinematic Fitting Program

a mass plot for the X particle should have a sharp peak at the mass of the deuteron resulting from $n+p \rightarrow \gamma+d$ events. Figure 21 indicates that such is indeed the case.

E. MONTE CARLO COMPUTER PROGRAMS

1. General Description

Monte Carlo computer programs were written for three explicit purposes: (1) to calculate the relative solid angle subtended by the apparatus, (2) to check the least-squares kinematic fitting programs, and (3) to aid in the background subtraction. In addition, the processing of the Monte Carlo generated data served as a general check of the entire data reduction scheme. A simulation of the $n+p \rightarrow \gamma+d$ reaction accomplished the first two tasks above and the third was accomplished by a simulation of the $n+p \rightarrow \pi^0+d$ reaction.

The simulation of both reactions was very similar, differing only in input cross sections and kinematic generation routines. The input to the programs consisted of: (1) specification of the apparatus for each experimental configuration, (2) position and size of the beryllium target in the cyclotron, (3) neutron energy spectrum, pictured in Fig. 4, (4) approximation of the geometric distribution of the neutron beam at the hydrogen target, displayed in Fig. 3, (5) total cross sections and angular

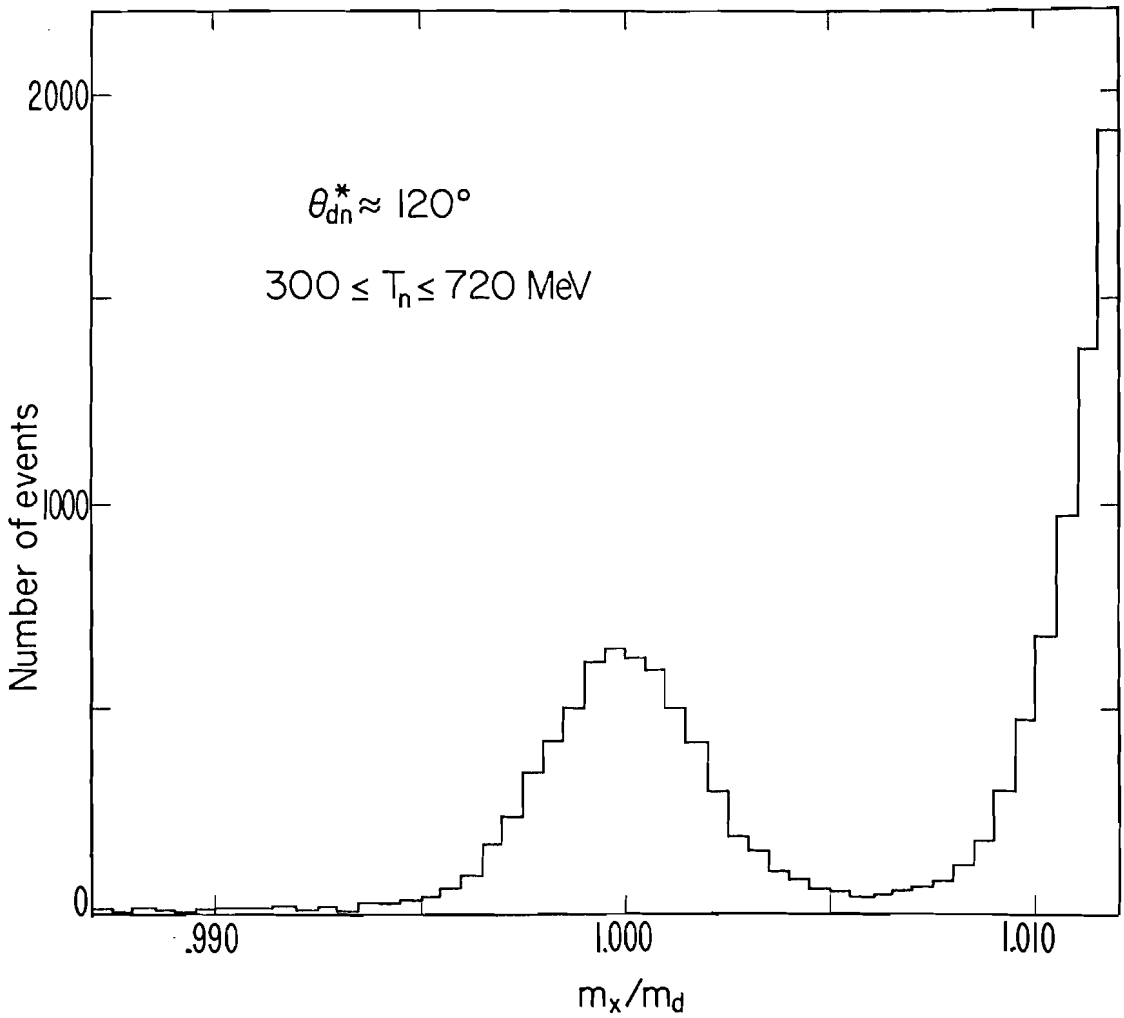

Figure 21. Missing Mass(m_x) Plot from the 1C Fit (m_d is the Deuteron Mass)

distributions for the respective reactions, and (6) kinematic routines to generate events and to translate from center of mass to laboratory coordinates. The data resulting from the Monte Carlo programs were processed by the same analysis routines used for the real data.

2. Solid Angle Calculation

The effective solid angle for each configuration of the apparatus was defined jointly by the gamma chamber counters and by the counters in the magnetic spectrometer. For this type of situation the effective solid angle is usually more easily determined by a Monte Carlo program than by a direct calculation.

The problem of calculating the solid angle for this experiment was somewhat simplified in that the angular distribution, not the differential cross section, was being measured. Calculation of the differential cross section was precluded by the fact that the absolute intensity of the neutron beam was not known. Consequently, rather than calculating the absolute value of the solid angle for each measured point, it was sufficient to calculate only the relative values. These "relative solid angles" were calculated in the following manner.

For each angle at which the angular distribution was measured, the configuration of the apparatus was specified in the Monte Carlo program exactly as it had been measured

for the collection of the real data. For every configuration, the same neutron spectrum, $F(T_n)$, and the same hypothetical center of mass differential cross section, $d\sigma/d\Omega(T_n,\theta)$, were used to generate $n+p \rightarrow \gamma+d$ events until a specified number of events had been generated. The events that were "detected" by the apparatus were then processed by the same analysis routines as used for the real data and all fiducial volume cuts were applied as for the real data. Events which survived the analysis routines and fiducial volume cuts were classified as the Monte Carlo yield, $Y(T_n)$, for that particular configuration. For the ith configuration, $Y^i(T_n)$ can also be calculated as

$$Y^i(T_n) = F(T_n) \frac{d\sigma}{d\Omega}(T_n,\theta) N_p J^i(T_n,\theta) \Delta\Omega^i_{lab} \qquad (17)$$

where

T_n	=	neutron kinetic energy
θ	=	center of mass scattering angle
N_p	=	number of protons/cm^2 in the LH_2 target
$J^i(T_n,\theta)$	=	Jacobian of the transformation from center of mass to laboratory coordinates
$\Delta\Omega^i_{lab}$	=	solid angle in laboratory system

In equation 17, $Y^i(T_n)$ is recorded from the Monte

Carlo, $F(T_n)$ and $d\sigma/d\Omega(T_n,\theta)$ have known values, and N_p is the same for all configurations. Thus the product, $J^i(T_n,\theta)\Delta\Omega^i_{lab}$, can be calculated and this value is the "relative solid angle" for the ith configuration. The justification for the preceding technique lies in the fact that $\Delta\Omega^i_{lab}$ was implicitly included in the Monte Carlo program by correctly specifying the placement of the apparatus. The Jacobian, $J^i(T_n,\theta)$, was also implicitly included by the kinematic routines which transformed, to the laboratory system, events generated in the center of mass system.

Numerous checks were made to ensure that the $n+p \rightarrow \gamma+d$ Monte Carlo simulation had been done correctly. Specifically, the inputs to the program, $F(T_n)$, $d\sigma/d\Omega(T_n,\theta)$ and the geometric distribution of the neutron beam, were varied within reasonable bounds to ensure that their variations did not alter the calculated relative solid angle. Also, the routines that traced the deuteron's trajectory through the magnet were checked in a variety of ways, including alteration of the step size used in the integration. In addition, distributions of events on the four wire chambers were compared for the real and Monte Carlo data. This comparison was facilitated by the fact that there existed kinematic regions in which background reactions were of a negligible magnitude (<1%). Distributions of real and Monte Carlo events on chambers S_2 and S_4

from one such background-free region are displayed in Fig. 22. The good agreement evident in Fig. 22, particularly between the distributions on chamber S_4, is typical of the checks which ensured that the Monte Carlo was indeed correct.

3. Kinematic Fitting Check

Monte Carlo generated events for the reaction $n+p \rightarrow \gamma+d$ were processed by the same kinematic fitting program used to process real events. The χ^2-value (equation 13) calculated by the fitting program is obviously sensitive to the estimates of the uncertainties, Δx_i^m, in the measured kinematic parameters, x_i^m. Thus a comparison of the χ^2-distributions for real and Monte Carlo events serves as a check that the experimental uncertainties, Δx_i^m, were estimated correctly in the Monte Carlo generating routine as well as in the kinematic fitting program. Figure 23 is such a comparison for several neutron energy intervals from a kinematic region relatively free of background events from the reaction $n+p \rightarrow \pi^o+d$ (see Fig. 20a). Monte Carlo events were also used: (1) to ensure that $n+p \rightarrow \gamma+d$ events were not being rejected by the fitting program (or being given abnormally high χ^2-values) and (2) to determine a χ^2-value, χ_b^2, such that all events with $\chi^2 > \chi_b^2$ could be considered as background or, equivalently, that all $n+p \rightarrow \gamma+d$ events had

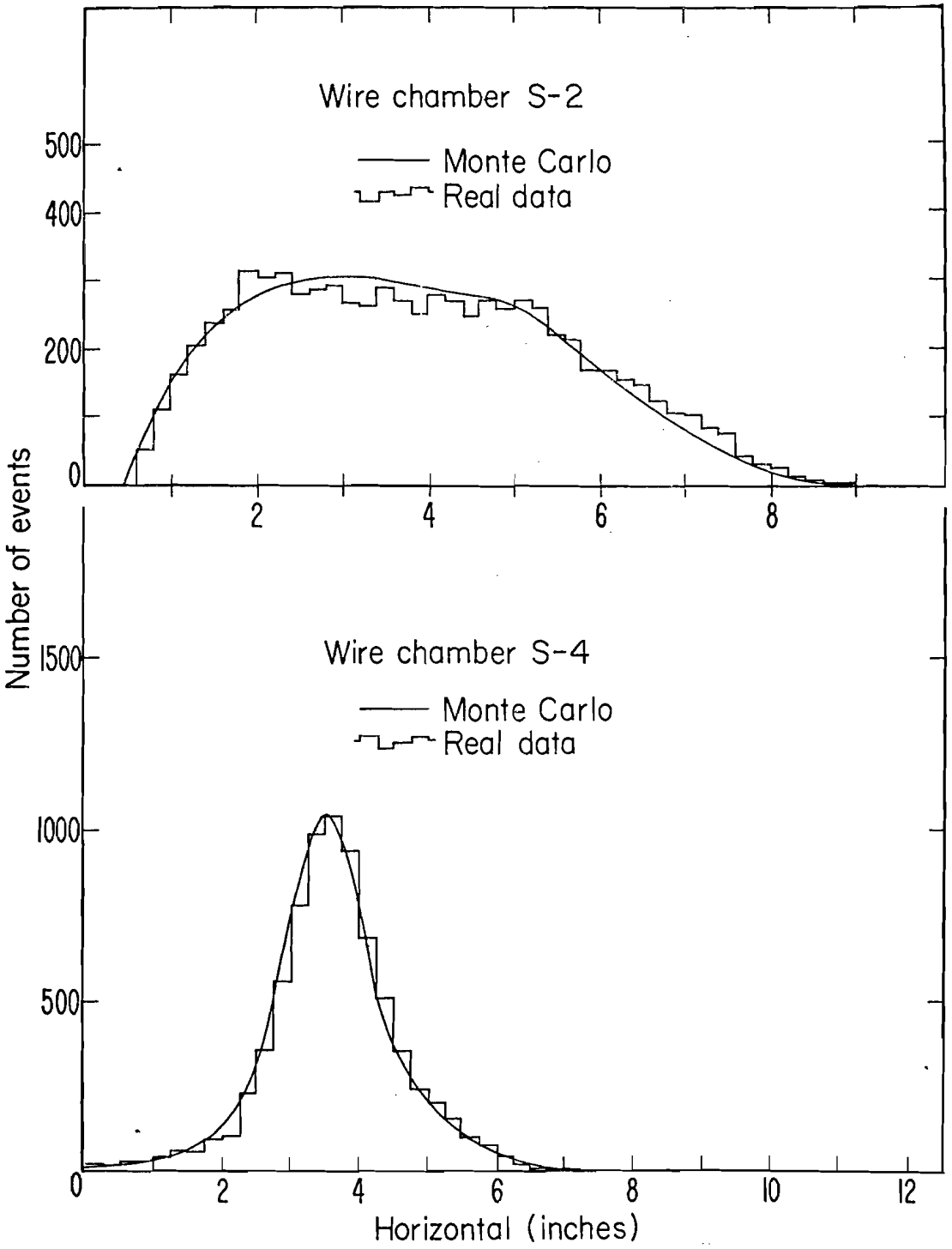

Figure 22. Distributions of Real and Monte Carlo $n+p \rightarrow \gamma+d$ Events on Wire Chambers S_2 and S_4

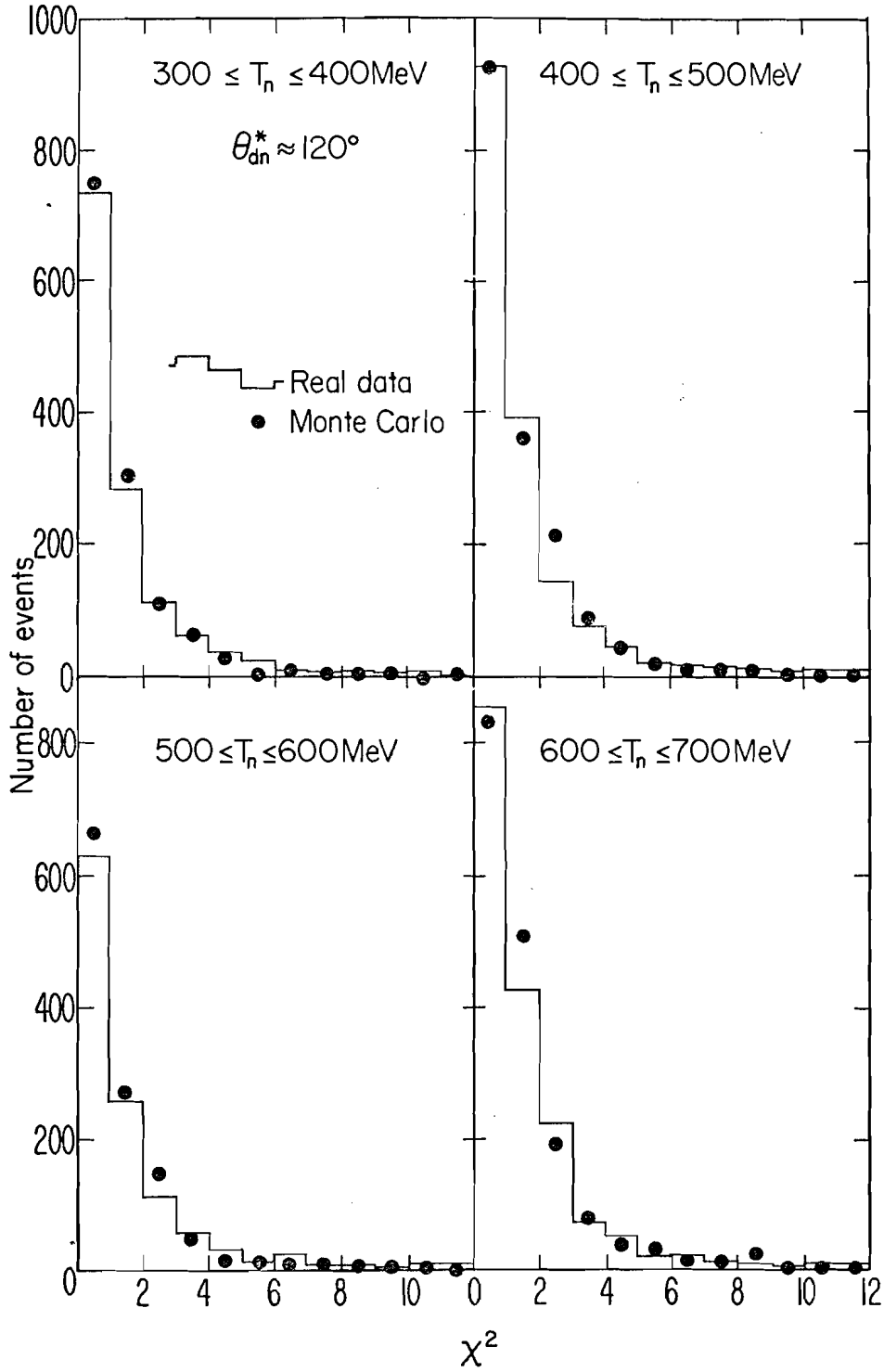

Figure 23. Comparisons of χ^2-plots for Real and Monte Carlo n+p → γ+d Events

a $\chi^2 < \chi_b^2$. In kinematic regions heavily contaminated with background (see Fig. 20b), a knowledge of χ_b^2 was a valuable aid in the background subtraction.

4. Background Subtraction Aid

The signal-to-noise ratio R_{sn}, where R_{sn} is the number of $n+p \rightarrow \gamma+d$ events divided by the number of $n+p \rightarrow \pi^o+d$ events with $\chi^2 < \chi_b^2$, ranged approximately from 100/1 to 1/1 depending on the scattering angle θ_{dn}^* and the neutron energy T_n. Of the five configurations of the apparatus (see Section II-C), the two with $\theta_{dn}^* \simeq 90^o$ and $\theta_{dn}^* \simeq 120^o$ had large R_{sn} ratios for all T_n intervals. For these two configurations, the background could be accurately subtracted without any aid from the $(\pi^o d)$ Monte Carlo. For the other three configurations, it was necessary to ascertain, using the $(\pi^o d)$ Monte Carlo, the general shape of the χ^2-distributions from $(\pi^o d)$ events in the region $\chi^2 < \chi_b^2$.

Since the total cross section and angular distribution for the reaction $n+p \rightarrow \pi^o+d$ are well known[53], the construction of the $(\pi^o d)$ Monte Carlo program was a rather straightforward task. The only complicating feature was the fact that the efficiencies of the anti-counters around the LH_2 target (A_3, A_4 and A_5 in Fig. 2) were not precisely known. Consequently, rather than using the Monte Carlo data to reconstruct the χ^2-distributions from real events with great precision, it was considered more important to

ensure that no conceivable efficiency of the anti-counters could cause an unexpected peaking or depression in the χ^2-distributions in the region $\chi^2 < \chi_b^2$. Thus the $(\pi^o d)$ Monte Carlo data was used only to ensure that polynomials which fit the data in the region $\chi^2 > \chi_b^2$ could be smoothly extrapolated to the region $\chi^2 < \chi_b^2$.

Figure 24 is a comparison between the real data and smooth curves hand drawn through the $(\pi^o d)$ Monte Carlo data for $\theta_{dn}^* \simeq 30^o$ and for four T_n intervals. This scattering angle had the worst background contamination and thus represents the most severe test of the $(\pi^o d)$ Monte Carlo. The figure illustrates two important points. First, the $n+p \rightarrow \gamma+d$ Monte Carlo indicated that ≈99.9% of all (γd) events have a $\chi^2 < 10$ and thus lie in the first bin of the histogram of the real data. Consequently, since $(\pi^o d)$ events have χ^2-values ranging from 0.0 to at least 500., the $(\pi^o d)$ data could be fit over a wide range of values and could then be extrapolated to the comparatively narrow range, 0.0 to 10., with considerable confidence. Secondly, although the curves representing the $(\pi^o d)$ Monte Carlo data do not fit the real data precisely for all four T_n intervals, they do, in each case, smoothly extrapolate to the χ^2-region from 0.0 to 10.

F. BACKGROUND SUBTRACTION

The general procedure for determining the number of

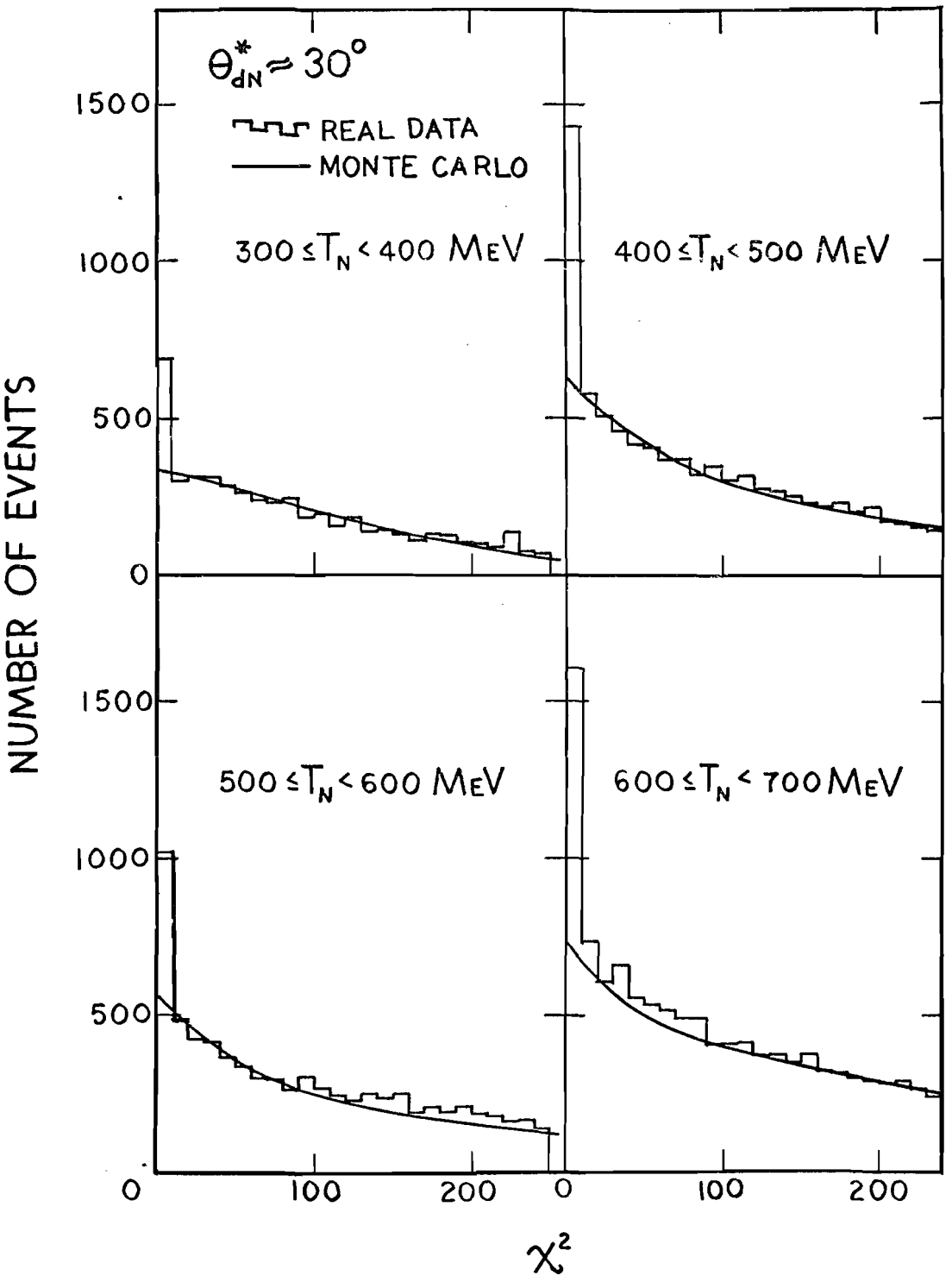

Figure 24. Comparison of χ^2-plots for Real Data and for Monte Carlo $n+p \rightarrow \pi^0+d$ Data

(γd) events in each energy-angle bin consisted of first counting the total number of events with $\chi^2 < \chi_b^2$ in the χ^2-plot for each bin and then subtracting the number of events considered to be background. As already pointed out, the Monte Carlo programs were used only to determine the value of χ_b^2 for each bin and to ensure that the (π^od) background could be smoothly extrapolated under the (γd) peak.

The χ^2-plots for all 20 energy-angle bins appear in Fig. 25(a-e). For each plot, the neutron energy interval ΔT_n and the average c.m. scattering angle of the deuteron relative to the neutron $\overline{\theta^*_{dn}}$ are indicated. The dashed line indicates the approximate value of χ_b^2 such that all events with $\chi^2 > \chi_b^2$ could be considered as background. The background was generally fit to a low-order polynomial in the region ($\chi_b^2 < \chi^2 < \chi_b^2 + \Delta\chi^2$) and the fitted curve was extrapolated to the region ($0. < \chi^2 < \chi_b^2$). Values of $\Delta\chi^2$ ranging from 10 to 60 were used for each plot to ensure that the extrapolated curve was not sensitive to the interval chosen for fitting the background. The number of (γd) events remaining after subtracting the background is indicated in each plot as N_γ.

G. ANGULAR DISTRIBUTION CALCULATION

In order to obtain the angular distribution for the reaction $n+p \rightarrow \gamma+d$, the number of (γd) events in each

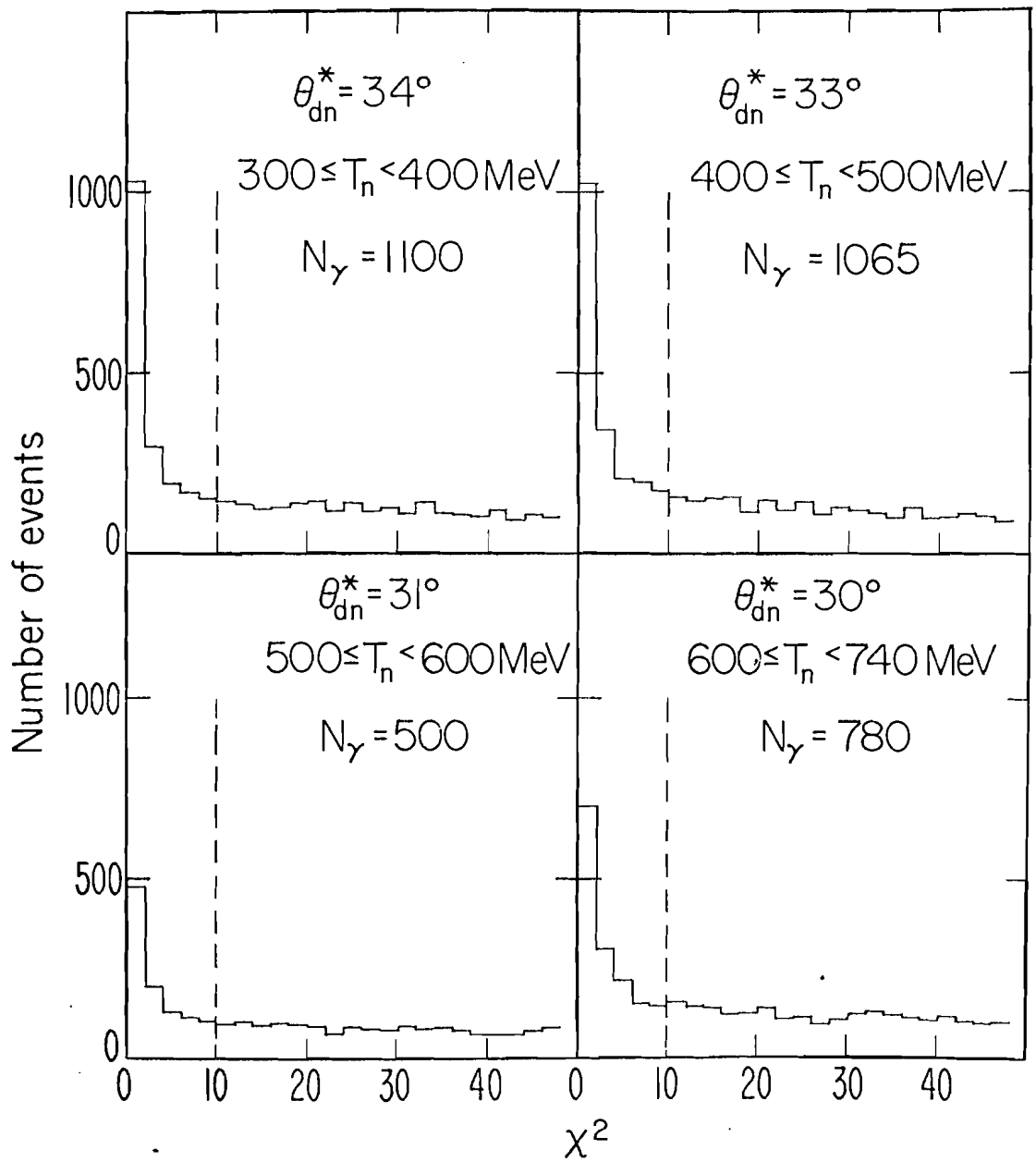

Figure 25(a). χ^2-plots for $\theta^*_{dn} \approx 30^o$

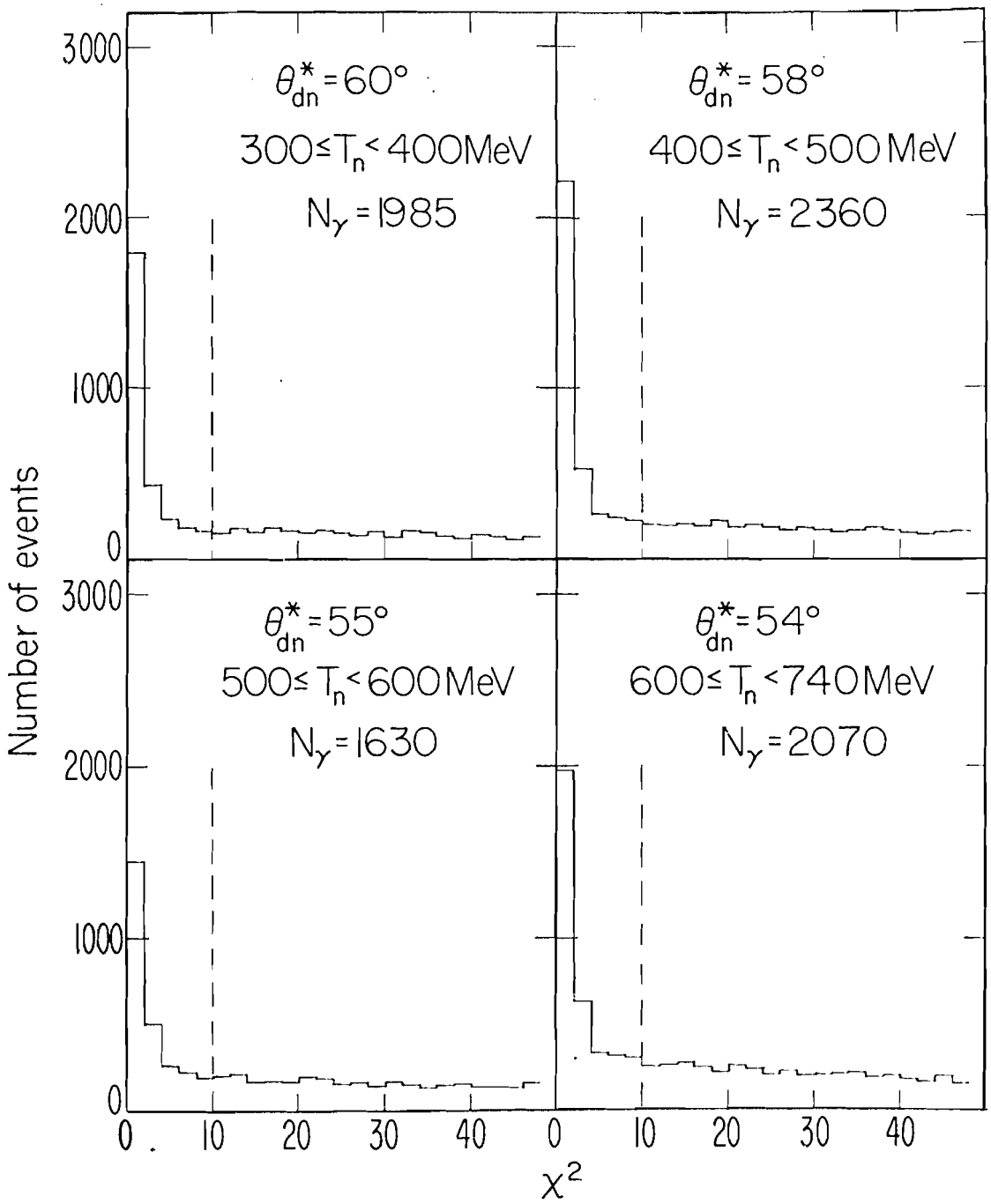

Figure 25(b). χ^2-plots for $\theta^*_{dn} \approx 60°$

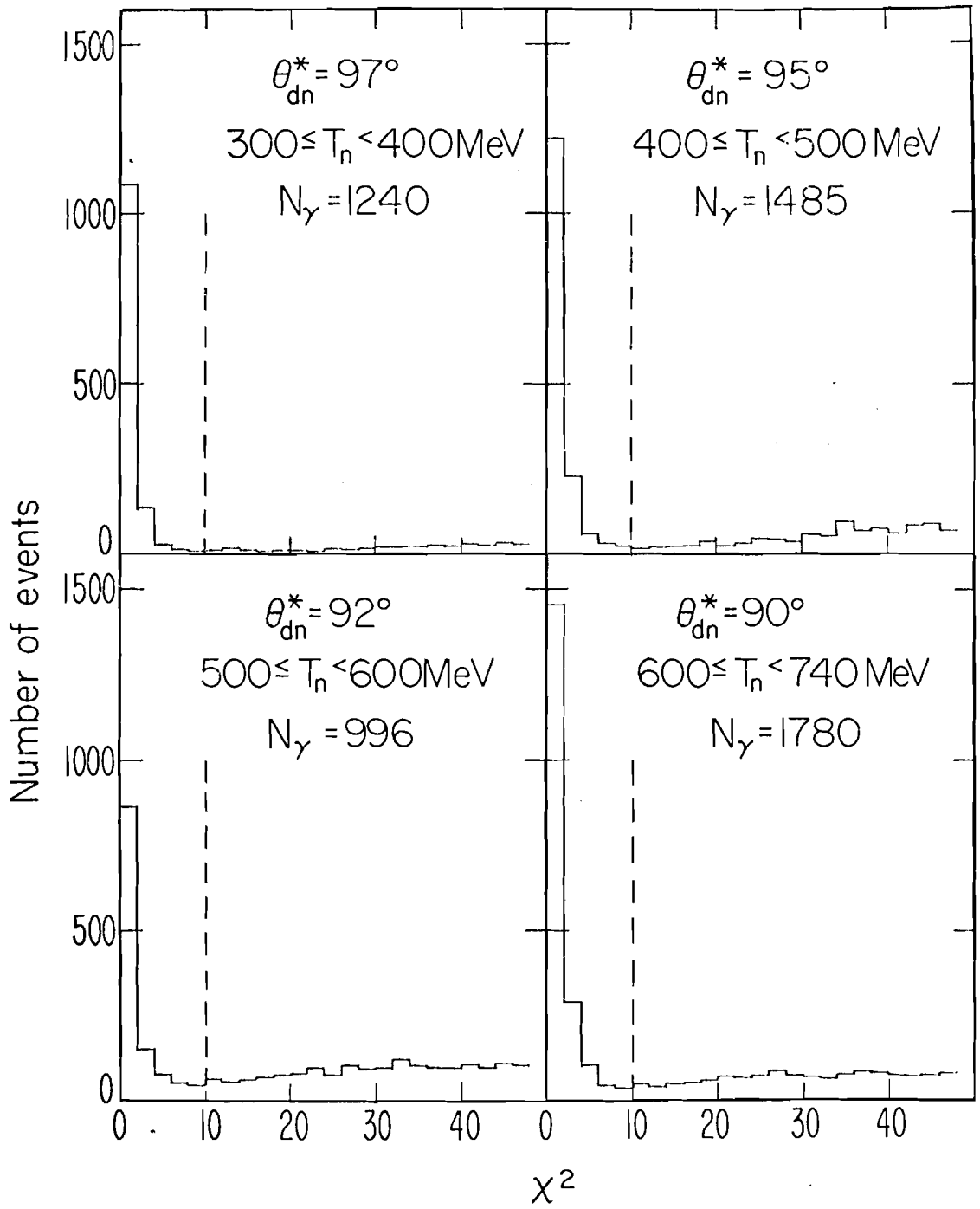

Figure 25(c). χ^2-plots for $\theta^*_{dn} \approx 90^o$

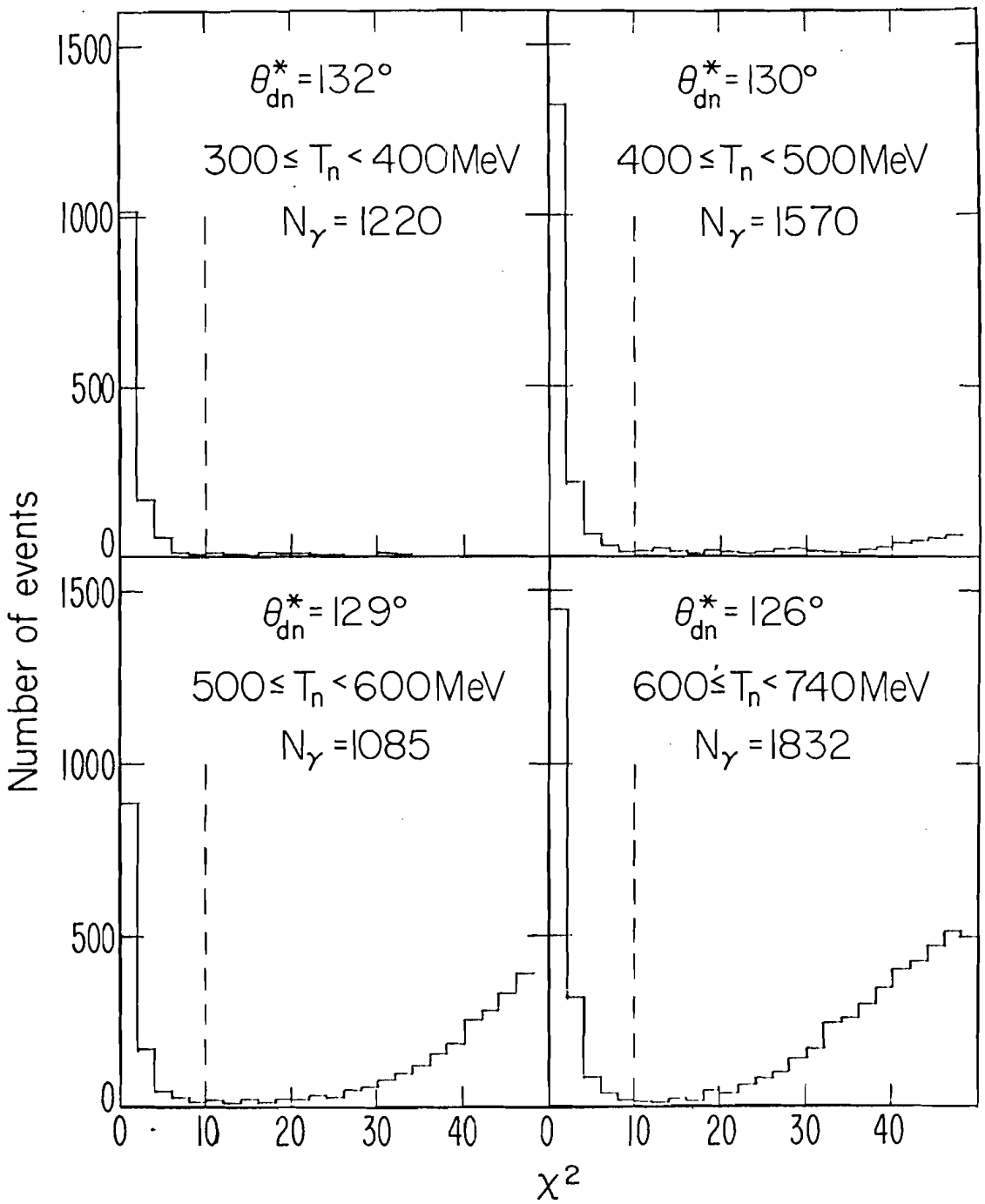

Figure 25(d). χ^2-plots for $\theta^*_{dn} \simeq 120^o$

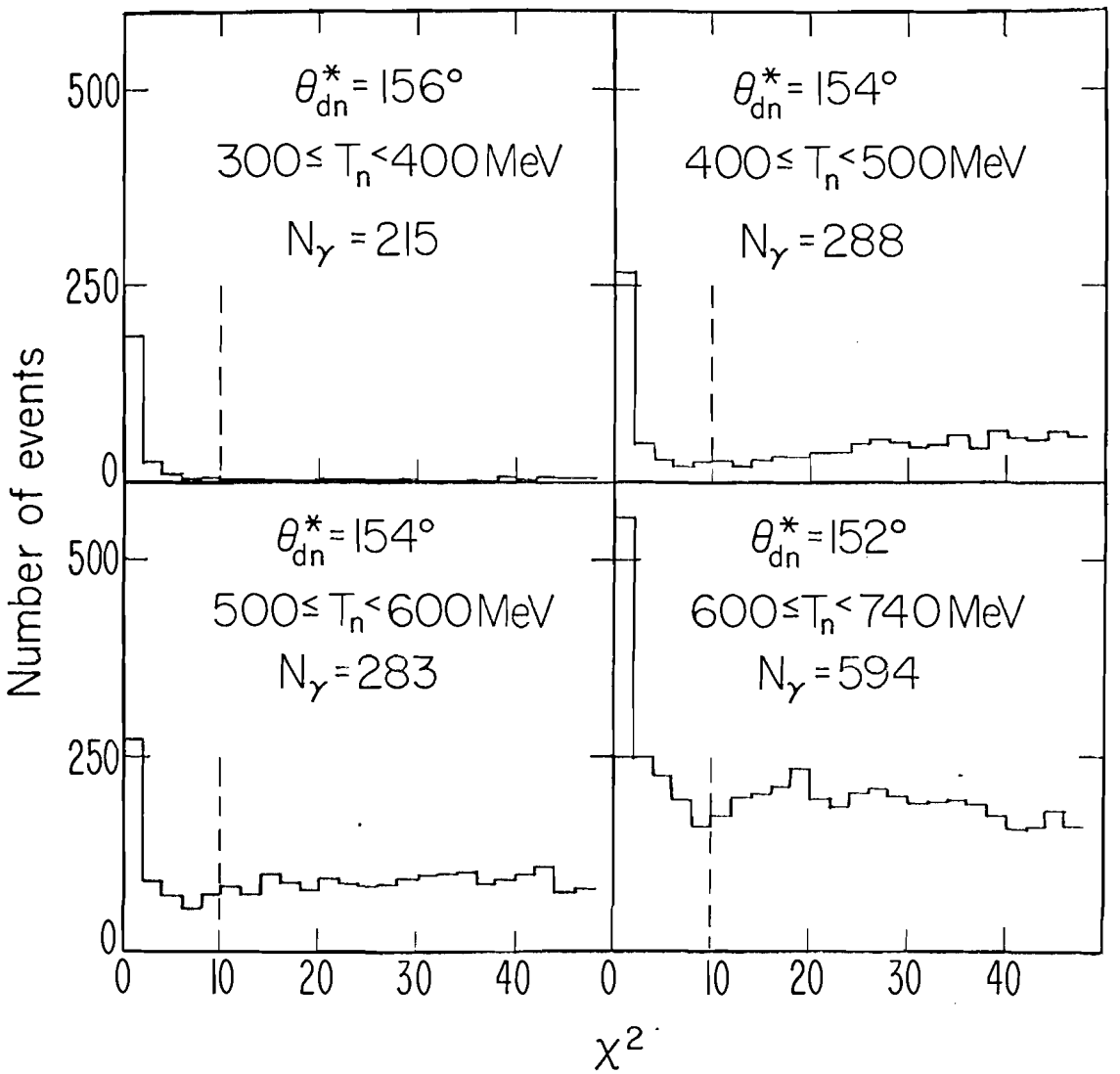

Figure 25(e). χ^2-plots for $\theta^*_{dn} \simeq 150^o$

energy-angle bin, $N_\gamma(\overline{\theta}^*_{dn},\Delta T_n)$, was divided by the effective solid angle for that bin (see Section III-E-2), and all bins were then normalized to an equal number of neutron beam monitor counts (see Section II-B-7). The resulting numbers, $N^c_\gamma(\overline{\theta}^*_{dn},\Delta T_n)$, were then plotted, for all bins with the same ΔT_n, as a function of θ^*_{dn}. These plots constituted the uncorrected $n+p \rightarrow \gamma+d$ angular distributions. In order to obtain the final, measured angular distributions, the plots were then corrected for the various inefficiencies and systematic effects to be discussed in the following sections.

H. CORRECTIONS TO THE ANGULAR DISTRIBUTIONS

1. Nuclear Scattering of the Deuteron

A significant fraction of the deuterons from the reaction $n+p \rightarrow \gamma+d$ were lost due to nuclear scattering in the LH_2 target and in the spectrometer system. Since the total cross section for deuteron-nuclear scattering is rather strongly momentum dependent over the momentum range of this experiment, this scattering had a significant effect on the measured angular distribution for $n+p \rightarrow \gamma+d$.

The kinematic constraints applied by the fitting programs to the momentum and angle measurements for deuterons from $n+p \rightarrow \gamma+d$ (see Section III-D) were so severe that if the deuteron nuclear-scattered through an angle greater

than 0.5° it was rejected (given a high χ^2-value) by the fitting programs. Thus the deuteron losses in the LH_2 target and spectrometer system could be calculated from the total cross section for deuteron-nuclear scattering for all material through which the deuteron passed.

The total cross section, $\sigma_d(P_d,A)$, for deuterons of momentum P_d scattering from nuclei of atomic number A was calculated from the measured total cross sections for neutrons and protons scattering from the same nuclei, $\sigma_n(P_d/2,A)$ and $\sigma_p(P_d/2,A)$, respectively. Data for $\sigma_n(P_d/2,A)$ and $\sigma_p(P_d/2,A)$ for nuclei encountered by the deuteron are generally available in the literature. Thus,

$$\sigma_d(P_d,A) = k\ \{\sigma_n(P_d/2,A) + \sigma_p(P_d/2,A)\}$$

where k is a normalization factor necessary to correct for the mutual screening[54] of the neutron and proton bound as a deuteron. The value of $k(\approx 0.82)$ was calculated from data[55] for deuterons scattering on carbon at P_d = 1691 MeV/c, slightly higher than the momentum range of this experiment. The estimated uncertainty in the value of $\sigma_d(P_d,A)$ is approximately 10%.

The solid curve in Fig. 26 represents, as a function of the deuteron momentum, the percentage of deuterons which were lost due to nuclear scattering. The dashed curve is the estimated uncertainty in the percentage lost due to the uncertainty in $\sigma_d(P_d,A)$. Other factors, to be discussed in

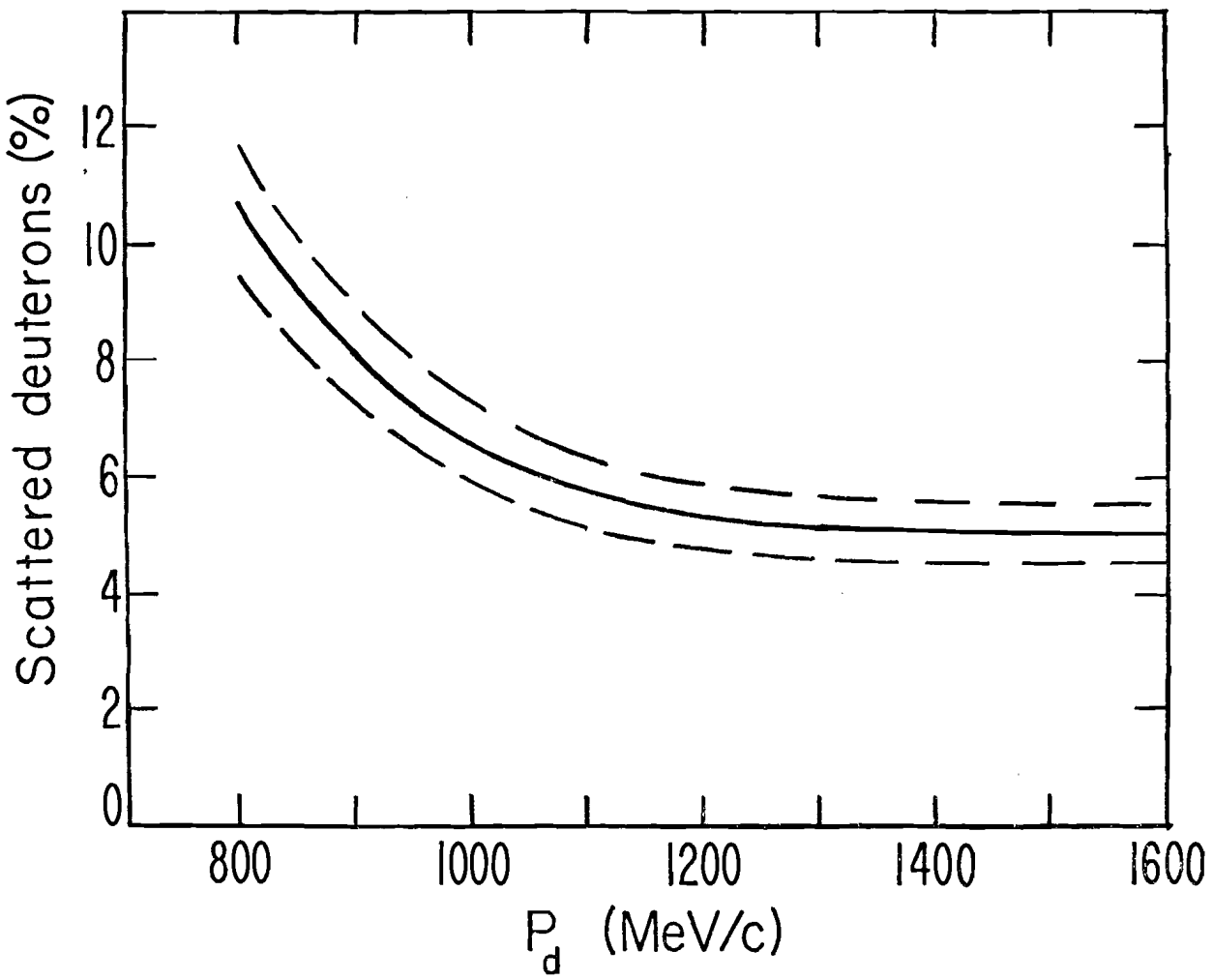

Figure 26. Percentage of Deuterons Lost Due to Nuclear Scattering

Section IV-B-4, increased the total uncertainty but these factors are not included in the uncertainty indicated by the dashed curve. The angular distribution was corrected by calculating the average deuteron momentum for each energy-angle bin and then increasing the value of $N_\gamma^c(\bar{\theta}^*_{dn}, \Delta T_n)$ by the appropriate percentage found from the solid curve in Fig. 26.

2. Accidentals in the LH2 Anti-counters

Although most of the important accidental coincidence rates were less than 1%, accidental rates from the anti-counters partially surrounding the LH_2 target ranged from 2.0% to 8.2% depending on the deuteron scattering angle θ^*_{dn}. These rates were continuously measured by delaying one of the inputs to the coincidence by 51 nanoseconds (see Section II-B-8), and appropriate corrections were made in the values of the $N_\gamma^c(\bar{\theta}^*_{dn}, \Delta T_n)$.

3. Target Empty Corrections

For each configuration of the apparatus, events were collected with no liquid-hydrogen in the target flask. The collected events, resulting from neutron interactions in hydrogen gas and in the mylar walls of the flask, were then processed in exactly the same manner as events from target-full runs. The processed events were then

normalized to the neutron beam monitor counts, and small corrections (<1%) were made to the angular distributions.

4. Neutron Energy Adjustment

The neutron kinetic energy T_n assigned to each event was not explicitly measured but rather was calculated from the measured kinematic parameters assuming that the event was an $n+p \rightarrow \gamma+d$ reaction (see Section III-D). Thus any systematic errors present in the measured parameters were reflected as a systematic error in T_n for each event. Since the neutron energy spectrum was very structured (see Fig. 4), systematic errors in the neutron energy assignment for the five configurations of the apparatus could have caused a large systematic error in the angular distribution. To ensure that such was not the case, the neutron energy spectrum was calculated as described in Section II-B-2 and plotted for each experimental configuration. For each configuration, a correction to T_n was then calculated such that, when the correction was made to the T_n for each event, the resulting spectrum for the configuration was as similar as possible to the spectrum in Fig. 4. The corrected spectra were not all identical due to differing resolutions and background subtraction difficulties, but the prominent features of the spectra, the high-energy peak and end point, could be matched sufficiently accurately to ensure that the systematic errors in the neutron energy

assignment had been reduced to the 0.25% level. The corrections to T_n ranged from 0.2% to 0.6% depending on the momentum and scattering angle of the deuteron. It should be pointed out that these corrections were made <u>before</u> the numbers $N_\gamma(\theta^*_{dn}, \Delta T_n)$ were obtained from the binning and histogramming routines (see Sections III-F and III-G), and thus no explicit correction to the angular distribution was necessary.

The largest systematic errors in the measurement of the kinematic parameters occurred in the measurements of the scattering angle and momentum of the deuteron and were possibly caused by the fringing field of the cyclotron magnet. As an alternative to correcting T_n explicitly, it would have been possible to make corrections to these two parameters, $|\vec{P}_d|$ and θ_d, thus implicitly correcting T_n. However, in that case, the kinematic fitting (see Section III-D) would have had to be redone at least once and possibly several times in order to check the corrections. It was not considered necessary to do this, particularly since the (γd) Monte Carlo indicated that errors in $|\vec{P}_d|$ and θ_d of the right magnitude to cause the observed shift in T_n did not appreciably broaden the (γd) χ^2-peak. Consequently, it was more expedient to make the explicit correction to T_n.

5. Additional Photon Detection Considerations

Two factors affecting the efficiency for detecting photons from $n+p \rightarrow \gamma+d$ have to be considered in addition to the overall efficiency of the γ-chamber itself (see Section III-B-3). These factors are: (1) loss of events due to the conversion of the $n+p \rightarrow \gamma+d$ photon into an electron-positron pair before passing through the anti-counter A_6 in front of the γ-chamber and (2) possible loss of events from soft photons, produced by the primary shower in the gamma chamber, which were invisible in the chamber but which could convert and count in A_6, thus vetoing the event.

The percentage of photons from $n+p \rightarrow \gamma+d$ which were converted before passing through A_6 ranged from 1.1% to 2.2% depending on the photon energy and the amount of material traversed by the photon. Small corrections (<1%) were made to the angular distribution on the basis of: (1) the energy dependence of the photon mass absorption coefficients[56] and (2) the position of the γ-chamber relative to the LH_2 target (the position of the γ-chamber determined the amount of air through which the photon passed).

No correction was made to the angular distribution for the effect from soft photons, produced by the $n+p \rightarrow \gamma+d$ photon shower, which converted in the anti-counter A_6.

However, in order to estimate the magnitude of the effect, relevant results from a $\pi^- p$ charge exchange experiment[57], conducted at higher photon energies but using a detector similar to the one in this experiment, were extrapolated linearly to the energy range of this experiment. On the basis of this extrapolation, the effect on the angular distribution was less than 0.6%. However, since the effect is an unknown function of the geometry of the experiment and since the linear extrapolation is not completely justifiable, no correction was made to the angular distribution.

IV. RESULTS AND CONCLUSIONS

A. GENERAL COMMENTS

As described in Section II-C, two measurements of the angular distribution were made. The procedures for the two measurements were identical except that 85% of the total sample of events were collected in the first measurement and only 15% in the second measurement. The measurement with 85% of the data will hereafter be labeled Sample I and that with 15% Sample II. Both samples were processed separately to obtain two distinct angular distributions. The data points for these two distributions were then combined, with proper weights, to obtain the final angular distribution. Also, the combined data points were fit to a second degree Legendre series and the coefficients resulting from the fit were used to calculate the value of the T-violating phase angle ϕ appearing in equation (22) in Section I-E.

For both Samples I and II, the angular distribution was measured at five scattering angles with nominal values $\theta^*_{dn} = 30^\circ, 60^\circ, 90^\circ, 120^\circ$ and 150° where θ^*_{dn} is the c.m. angle of the deuteron relative to the neutron. For the measurement at $\theta^*_{dn} \simeq 30^\circ$, two distinct configurations of the apparatus were used. The gamma chamber was positioned identically for both configurations but different currents

were used in the analyzing magnet in order to efficiently collect the wide range of deuteron momenta at this scattering angle. Consequently two data points for $\theta^*_{dn} \simeq 30^o$ will appear in the angular distributions to be presented for Samples I and II.

B. ERROR ANALYSIS

1. General Description

The uncertainties in the measured data points for the angular distribution were estimated independently for Samples I and II. For both samples, the total uncertainty in each data point included the statistical uncertainty as well as contributions resulting from the uncertainties in the background subtraction, the solid angle calculation, the deuteron nuclear-scattering losses and the neutron energy determination. Each factor contributing to the calculated total uncertainty is briefly discussed in the following sections.

2. Background Subtraction Uncertainty

The background subtraction procedure was discussed in Section III-F. The uncertainty in the subtraction was determined by calculating the errors in the coefficients resulting from the polynomial fit to the background in the

χ^2-region: $\chi_b^2 < \chi^2 \leq \chi_b^2 + \Delta\chi^2$ (see Section III-F). The uncertainty in the number of subtracted events could then be calculated from the errors in the coefficients. This determination of the subtraction uncertainty was checked by choosing values of $\Delta\chi^2$ ranging from 10.0 to 60.0 and noting the subsequent variation in the predicted number of $(\pi^o d)$ events in the range: $\chi^2 < \chi_b^2$. In kinematic regions heavily contaminated with background (see Fig. 20b), the subtraction uncertainty was often larger than the purely statistical uncertainty in the number of (γd) events.

3. Solid Angle Calculation Uncertainty

The method for calculating the solid angle subtended by the apparatus for each scattering angle was described in Section III-E-2. The uncertainty in this calculation was due primarily to uncertainties in the distributions which served as input to the Monte Carlo programs, e.g., the geometric distribution and energy spectrum of the neutron beam (see Figs. 3 and 4). The inputs to the Monte Carlo program were varied within reasonable bounds and the subsequent variations in the calculated solid angle were used to estimate the resultant uncertainty. It should be pointed out that the solid angle for the experiment was not merely a function of the geometry of the apparatus but rather was also a function of the deuteron momentum due to the presence of the analyzing magnet.

4. Uncertainty in Deuteron Nuclear-scattering Losses

The calculation of the losses due to the nuclear scattering of the deuteron was described in Section III-H-1. As pointed out in that section, the deuteron total cross section for nuclear scattering was considered accurate to only about 10% and this lack of precision caused a similar 10% uncertainty in the correction to the number of observed deuterons. Since the loss correction ranged from 3% to 10%, the uncertainty in the correction due to the imprecise cross section was less than 1%. However, two other factors made this uncertainty somewhat larger. One factor was that the total cross section was used to calculate the loss correction whereas deuterons which scattered through small angles were actually not rejected (given high χ^2-values) by the kinematic fitting program. The second factor resulted from uncertainties in the amount of material through which the deuteron had passed. The effect of these two factors was to increase the uncertainty such that it ranged from 0.8% to 2.6% depending on the energy-angle bin.

5. Uncertainty in the Neutron Energy Determination

Systematic errors in the determination of the neutron energy T_n were discussed in Section III-H-4. In that section it was stated that these errors were reduced to the

0.25% level. The uncertainty in the number of events in each energy interval resulting from errors in T_n of this magnitude was estimated from the neutron energy spectrum appearing in Fig. 4. The uncertainty at each scattering angle depended on how well the spectrum could be recovered which in turn was determined by the amount of background contamination. The contribution to the total uncertainty from this effect ranged from 0.2% to 3.4% depending on the energy and angle.

6. Total Calculated Uncertainty

The calculated uncertainties in the data points, resulting from the factors discussed in the preceding sections, are listed (as percentages) for all the energy-angle bins for Samples I and II in Tables 4 and 5, respectively. The total uncertainty in each data point, obtained by quadrature from the individual uncertainties, is also listed. Any uncertainties in the data not appearing in these tables are considered to be of negligible magnitude.

C. ANGULAR DISTRIBUTION RESULTS

The angular distribution was calculated, for four T_n intervals, as described in Section III-G and subsequent corrections to the distributions were made as described in Sections III-H(1-5). The resulting corrected, but

TABLE 4

ESTIMATED UNCERTAINTIES (%) FOR SAMPLE I

T_n INTERVAL	$\overline{\theta^*_{dn}}$	STAT.	BACKGD.	S.A.	D.N.S.	NEUT.	TOTAL
300-400 MeV	28.	5.1	5.3	2.9	1.0	1.5	8.1
$\overline{T_n}$= 358 MeV	34.	3.0	2.3	2.0	1.0	1.5	4.6
	60.	2.2	2.5	2.2	1.2	1.2	4.3
	97.	2.8	1.6	2.2	1.5	0.9	4.3
	132.	2.9	0.8	2.2	2.0	0.9	4.3
	156.	6.8	1.9	2.4	2.6	1.5	8.0
400-500 MeV	32.	3.6	5.2	1.9	0.8	1.8	6.9
$\overline{T_n}$= 446 MeV	33.	3.1	2.8	2.0	0.8	1.8	5.0
	58.	2.1	1.7	1.9	1.0	1.6	3.8
	95.	2.6	1.7	2.1	1.2	1.3	4.1
	130.	2.5	1.3	2.1	1.6	1.3	4.1
	154.	5.9	5.2	2.1	2.2	1.8	8.6
500-600 MeV	31.	4.4	6.0	2.4	0.8	0.2	7.9
$\overline{T_n}$= 548 MeV	33.	4.3	5.6	2.8	0.8	0.2	7.6
	55.	2.5	2.5	2.5	0.8	0.2	4.4
	92.	3.2	2.0	2.6	0.9	0.2	4.7
	129.	3.0	1.8	2.5	1.3	0.2	4.5
	154.	6.0	8.9	2.5	1.8	0.2	11.2
600-740 MeV	30.	3.6	3.9	1.7	0.8	1.4	5.8
$\overline{T_n}$= 672 MeV	34.	3.9	3.8	2.4	0.8	1.4	6.2
	54.	2.2	2.4	1.9	0.8	1.4	4.1
	90.	2.4	1.4	1.8	0.8	1.4	3.7
	126.	2.3	1.1	1.9	1.1	1.4	3.6
	152.	4.1	8.4	1.7	1.5	1.4	9.7

STAT. = Statistical Uncertainty
BACKGD. = Background subtraction uncertainty
S.A. = Solid angle uncertainty
D.N.S. = Deuteron nuclear-scattering uncertainty
NEUT. = Neutron energy determination uncertainty

TABLE 5

ESTIMATED UNCERTAINTIES (%) FOR SAMPLE II

T_n INTERVAL	$\overline{\theta^*_{dn}}$	STAT.	BACKGD.	S.A.	D.N.S.	NEUT.	TOTAL
300-400 MeV	28.	11.2	15.2	2.9	1.0	2.1	19.2
$\overline{T_n}$= 358 MeV	34.	8.5	10.9	2.0	1.0	2.1	14.2
	60.	7.8	7.3	2.2	1.2	1.8	11.1
	97.	6.1	1.1	2.2	1.5	1.5	6.9
	132.	10.1	2.0	2.2	2.0	1.5	10.8
	156.	9.8	2.9	2.4	2.6	2.3	11.1
400-500 MeV	32.	7.2	7.8	1.9	0.8	1.8	11.0
$\overline{T_n}$= 446 MeV	33.	7.9	8.7	2.0	0.8	1.3	12.0
	58.	6.3	8.0	1.9	1.0	2.1	10.6
	95.	5.4	2.3	2.1	1.2	2.1	6.7
	130.	9.1	1.7	2.1	1.6	2.6	10.0
	154.	8.0	6.5	2.1	2.2	3.1	11.2
500-600 MeV	31.	9.1	12.4	2.4	0.8	0.2	15.6
$\overline{T_n}$= 548 MeV	33.	11.6	16.0	2.8	0.8	0.2	20.0
	55.	7.8	6.2	2.5	0.8	0.3	10.3
	92.	7.2	6.2	2.6	0.9	0.2	9.9
	129.	12.2	3.0	2.5	1.3	0.2	12.9
	154.	9.1	12.5	2.5	1.8	0.6	15.8
600-740 MeV	30.	6.6	8.6	1.7	0.8	2.0	11.2
$\overline{T_n}$= 672 MeV	34.	10.4	16.3	2.4	0.8	1.4	19.6
	54.	7.0	7.4	1.9	0.8	2.2	10.6
	90.	4.9	3.9	1.8	0.8	1.4	6.7
	126.	8.8	2.3	1.9	1.1	2.0	9.6
	152.	5.9	7.0	1.7	1.5	3.4	10.0

STAT. = Statistical uncertainty
BACKGD. = Background subtraction uncertainty
S.A. = Solid angle uncertainty
D.N.S. = Deuteron nuclear-scattering uncertainty
NEUT. = Neutron energy determination uncertainty

unnormalized, angular distribution was then fitted to a second degree Legendre polynomial series and normalized by requiring that the total cross section found by integrating the series have a value of 4π. The resulting data points for Samples I and II appear, with their percentage uncertainties, in Tables 6 and 7, respectively. The values of θ^*_{dn} appearing in both tables are the average deuteron scattering angles for the appropriate energy-angle bins. Each angle bin spanned approximately 20° in the c.m. system, and uncertainties in the θ^*_{dn} averages were considered to be negligible relative to the uncertainties in the amplitudes for the data points.

The angular distributions for Samples I and II are plotted in Fig. 27. The solid curve is the fit of Legendre polynomials to the data of Sample I and the dashed curve is the corresponding fit to the data of Sample II. These curves indicate that the data points from the two samples are statistically consistent with each other. Consequently, the data points from the two samples were combined, with proper weights, and the resulting final angular distributions, normalized as described above, appear in Table 8 and Fig. 28. The coefficients from the second degree Legendre fit (A_o, A_1 and A_2) as well as the χ^2/d for each fit are listed in Table 9.

Measurements[58,59,60] of the angular distribution for $\gamma+d \rightarrow n+p$ and another measurement of $n+p \rightarrow \gamma+d$ by a

TABLE 6

$n+p \rightarrow \gamma+d$ ANGULAR DISTRIBUTION FOR SAMPLE I

T_n INTERVAL	$\overline{\theta^*_{dn}}$	VALUE	ERROR(%)
300-400 MeV	28.	1.06	8.1
$\overline{T_n}$= 358 MeV	34.	1.04	4.6
	60.	1.18	4.3
	97.	1.08	4.3
	132.	0.80	4.3
	156.	0.60	8.0
400-500 MeV	32.	1.07	6.9
$\overline{T_n}$= 446 MeV	33.	0.99	5.0
	58.	1.06	3.8
	95.	1.16	4.1
	130.	0.86	4.1
	154.	0.58	8.6
500-600 MeV	31.	0.96	7.9
$\overline{T_n}$= 548 MeV	33.	0.96	7.6
	55.	1.12	4.4
	92.	1.12	4.7
	129.	0.86	4.5
	154.	0.74	11.2
600-740 MeV	30.	0.90	5.8
$\overline{T_n}$= 672 MeV	34.	0.97	6.2
	54.	1.02	4.1
	90.	1.14	3.7
	126.	0.93	3.6
	152.	0.86	9.7

TABLE 7

$n+p \rightarrow \gamma+d$ ANGULAR DISTRIBUTION FOR SAMPLE II

T_n INTERVAL	$\overline{\theta^*_{dn}}$	VALUE	ERROR(%)
300-400 MeV	28.	0.92	19.2
$\overline{T_n}$= 358 MeV	34.	0.93	14.2
	60.	1.13	11.1
	97.	1.10	6.9
	132.	0.96	10.8
	156.	0.63	11.1
400-500 MeV	32.	1.00	11.0
$\overline{T_n}$= 446 MeV	33.	0.97	12.0
	58.	1.17	10.6
	95.	1.10	6.7
	130.	0.89	10.0
	154.	0.61	11.2
500-600 MeV	31.	1.03	15.6
$\overline{T_n}$= 548 MeV	33.	1.00	20.0
	55.	1.34	10.3
	92.	1.00	9.9
	129.	0.84	12.9
	154.	0.71	15.8
600-740 MeV	30.	1.06	11.2
$\overline{T_n}$= 672 MeV	34.	0.91	19.6
	54.	1.08	10.6
	90.	1.06	6.7
	126.	0.91	9.6
	152.	0.84	10.0

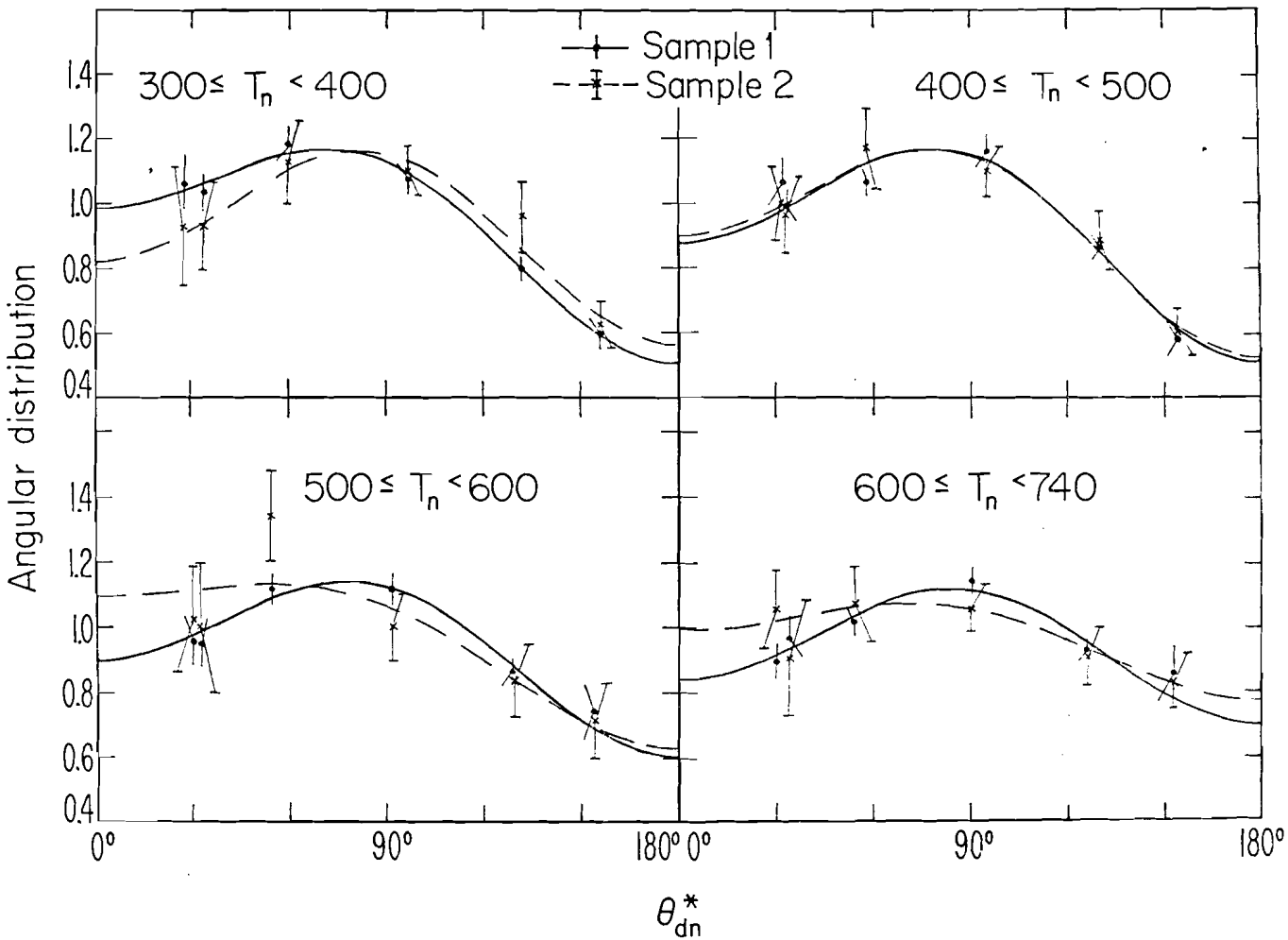

Figure 27. n+p → γ+d Angular Distributions for Samples I and II

TABLE 8

FINAL $n+p \rightarrow \gamma+d$ ANGULAR DISTRIBUTION

T_n INTERVAL	$\overline{\theta^*_{dn}}$	VALUE	ERROR(%)
300-400 MeV	28.	1.03	7.5
$\overline{T_n}$= 358 MeV	34.	1.02	4.4
	60.	1.17	4.0
	97.	1.08	3.6
	132.	0.82	4.0
	156.	0.61	6.5
400-500 MeV	32.	1.06	5.8
$\overline{T_n}$= 446 MeV	33.	0.99	4.6
	58.	1.07	3.6
	95.	1.16	3.5
	130.	0.86	3.8
	154.	0.60	6.8
500-600 MeV	31.	0.97	7.0
$\overline{T_n}$= 548 MeV	33.	0.96	7.1
	55.	1.15	4.0
	92.	1.09	4.3
	129.	0.86	4.3
	154.	0.72	9.1
600-740 MeV	30.	0.92	5.2
$\overline{T_n}$= 672 MeV	34.	0.96	5.9
	54.	1.02	3.8
	90.	1.13	3.2
	126.	0.93	3.4
	152.	0.86	7.0

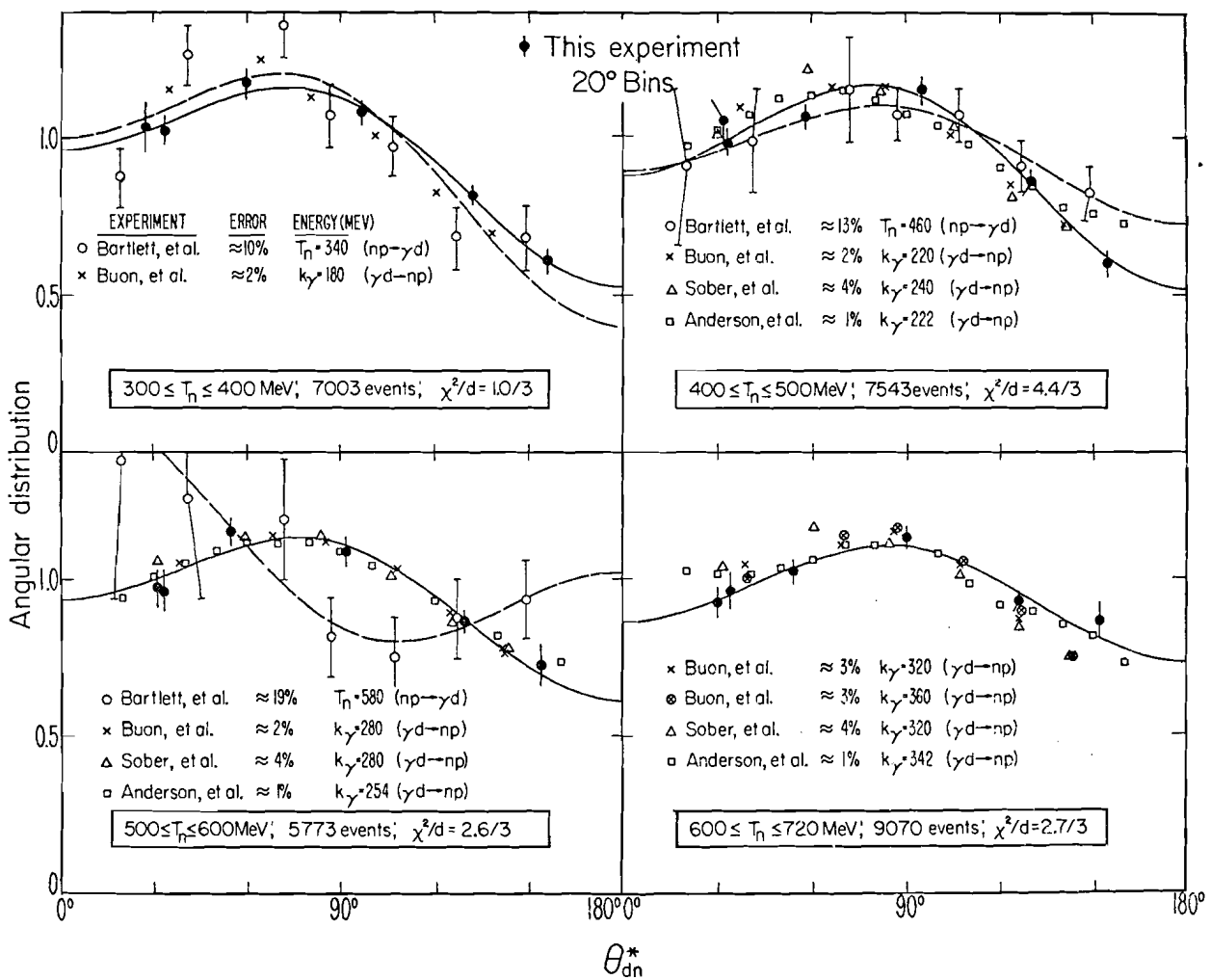

Figure 28. Comparison of Angular Distributions for n+p → γ+d and γ+d → n+p

TABLE 9

SECOND DEGREE LEGENDRE COEFFICIENTS

SAMPLE	T_n(MeV)	A_o	A_1	A_2	χ^2/d
I	300-400	20.4±0.2	4.8±0.3	-5.2±0.5	0.9/3
I	400-500	20.4±0.5	3.7±0.7	-6.2±1.2	4.4/3
I	500-600	14.0±0.2	2.1±0.3	-3.5±0.6	1.3/3
I	600-740	24.8±0.4	1.7±0.7	-5.7±1.2	2.5/3
II	300-400	20.2±0.6	2.6±0.9	-6.2±1.1	1.2/3
II	400-500	22.4±0.4	4.2±0.6	-6.5±0.8	0.6/3
II	500-600	13.2±0.7	3.0±1.1	-1.8±1.6	3.3/3
II	600-740	26.1±0.5	2.8±0.8	-3.0±1.0	0.6/3
I + II	300-400	20.4±0.2	4.4±0.3	-5.3±0.5	1.0/3
I + II	400-500	20.7±0.5	3.8±0.6	-6.2±1.0	4.4/3
I + II	500-600	13.8±0.3	2.2±0.4	-3.2±0.7	2.6/3
I + II	600-740	25.0±0.4	1.6±0.7	-5.1±1.0	2.7/3

Princeton group[61] were normalized by the same procedure and are also displayed in Fig. 28. The solid curve in Fig. 28 is the second degree fit in Legendre polynomials to our data for which the χ^2/d is indicated. The dashed curve is a similar fit to the Princeton data. Our results are in good agreement with results from the inverse reaction for all energies as expected from T-invariance independently of any model (The comparison between $n+p \rightarrow \gamma+d$ and $\gamma+d \rightarrow n+p$ must be made at the same c.m. energy for which $T_n \approx 2k\gamma$ where $k\gamma$ is the photon laboratory energy in $\gamma+d \rightarrow n+p$.).

Good agreement between the two measurements of $n+p \rightarrow \gamma+d$ is evident at the two lower energy intervals but there appears to be a significant discrepancy in the T_n interval 500 - 600 MeV. Since the difference in the average neutron energies for the two experiments was ≈ 30 MeV, no quantitative estimate of the discrepancy is made. A more suitable method of comparison will be discussed in the next section.

D. CONCLUSIONS

The difficulty in comparing the $n+p \rightleftarrows \gamma+d$ angular distributions, resulting from the differences in the c.m. energies at which the distributions were measured, can be avoided to some degree by plotting the normalized coefficients from the Legendre fit as a function of the neutron (or photon) energy. The normalization-independent ratios,

A_1/A_o and A_2/A_o, are plotted in Fig. 29 for the two measurements of $n+p \rightarrow \gamma+d$ and for recent measurements of $\gamma+d \rightarrow n+p$.

Figure 29 indicates that the various measurements of the angular distribution for $\gamma+d \rightarrow n+p$ are statistically inconsistent at some energies. However, the disagreement among the $\gamma+d \rightarrow n+p$ measurements is much smaller than the predicted difference (from Barshay's model) between the angular distributions for $\gamma+d \rightarrow n+p$ and $n+p \rightarrow \gamma+d$ resulting from a hypothetical maximal T-violation. Barshay predicted, for a maximal T-violation, differences of $\simeq 0.3$ between $A_2/A_o(np\rightarrow\gamma d)$ and $A_2/A_o(\gamma d\rightarrow np)$ at $T_n = 590$ MeV (see Section I-E). The differences in A_2/A_o for the various $\gamma+d \rightarrow n+p$ measurements are much smaller than 0.3 and consequently a meaningful reciprocity comparison between $n+p \rightarrow \gamma+d$ and $\gamma+d \rightarrow n+p$ can be made.

From Fig. 29, it can be seen that the Princeton value for A_2/A_o at $T_n = 580$ MeV deviates by approximately three standard deviations from the values of A_2/A_o for the inverse reaction. In contrast, our values for A_2/A_o are in good agreement with corresponding values from the inverse reaction for all neutron energies in the range 300 to 720 MeV. In particular, comparing our values of A_2/A_o to those from the inverse reaction at $T_n = 590$ MeV, we calculate that the T-violating phase ϕ, appearing in equation (22) in Section I-E, has a value $\phi = (4\pm10)^o$. Thus our results,

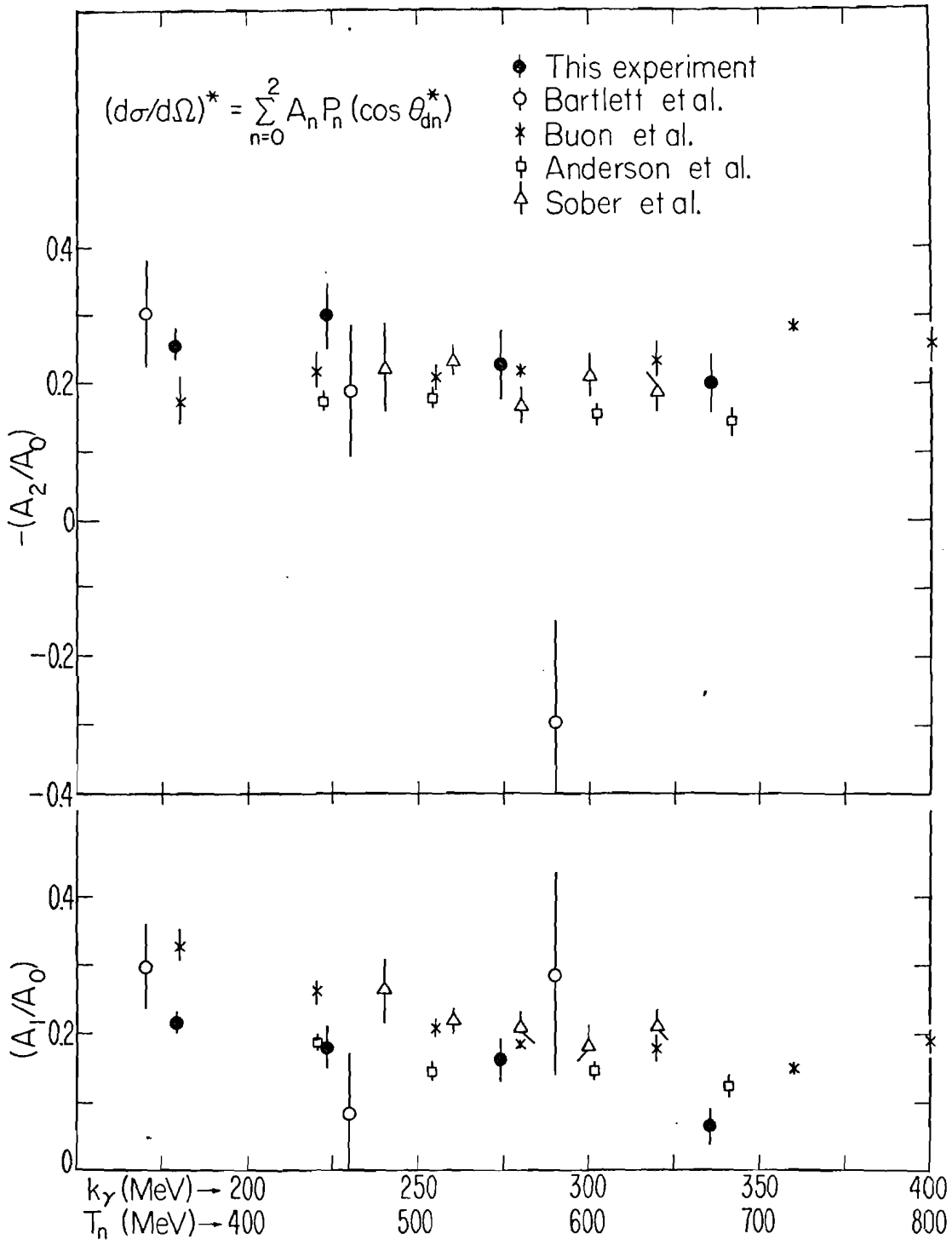

Figure 29. Plot of A_1/A_o and A_2/A_o as a Function of T_n and k_γ

interpreted in the framework of Barshay's model, and also independent of any model, <u>are consistent with time-reversal invariance in the reaction $np \rightleftarrows \gamma d$</u>.

It is hoped that two new measurements of $n+p \rightarrow \gamma+d$, recently completed at Princeton[62] and at Berkeley[63] and presently under analysis, will resolve the discrepancy between the values of A_2/A_o at $T_n \approx 585$ MeV as determined by this experiment and by the previous Princeton experiment.

REFERENCES

1. J. H. Christenson, J. W. Cronin, V. L. Fitch and R. Turlay, Phys. Rev. Letters 13, 138 (1964).
2. J. Steinberger, Topical Conf. on Weak Interactions, CERN(Geneva), p. 291 (1969).
3. J. Bernstein, G. Feinberg and T. D. Lee, Phys. Rev. 139, B1650 (1965).
4. S. Barshay, Phys. Letters 17, 78 (1965).
5. S. Barshay, Phys. Rev. Letters 17, 49 (1966).
6. N. Austern, Phys. Rev. 100, 1522 (1955).
7. T. D. Lee and C. S. Wu, Ann. Rev. Nucl. Sci. 16, 511 (1966).
8. J. W. Cronin, Proc. 14th Int. Conf. on High-Energy Physics, Vienna, p. 281 (1968).
9. T. D. Lee, R. Oehme and C. N. Yang, Phys. Rev. 106, 340 (1957).
10. B. Aubert, L. Behr, J. P. Lowys, P. Mittner and C. Pascaud, Phys. Letters 10, 215 (1964).
11. C. S. Wu, E. Ambler, R. W. Hayward, D. D. Hoppes and R. P, Hudson, Phys. Rev. 105, 1413 (1957).
12. L. Grodzins and F. Genovese, Phys. Rev. 121, 228 (1961).
13. D. E. Alburger, R. E. Pixley, D. H. Wilkinson and P. Donovan, Phil. Mag. 6, 171 (1961).

14. C. Baltay, N. Barash, P. Franzini, N. Gelfand, L. Kirsch, G. Lütjens, J. C. Severiens, J.Steinberger, D. Tycko and D. Zanello, Phys. Rev. Letters 15, 951 (1965).

15. L. Dobrzynski, Nguyen-Huu Xuong, L. Montanet, M. Tomas, J. Duboc and R. A. Donald, Phys. Letters 22, 105 (1966).

16. W. G. Weitkamp, D. W. Storm, D. C. Shreve, W. J. Braithwaite and D. Bodansky, Phys. Rev. 165, 1233 (1968).

17. W. von Witsch, A. Richter and P. von Brentano, Phys. Rev. Letters 19, 524 (1967).

18. A review article by J. Bailey and E. Picasso appeared in Progr. Nucl. Phys. 12, 43-75 (1970).

19. A review article by F. Bopp appeared in Physics of the One- and Two-Electron Atoms, North-Holland Publishing Co., pp. 117-510 (1969).

20. N. Christ and T. D. Lee, Phys. Rev. 143, 1310 (1966).

21. J. R. Chen, J. Sanderson, J. A. Appel, G. Gladding, M. Goitein, K. Hanson, D. C. Imrie, T. Kirk, R. Madaras, R. V. Pound, L. Price, R. Wilson and C. Zajde, Phys. Rev. Letters 21, 1279 (1968).

22. S. Rock, M. Borghini, O. Chamberlain, R. Z. Fuzesy, C. C. Morehouse, T. Powell, G. Shapiro, H. Weisberg, R. L. A. Cottrell, J. Litt, L. W. Mo and R. E. Taylor, Phys. Rev. Letters 24, 748 (1970).

23. M. Gormley, E. Hyman, W. Lee, T. Nash, J. Peoples, C. Schultz and S. Stein, Phys. Rev. Letters 21, 402 (1968).

24. A. M. Cnops, G. Finocchiaro, J. C. Lassalle, P. Mittner, P. Zanella, J. P. Dufey, B. Gobbi, M. A. Pouchon and A. Muller, Phys. Letters 22, 546 (1966).

25. R. A. Bowen, A. M. Cnops, G. Finocchiaro, P. Mittner, J. P. Dufey, B. Gobbi, M. A. Pouchon and A. Muller, Phys. Letters 24B, 206 (1967).

26. M. Gormley, E. Hyman, W. Lee, T. Nash, J. Peoples, C. Schultz and S. Stein, Phys. Rev. Letters 21, 399 (1968).

27. A review article by M. Bazin appeared in Lect. Theor. Phys. 11-A, 901-9 (1969).

28. C. Baglin, A. Bezagnet, B. Degrange, F. Jacquet, P. Musset, N. Nguyen-Khac, G. Nihoul-Boutang, H. H. Bingham and W. Michael, Phys. Letters 24B, 637 (1967).

29. J. K. Baird, P. D. Miller, W. B. Dress and N. F. Ramsey, Phys. Rev. 179, 1285 (1969).

30. A review article by A. Wattenberg appeared in Lect. Theor. Phys. 11-A, 911-18 (1969).

31. N. Christ and T. D. Lee, Phys. Rev. 148, 1520 (1966).

32. P. A. Berardo, R. P. Haddock, B. M. K. Nefkens, L. J. Verhey, M. E. Zeller, A. S. L. Parsons and P. Truoel, Phys. Rev. Letters 26, 201 (1971).

33. W. S. C. Williams, An Introduction to Elementary Particles, Academic Press, New York and London, pp.85-94 (1961).

34. E. A. Whalin, D. Schriever and A. O. Hanson, Phys. Rev. 101, 377 (1956).

35. J. C. Keck and A. V. Tollestrup, Phys. Rev. 101, 360 (1956).

36. S. Barshay, private communication (1971).

37. R. R. Wilson, Phys. Rev. 86, 261 (1952).

38. W. A. Wenzel, UCRL-11319 (1964).

39. L. Kaufman (Ph.D. Thesis), UCRL-17605, pp. 67-76 (1967).

40. Q. Kerns, UCRL-10887 (1963).

41. V. Perez-Mendez and J. M. Pfab, Nucl. Inst. and Meth. 33, 141 (1965).

42. F. Kirsten, K. Lee and J. Conragan, UCRL-16539 (1966).

43. R. L. Van Tuyl, V. Perez-Mendez, K. Lee and R. L. Grove, UCRL-17623 (1967).

44. Chronetics Inc., 500 Nuber Ave., Mt. Vernon, New York.

45. Digital Equipment Corp., Maynard, Massachusetts.

46. S. W. Andreae, F. Kirsten, T. A. Nunamaker and V. Perez-Mendez, UCRL-11209(Rev.) (1964).

47. Control Data Corp., 3145 Porter Drive, Palo Alto, California.

48. P. A. Berardo (Ph.D. Thesis), U. C. L. A., 405 Hilgard, Los Angeles, California (unpublished) (1971).

49. T. Schaefer and L. Wilson, private communication.

50. B. Rust, W. R. Burrus and C. Schneeberger, ACM 9, 381 (1965).

51. M. Rich and R. Madey, UCRL-2301 (1954).

52. J. Berge, UCID-1252, University of California, Berkeley, California (1960).

53. S. S. Wilson, M. J. Longo, K. K. Young, R. P. Haddock, J. A. Helland, B. L. Schrock, D. Cheng and V. Perez-Mendez, Phys. Letters 35B, 83 (1971).

54. E. Parker, University of Michigan Thesis, Tech. Report 03028-3-T (1970).

55. L. M. C. Dutton, J. D. Jafar, H. B. van der Raay, D. G. Ryan, J. A. Stiegelmair, R. K. Tandon and J. F. Reading, Phys. Letters 16, 331 (1965).

56. W. P. Trower, UCRL-2426, Vol. II (1966 Rev.).

57. P. Sonderegger, J. Kirz, O. Guisan, F. Falk-Vairant, C. Bruneton, P. Borgeaud, A. V. Stirling, C. Caverzasis, J. P. Guilland, M. Yvert and B. Amblard, Phys. Letters 20, 75 (1966).

58. D. I. Sober, D. G. Cassel, A. J. Sadoff, K. W. Chen and P. A. Crean, Phys. Rev. Letters 22, 430 (1969).

59. J. Buon, V. Gracco, J. Lefrancois, P. Lehmann, B. Merkel and Ph. Roy, Phys. Letters 26B, 595 (1968).

60. R. L. Anderson, R. Prepost and B. H. Wiik, Phys. Rev. Letters 22, 651 (1969).

61. D. F. Bartlett, C. E. Friedberg, K. Goulianos, I. S. Hammerman and D. P. Hutchinson, Phys. Rev. Letters 23, 893 (1969).

62. D. F. Bartlett, Private communication (1971).

63. M. J. Longo, Private communication (1971).